INTERACTION NOTES

Note 222

June 1968

A TECHNIQUE FOR COMPUTING APPROXIMATE ELECTROMAGNETIC IMPULSE RESPONSE OF CONDUCTING BODIES

C. Leonard Bennett, Jr.
Walter L. Weeks

Purdue University

ABSTRACT

A numerical technique for the time domain solution of scattering by perfect conductors is described. The problem is broken into two cases. In the first case scattering by parallel cylindrical conductors with arbitrary cross sections is considered for arbitrary angles of incidence. The first step is to reduce the cylindrical scattering problem to a time-domain integro-differential equation for the magnetic field intensity on the scatterer contour. Next, the integro-differential equation is solved numerically for the magnetic field on the scatterer contour which, in turn, is used to compute the far field. To approximate an electromagnetic impulse the incident wave is taken to be a plane Gaussian pulse, although the technique is not limited to this excitation. The resulting far field is then an approximation to the electromagnetic impulse response. The validity of this technique is demonstrated by using it to calculate the approximate impulse response of a circular cylinder for a normally incident wave. The results are in good agreement with those obtained from the classical frequency domain solution. To illustrate the versatility of the technique the approximate impulse response is also computed for a strip and a corner reflector. The results for these more complex shapes are

consistent with the time domain reciprocity theorem, and thus, provide a further check on the validity of this technique.

In the second case scattering by three dimensional conducting bodies of arbitrary shape is considered. The first step is to reduce the scattering problem to a time domain integro-differential equation for the current density on the surface of the scatterer. Next, the integro-differential equation is solved numerically for the current density at the scatterer which is then used to compute the far field. As in the case of cylindrical scatterers, a plane Gaussian pulse is chosen for the incident field so that the resulting far field is an approximate impulse response. The technique when used to compute the approximate impulse response of a sphere gives results which are in good agreement with those obtained from the classical frequency response. The technique is also used to compute the approximate impulse response of a hemispherical capped cylinder with axial incidence.

One of the applications of the approximate electromagnetic impulse response is illustrated by using it to compute the frequency response of the bodies considered. In addition some close relationships between the approximate impulse response and the scatterer geometry are pointed out.

TABLE OF CONTENTS

LIST OF FIGURES

THIS PAGE IS INTENTIONALLY BLANK.

CHAPTER 1

INTRODUCTION

1.1 General

In military and space applications, the primary means for locating and identifying distant objects continues to be based on the electromagnetic response of these objects. Electromagnetic sensors do the bulk of this information gathering. Thus, the determination of electromagnetic response of all kinds of objects is a fundamental problem. It is also a continuing problem because practical objects of interest are continually undergoing evolutionary changes.

The classical approach to electromagnetic scattering problems is an analysis based on the differential equations for the fields, together with the boundary conditions at the scatterer. For the most part, this work has been confined to a single, but arbitrary, frequency. Over the past seventy years, workers have produced a number of invaluable results, however, the number of different shapes treated has been relatively small. Moreover, work of this type on other target shapes is becoming more and more difficult.

On the other hand, there has been relatively little work done on scattering problems with general time variation. Yet the most distinctive radar signature of objects surely

lies in the time variation of the scattered signal. Probably the most fundamental and useful result would be a good method for the computation of the field scattered by an arbitrary shape when the incident wave is an impulse. This scattered field is called the electromagnetic impulse response.

The impulse response is of interest for a number of reasons. First, the time dependent scattered field for any excitation can be found by a convolution of the excitation with the impulse response. Second, the frequency response can be obtained by taking the Fourier transform of the impulse response. Third, the impulse response is useful in analyzing the return from targets illuminated by broadband spread-spectrum type radar systems. One particular radar system of this type is the broadband noise radar under study at Purdue University. In this radar system the output is closely related to the impulse response of the target. Fourth, the impulse response itself may be used as a characteristic function of the scattering object.

1.2 Survey of Literature

A number of workers have estimated the impulse response for various scattering objects, apparently the first being that by Kennaugh and Cosgriff (1958). They used the physical optics approximation to calculate the far zone approximate impulse response for the backscatter direction of a rectangular flat plate, sphere, and spheriod. They

modified their first results by making them satisfy the so-called moment conditions to give a better approximation. Kennaugh (1961) improved the result for a sphere by using the known sinusoidal steady state response to find the approximate impulse response for an incident pulse train that was synthesized by a Fourier series. Kennaugh and Moffatt (1962) approximated the backscatter impulse response of a cone sphere for an axial incident wave by combining the physical optics approximation with the approximate impulse response of a sphere. Using this approximate impulse response they obtained the axial echo area of the cone sphere with good results. Barabanenkov et al (1963) used the physical optics approximation to find the approximate impulse response in the backscatter direction of a sphere, disc, and cylinder. The technique they used is essentially the same as Kennaugh and Cosgriff (1958) used except Kennaugh and Cosgriff improved on the physical optics result by applying the moment conditions. Moffatt and Kennaugh (1965) obtained the approximate backscatter impulse response of a prolate spheriod with an axial incident wave. They did this by "stretching" the approximate ramp response of a sphere to obtain the approximate ramp response of the spheriod and then differentiating the ramp response twice. The backscatter impulse response of the flat-based right-circular cone for an axial incident wave was approximated by Kennaugh and Moffatt (1965) by combining results from

the physical optics approximation, theory of geometric diffraction, and moment conditions. Also, Weeks (1967) used the physical optics approximation and the reciprocity theorem to calculate the approximate impulse response in the far field for a number of simple objects.

Rheinstein (1968) computed the short pulse response of both conducting and dielectric spheres by using the rigorously computed frequency domain results. In addition he compared his results with some approximate theories. Also in 1968 Hong and Borison reported on experimental measurements of short pulse scattering by a blunt nose flat-backed cone in which separate returns from the nose and the back edge were clearly present.

Transient scattering of acoustic waves by infinite cylindrical structures has been quite widely studied and much of the work is referenced in Friedlaender (1958). However, it appears that analytical solutions exist for only simple shapes such as the wedge and cylinder. Diffraction of sound pulses by cylindrical obstacles of arbitrary cross section has been considered by Friedman and Shaw (1962). They developed an integral equation for the velocity potential on the surface and then solved this equation numerically for a square cylinder. However, it appears that the concept of impulse response in acoustics has not been exploited.

The previous work may be broken into two classes. In the first, the classical technique was used to find the

exact response for a sinusoidal steady state input and from this the approximate impulse response was computed. In the classical technique for finding the response, the problem is solved by expanding the solution in a series of eigenfunctions and matching the boundary conditions to determine the unknown coefficients. This approach is probably superior to any other approach when it can be applied. However, the serious deficiency lies in the fact that the exact frequency response can be found for only a small number of simple shapes.

The second approach used the physical optics approximation (sometimes along with other approximations) to obtain the approximate impulse response. In the physical optics approximation, the currents on the scatterer are assumed to be due only to the incident field, and no account is taken of the interaction between currents flowing at different points on the scatterer. This assumption certainly is not valid when the scatterer is a concave body, as in the case of a corner reflector. In this case it is obvious that currents at one point on the scatterer will affect the currents at other points on the scatterer. If some other approximations are used along with the physical optics approximation, the effect of currents interacting may be at least partially taken into account. However, the worth of these additional approximations is very hard to judge. Moreover, the application of the additional approximations

is quite difficult for the general case.

Although it has not been carried out to date, a third approach would be to find the response for a sinusoidal steady state input by numerical techniques. For example, the numerical techniques of Oshiro and Su (1965) or Andreasen (1964) could be used. The approximate impulse response would then be found by synthesizing an incident pulse train with a Fourier series. The advantage of this approach would be that the approximate impulse response could be found for a large number of objects. However, the overriding disadvantage is that the process would be very arduous and time consuming since the frequency response would have to be computed at a large number of frequencies to obtain a good approximation to an incident pulse train.

1.3 General Outline

This thesis considers a fourth approach for computing the approximate electromagnetic impulse response of conducting scatterers. An integro-differential equation in the time domain is developed for the current density (or magnetic field intensity) on the surface of an arbitrarily shaped scatterer. Moreover, it is demonstrated that the resulting equation can be solved numerically in the time domain by treating some interesting shapes.

In Chapter 2 a time domain integro-differential equation is developed for the magnetic field intensity at the surface of a cylindrical scatterer with arbitrary cross

section. In the same Chapter a second time domain integro-differential equation is formulated for the current density at the surface of an arbitrarily shaped three dimensional scatterer.

The equation for cylindrical scatterers is then solved numerically in Chapter 3 for the case of a circular cylinder with an approximate incident plane impulse to illustrate that numerical solution is feasible and, in fact, gives good results. Later in Chapter 3 the approximate impulse response is obtained for both a strip and a corner reflector.

In Chapter 4 the integro-differential equation for the current density on the surface of a sphere is solved numerically for an approximate incident plane impulse. Then the resulting far scattered field is computed numerically giving an approximate impulse response of the sphere and at the same time demonstrating that numerical solution is feasible and gives good results. Later in Chapter 4 the approximate impulse response is obtained for a finite cylinder with hemispherical caps. Chapter 5 is devoted to the presentation of conclusions and recommendations for further study.

CHAPTER 2

DERIVATION OF INTEGRO-DIFFERENTIAL EQUATIONS

2.1 General Scattering Problem

The general problem toward which this research is directed is the scattering of an electromagnetic wave by a perfectly conducting body. This is shown pictorially in Figure 2.1, where $\vec{H}^i$ is the incident magnetic field. The incident field is defined to be the field that would exist if the scatterer were not present. The total field that results with the scatterer present is denoted by $\vec{H}$. The scattered field $\vec{H}^s$ is then defined as

$$\vec{H}^s \equiv \vec{H} - \vec{H}^i \quad .$$

A physical interpretation is that the incident field induces current on the surface of the scatterer in such a way that the boundary conditions are satisfied. The scattered field is then produced by these induced currents.

By applying the equivalence principle (pp 106-110 Harrington, 1961) the problem in Figure 2.1 may be replaced by a problem which is equivalent, as shown in Figure 2.2. In the equivalent statement of the problem the currents are radiating in free space. Thus, the free space Green's function may be used to find the expression for the total

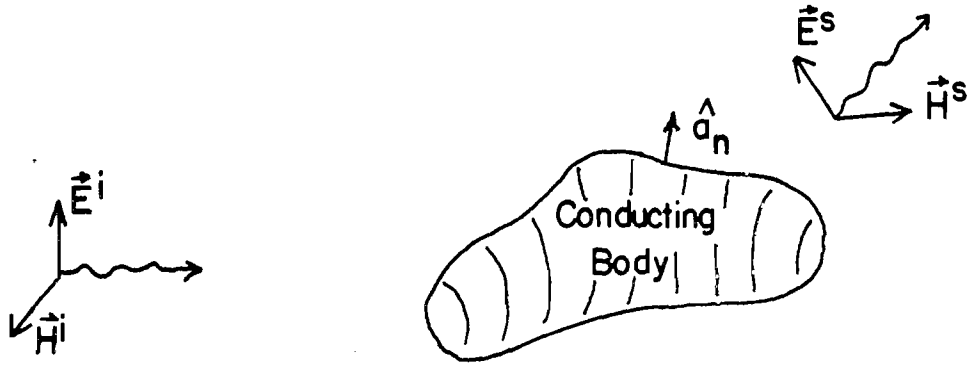

FIGURE 2.1 GENERAL SCATTERING PROBLEM

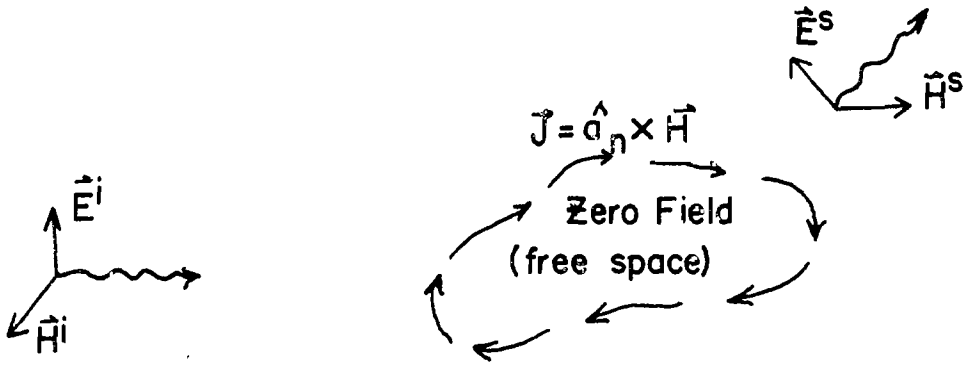

FIGURE 2.2 EQUIVALENT OF GENERAL SCATTERING PROBLEM

field at an arbitrary point in space. But since the current on the scatterer is in terms of the total field there, then an integro-differential equation for the current (or total field) on the surface of the scatterer may be obtained by selecting observation points at the surface of the scatterer.

It is convenient at this point to break the problem into two cases. The first case, scattering by a generalized cylindrical scatterer, is considered in Section 2.2. The second case, scattering by a finite three dimensional body of aribtrary shape, is treated in Section 2.3.

2.2 Generalized Cylindrical Scatterers

This Section considers the scattering of plane waves at arbitrary incidence on parallel cylindrical conductors with arbitrary cross section. It should be noted that this is not strictly a two dimensional problem but that it can be reduced to the same form as that of scattering with normal incidence, which is a two dimensional problem. If the incident wave is not plane, then the technique developed in Section 2.3 would have to be used.

Consider a plane wave incident on a cylindrical scatterer whose sides are parallel to the z-axis as shown in Figure 2.3. The incident Poynting vector makes an angle θ_i with the negative z-axis. At each point on the surface of the scatterer an orthogonal set of unit vectors $(\hat{a}_1, \hat{a}_2, \hat{a}_z)$ is defined. The vector $\hat{a}_1$ is the unit outward normal

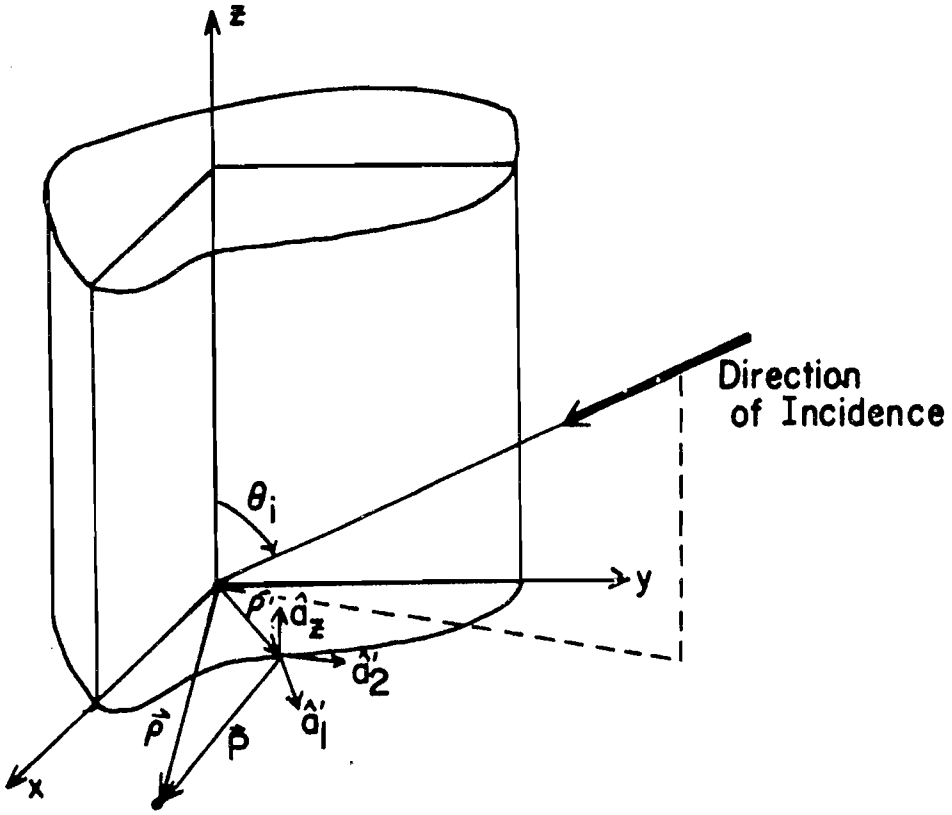

FIGURE 2.3 GEOMETRY OF CYLINDRICAL SCATTERING PROBLEM

to the surface and the vector $\hat{a}_z$ is the usual unit vector in the z-direction. Finally, the vector $\hat{a}_2$ lies in the z = constant plane and is tangent to the surface such that $(\hat{a}_1, \hat{a}_2, \hat{a}_z)$ forms a right hand system.

The Green's function for the i^{th} component of the vector potential at $(\vec{r},t)$ due to a point source at $(\vec{r}',t')$ is (pg. 838 Morse and Feshbach, 1953)

$$g(\vec{r},t;\vec{r}',t') = \frac{\delta(R/c - (t - t'))}{4\pi R} \; ; \quad R, (t - t') > 0 \; ,$$

where

$$\vec{r} = x\hat{a}_x + y\hat{a}_y + z\hat{a}_z$$

$$\vec{r}' = x'\hat{a}_x + y'\hat{a}_y + z'\hat{a}_z$$

$$R = |\vec{r} - \vec{r}'|$$

$$c = 1/\sqrt{\mu \varepsilon} \quad .$$

Thus, the vector potential due to the currents on the surface of the scatterer is

$$\vec{A}(\vec{\rho},z,t) = \frac{1}{4\pi} \int\int\int \frac{\vec{J}(\vec{\rho}',z',t')}{R} \delta(R/c - (t - t'))dz'ds'dt'.$$

(Note that the vector potential used here is defined so that $\vec{H} = \nabla x\vec{A}$ rather than $\vec{B} = \nabla x\vec{A}$.) But since the structure is of infinite length and the incident wave makes an angle of θ_i with the z axis, then

$$\vec{J}(\vec{\rho}',z',t') = \vec{J}(\vec{\rho}',z,t' - \frac{z - z'}{c} \cos\theta_i) .$$

Hence, it is possible to perform the z' integration analytically. The crucial step is to change variables

$$\tau = t' - \frac{z - z'}{c} \cos\theta_i .$$

The expression for $\vec{A}$ then becomes

$$\vec{A}(\vec{\rho},z,t) =$$

$$\frac{1}{4\pi} \int ds' \int d\tau\ \vec{J}(\vec{\rho}',z,\tau) \int_{-\infty}^{\infty} dz' \frac{\delta[\frac{R + (z - z')\cos\theta_i}{c} - (t-\tau)]}{R} .$$

Since $\vec{J}$ at $(\vec{\rho},z)$ differs from $\vec{J}$ at $(\vec{\rho},z')$ by only a shift in time there is no loss in generality by considering currents in the plane z = 0. Hence, $\vec{A}(\vec{\rho},z,t)$ is written as

$$\vec{A}(\vec{\rho},t) =$$

$$\frac{1}{4\pi} \int ds' \int d\tau\ \vec{J}(\vec{\rho}',\tau) \int_{-\infty}^{\infty} dz' \frac{\delta[\frac{R + (z - z')\cos\theta_i}{c} - (t - \tau)]}{R} ,$$

where $\vec{A}(\vec{\rho},t)$ and $\vec{J}(\vec{\rho},t)$ are $\vec{A}(\vec{\rho},0,t)$ and $\vec{J}(\vec{\rho},0,t)$, respectively.

Performing the z' integration gives (see Appendix I)

$$\vec{A}(\vec{\rho},t) = \frac{c}{2\pi}\int_s ds' \int_{t'=-\infty}^{t-\frac{P\sin\theta_i}{c}} \frac{\vec{J}(\vec{\rho}',t')}{\sqrt{c^2(t-t')^2 - P^2\sin^2\theta_i}}\,dt' ,$$

where the dummy variable τ has been replaced by t', s is the scatterer contour, and $P = |\vec{\rho} - \vec{\rho}'|$.

The total field $\vec{H}$ is just

$$\vec{H}(\vec{\rho},t) = \vec{H}^i(\vec{\rho},t) + \nabla x\vec{A}(\vec{\rho},t) .$$

Working out $\nabla x\vec{A}$ gives (see Appendix II)

$$\vec{H}(\vec{\rho},t) = \vec{H}^i(\vec{\rho},t)$$

$$+ \frac{c\sin\theta_i}{2\pi}\int_s ds' \int_{t'=-\infty}^{t-\frac{P\sin\theta_i}{c}} \frac{dt'}{\sqrt{c^2(t-t')^2 - P^2\sin^2\theta_i}} \left[\frac{\vec{J}(\vec{\rho}',t')}{c(t-t') + P\sin\theta_i}\right.$$

$$\left. + \frac{1}{c}\frac{\partial\vec{J}(\vec{\rho}',t')}{\partial t'}\right] x\hat{a}_p \qquad (2.1)$$

where

$$\hat{a}_p = \frac{\vec{\rho} - \vec{\rho}'}{P} .$$

To obtain an integro-differential equation from (2.1) it is necessary to shrink $\vec{\rho}$ to a point $\vec{\rho}''$ on the surface of the scatterer:

$$\vec{H}(\vec{\rho}",t) = \vec{H}^i(\vec{\rho}",t) + \lim_{\vec{\rho}\to\vec{\rho}"} \frac{c \sin\theta_i}{2\pi} \int_S ds' \int_{t'=-\infty}^{t - \frac{P\sin\theta_i}{c}} \frac{dt'}{\sqrt{c^2(t-t')^2 - P^2\sin^2\theta_i}}$$

$$\cdot \left[\frac{\vec{J}(\vec{\rho}',t')}{c(t-t') + P\sin\theta_i} + \frac{1}{c}\frac{\partial \vec{J}(\vec{\rho}',t')}{\partial t'}\right] x\hat{a}_p \quad . \quad (2.2)$$

Now break $\vec{H}$ into components

$$\vec{H} = \hat{a}_1 H_1 + \hat{a}_2 H_2 + \hat{a}_z H_z \quad ,$$

and compute $\vec{J}$ by applying the boundary condition $\vec{J} = \hat{a}_1' x \vec{H}$ to obtain

$$\vec{J}(\vec{\rho}',t') = -\hat{a}_2' H_z(\vec{\rho}',t') + \hat{a}_z H_2(\vec{\rho}',t') \quad .$$

So (2.2) becomes

$$\vec{H}(\vec{\rho}",t) = \vec{H}^i(\vec{\rho}",t) + \lim_{\vec{\rho}\to\vec{\rho}"} \frac{c \sin\theta_i}{2\pi} \int_S ds'(\hat{a}_p x \hat{a}_2') \int_{t'=-\infty}^{t - \frac{P\sin\theta_i}{c}} \frac{dt'}{\sqrt{c^2(t-t')^2 - P^2\sin^2\theta_i}}$$

$$\cdot \left[\frac{H_z(\vec{\rho}',t')}{c(t-t') + P\sin\theta_i} + \frac{1}{c}\frac{\partial H_z(\vec{\rho}',t')}{\partial t'}\right]$$

$$+ \lim_{\vec{\rho} \to \vec{\rho}} \frac{c \sin\theta_i}{2\pi} \int_S ds' (\hat{a}_z \times \hat{a}_p) \int_{t'=-\infty}^{t - \frac{P \sin\theta_i}{c}} \frac{dt'}{\sqrt{c^2(t-t')^2 - P^2 \sin^2\theta_i}}$$

$$\cdot - \left[\frac{H_2(\vec{\rho}', t')}{c(t-t') + P \sin\theta_i} + \frac{1}{c} \frac{\partial H_2(\vec{\rho}', t')}{\partial t'} \right] . \qquad (2.3)$$

Expanding $\hat{a}_p$ in terms of

$$\hat{a}_p = \hat{a}_1'(\hat{a}_1' \cdot \hat{a}_p) + \hat{a}_2'(\hat{a}_2' \cdot \hat{a}_p) \quad ,$$

and substituting into (2.3) gives

$$\vec{H}(\vec{\rho}'', t) = \vec{H}^i(\vec{\rho}'', t)$$

$$+ \hat{a}_z \lim_{\vec{\rho} \to \vec{\rho}''} \frac{c \sin\theta_i}{2\pi} \int_S ds' (\hat{a}_1' \cdot \hat{a}_p) \int_{t'=-\infty}^{t - \frac{P \sin\theta_i}{c}} \frac{dt'}{\sqrt{c^2(t-t')^2 - P^2 \sin^2\theta_i}}$$

$$\cdot \left[\frac{H_z(\vec{\rho}', t')}{c(t-t') + P \sin\theta_i} + \frac{1}{c} \frac{\partial H_z(\vec{\rho}', t')}{\partial t'} \right]$$

$$+ \lim_{\vec{\rho} \to \vec{\rho}''} \frac{c \sin\theta_i}{2\pi} \int_S ds' (\hat{a}_z \times \hat{a}_p) \int_{t'=-\infty}^{t - \frac{P \sin\theta_i}{c}} \frac{dt'}{\sqrt{c^2(t-t')^2 - P^2 \sin^2\theta_i}}$$

$$\cdot \left[\frac{H_2(\vec{\rho}', t')}{c(t-t') + P \sin\theta_i} + \frac{1}{c} \frac{\partial H_2(\vec{\rho}', t')}{\partial t'} \right] . \qquad (2.4)$$

But since the normal component of $\vec{H}$ is zero by virtue of the boundary condition, then it is necessary to find only the tangential components of the $\vec{H}$-field (i.e., H_2 and H_z) at the surface of the scatterer. So (2.4) yields

$$H_z(\vec{\rho}",t) = H_z^i(\vec{\rho}",t)$$

$$+ \lim_{\vec{\rho} \to \vec{\rho}"} \frac{c \sin\theta_i}{2\pi} \int_s ds'(\hat{a}_1' \cdot \hat{a}_\rho) \int_{t'=-\infty}^{t - \frac{P \sin\theta_i}{c}} \frac{dt'}{\sqrt{c^2(t-t')^2 - P^2 \sin^2\theta_i}}$$

$$\cdot \left[\frac{H_z(\vec{\rho}',t')}{c(t-t') + P \sin\theta_i} + \frac{1}{c} \frac{\partial H_z(\vec{\rho}',t')}{\partial t'}\right] \qquad (2.5)$$

$$H_2(\vec{\rho}",t) = H_2^i(\vec{\rho}",t)$$

$$+ \lim_{\vec{\rho} \to \vec{\rho}"} \frac{c \sin\theta_i}{2\pi} \int_s ds'(\hat{a}_1" \cdot \hat{a}_\rho) \int_{t'=-\infty}^{t - \frac{P \sin\theta_i}{c}} \frac{dt'}{\sqrt{c^2(t-t')^2 - P^2 \sin^2\theta_i}}$$

$$\cdot \left[\frac{H_2(\vec{\rho}',t')}{c(t-t') + P \sin\theta_i} + \frac{1}{c} \frac{\partial H_2(\vec{\rho}',t')}{\partial t'}\right] , \qquad (2.6)$$

where $\hat{a}_1'$ is the unit normal at $\vec{\rho}'$ and $\hat{a}_1"$ is the unit normal at $\vec{\rho}"$.

Thus, H_2 and H_z are decoupled as expected, and so each component may be treated separately. Traditionally,

equation (2.5) is called the TE case and equation (2.6) is called the TM case. The limiting procedure in (2.5) and (2.6) is performed in Appendix III. The result is:

$$H_z(\vec{\rho}'',t) = 2H_z^i(\vec{\rho}'',t) + \frac{c \sin\theta_i}{\pi}\int_s ds'(\hat{a}_1'\cdot\hat{a}_\rho)\int_{t'=-\infty}^{t-\frac{P\sin\theta_i}{c}} \frac{dt'}{\sqrt{c^2(t-t')^2 - P^2\sin^2\theta_i}} \cdot \left[\frac{H_z(\vec{\rho}',t')}{c(t-t') + P\sin\theta_i} + \frac{1}{c}\frac{\partial H_z(\vec{\rho}',t')}{\partial t'}\right] \qquad (2.7)$$

$$H_2(\vec{\rho}'',t) = 2H_2^i(\vec{\rho}'',t) + \frac{c \sin\theta_i}{\pi}\int_s ds'(\hat{a}_1''\cdot\hat{a}_\rho)\int_{t'=-\infty}^{t-\frac{P\sin\theta_i}{c}} \frac{dt'}{\sqrt{c^2(t-t')^2 - P^2\sin^2\theta_i}} \cdot \left[\frac{H_2(\vec{\rho}',t')}{c(t-t') + P\sin\theta_i} + \frac{1}{c}\frac{\partial H_2(\vec{\rho}',t')}{\partial t'}\right] . \qquad (2.8)$$

Some observations about the integro-differential equation (2.7) are now made. They are:

1. Consider the first term $2H_z^i(\vec{\rho}'',t)$. On the "illuminated" part of the scatterer, this is the field that would be given by the physical optics

approximation. However, this formulation differs from the physical optics approximation even in this term because in the "shadowed" region the physical optics term is zero.

2. The second term may be interpreted as the field at $\vec{\rho}''$ due to currents flowing at other points on the scatterer. It is interesting to note that if $\hat{a}_p$ is tangential at $\vec{\rho}'$, then the current at $\vec{\rho}'$ contributes nothing to the field at $\vec{\rho}''$. This means, for example, that there is no direct interaction between currents flowing on the same flat surface.
3. It should also be noted that the effect of any interaction is delayed in time by at least $P \sin \theta_i / c$. It is this important fact that makes numerical solution of (2.7) and (2.8) feasible.

So equation (2.7) gives the total field at a point on the scatterer as the sum of $2H_z^i$ and the field due to currents that existed at past times at other points on the scatterer. The interpretation of equation (2.8) is the same.

The striking fact about this formulation directly in the time domain is that equations (2.7) and (2.8) may be solved numerically on a computer by stepping on in time. That is, with these equations the total H field can be calculated sequentially in time beginning when the incident field arrives at the scatterer. This is possible since the total field at some time t is given in terms of the incident

field at time t (which is known) and the total field at previous times (which has been computed).

In most applications, the quantity of importance is the scattered field at a great distance from the scatterer. This is often called the far field. When the distance from the scatterer becomes very large, P also becomes very large, and the contribution due to the first term in the square brackets of (2.1) becomes negligible. In this case (2.1) becomes

$$\vec{H}^s(\vec{\rho},t) =$$

$$\frac{\sin\theta_i}{2\pi}\int_s ds' \int_{t'=-\infty}^{t-\frac{P\sin\theta_i}{c}} \frac{dt'}{\sqrt{c(t-t') - P\sin\theta_i}\,\sqrt{c(t-t') + P\sin\theta_i}}$$

$$\cdot \frac{\partial \vec{J}(\vec{\rho}',t')}{\partial t'} \times \hat{a}_p \quad .$$

In addition for P very large,

$$\frac{1}{\sqrt{c(t-t') + P\sin\theta_i}} \longrightarrow \frac{1}{\sqrt{2\sin\theta_i\,\rho}}$$

$$\hat{a}_p \longrightarrow \hat{a}_\rho = \vec{\rho}/\rho$$

So the expression for the far field becomes

$$\vec{H}^s(\vec{\rho},t) =$$

$$\frac{1}{\sqrt{\rho}}\,\frac{1}{2\pi}\,\sqrt{\frac{\sin\theta_i}{2}}\int_s ds'\int_{t'=-\infty}^{t-\frac{P\sin\theta_i}{c}} \frac{dt'}{\sqrt{c(t-t')-P\sin\theta_i}}\,\frac{\partial\vec{J}(\vec{\rho}',t')}{\partial t'}\,x\hat{a}_\rho .$$

Applying the boundary condition to find $\vec{J}$ in terms of $\vec{H}$ and simplifying gives the following expression for the far scattered field

$$\vec{H}^s(\vec{\rho},t) =$$

$$\frac{1}{\sqrt{\rho}}\,\frac{1}{2\pi}\,\sqrt{\frac{\sin\theta_i}{2}}\,[\hat{a}_z\int_s ds'(\hat{a}_i'\cdot\hat{a}_\rho)\int_{t'=-\infty}^{t-\frac{P\sin\theta_i}{c}} \frac{dt'}{\sqrt{c(t-t')-P\sin\theta_i}}$$

$$\cdot\ \frac{\partial H_z(\vec{\rho}',t')}{\partial t'}$$

$$+\ \hat{a}_\phi\int_s ds'\int_{t'=-\infty}^{t-\frac{P\sin\theta_i}{c}} \frac{dt'}{\sqrt{c(t-t')-P\sin\theta_i}}\ \frac{\partial H_2(\vec{\rho}',t')}{\partial t'}] \qquad (2.9)$$

where

$$\hat{a}_\phi = \hat{a}_z x \hat{a}_\rho \ .$$

2.3 Three Dimensional Scatterers

The derivation of the integro-differential equation in this case differs somewhat from the cylindrical case although the basic approach is the same. As in the cylindrical case, the equivalent problem shown in Figure 2.2 is solved.

The vector potential due to any current distribution on a surface S is given by (pg. 428 Stratton, 1941)

$$\vec{A}(\vec{r},t) = \frac{1}{4\pi}\int_S \frac{\vec{J}(\vec{r}',t - R/c)}{R}\, dS'$$

where

S is the surface of the scatterer

$\vec{r}$ is the observation point

$\vec{r}'$ is the integration point

$R = |\vec{r} - \vec{r}'|$

$c = 1/\sqrt{\mu\,\varepsilon}$.

In the equivalent problem shown in Figure 2.2 the total $\vec{H}$ field is simply the sum of the incident field and the field produced by the induced currents, $\vec{J}$. Thus, the total $\vec{H}$ field is

$$\vec{H}(\vec{r},t) = \vec{H}^i(\vec{r},t) + \nabla x\vec{A}(\vec{r},t)$$

Working out $\nabla x\vec{A}$ gives (see Appendix IV)

$$\vec{H}(\vec{r},t) = \vec{H}^i(\vec{r},t)$$

$$+ \frac{1}{4\pi}\int\left[\frac{\vec{J}(\vec{r}',\tau)}{R^2} + \frac{1}{Rc}\frac{\partial\vec{J}(\vec{r}',\tau)}{\partial\tau}\right]_{\tau=t-R/c} x\hat{a}_R dS' \qquad (2.10)$$

where

$$\hat{a}_R = \frac{\vec{r} - \vec{r}'}{R} .$$

An integro-differential equation for $\vec{J}$ may be obtained by simply shrinking $\vec{r}$ to a point $\vec{r}''$ on the surface of the scatterer and then applying the boundary conditions to put $\vec{H}$ in terms of $\vec{J}$. It may be worth noting that alternatively an equation in terms of $\vec{H}$ can be obtained; however, the numerical computation of the far scattered field from $\vec{H}$ takes somewhat longer than it does using $\vec{J}$. Hence, the integro-differential equation was put in terms of $\vec{J}$. Shrinking $\vec{r}$ to $\vec{r}''$ yields

$$\vec{H}(\vec{r}'',t) = \vec{H}^i(\vec{r}'',t)$$

$$+ \lim_{\vec{r}\to\vec{r}''} \frac{1}{4\pi}\int_S\left[\frac{\vec{J}(\vec{r}',\tau)}{R^2} + \frac{1}{Rc}\frac{\partial\vec{J}(\vec{r}',\tau)}{\partial\tau}\right]_{\tau=t-R/c} x\hat{a}_R dS'. \qquad (2.11)$$

The limiting procedure for (2.11) is carried out in Appendix V. Using this result, (2.11) then reduces to

$$\vec{H}(\vec{r}'',t) = 2\vec{H}^i(\vec{r}'',t)$$

$$+ \frac{1}{2\pi}\int_S \left[\frac{\vec{J}(\vec{r}',\tau)}{R^2} + \frac{1}{Rc}\frac{\partial\vec{J}(\vec{r}',\tau)}{\partial\tau}\right]_{\tau=t-R/c} x\hat{a}_R dS' \quad . \qquad (2.12)$$

For convenience an orthogonal right hand system of unit vectors $(\hat{a}_1,\hat{a}_2,\hat{a}_3)$ is chosen for each point on the scatterer such that $\hat{a}_1$ is normal to the surface of the scatterer and $\hat{a}_2,\hat{a}_3$ are tangential to the surface of the scatterer. Equation (2.12) is put entirely in terms of $\vec{J}$ by applying the boundary condition

$$\vec{J}(\vec{r}'',t) = \hat{a}_1'' \times \vec{H}(\vec{r}'',t) \quad ,$$

giving

$$\vec{J}(\vec{r}'',t) = 2\hat{a}_1'' x \vec{H}^i(\vec{r}'',t)$$

$$+ \frac{1}{2\pi}\int_S \hat{a}_1'' x\left[\left\{\frac{\vec{J}(\vec{r}',\tau)}{R^2} + \frac{1}{Rc}\frac{\partial\vec{J}(\vec{r}',\tau)}{\partial\tau}\right\}_{\tau=t-R/c} x\hat{a}_R\right] dS' \quad . \qquad (2.13)$$

This is a vector integro-differential equation for the current density on the surface of the scatterer.

Some observations about this equation should be made. They are:

1. The term $2\hat{a}_1'' \times \vec{H}^i(\vec{r}'',t)$ is the current that would be given by the physical optics approximation on the

"illuminated" part of the scatterer. However, this formulation differs from the physical optics approximation even in this term because in the "shadowed" region the physical optics current is zero.

2. The second term on the right hand side of (2.13) may be interpreted as the current at $\vec{r}''$ due to currents flowing at other points on the scatterer. It is interesting to note that if the patch of surface at $\vec{r}'$ lies in the same plane as the patch of surface at $\vec{r}''$, then the current at $\vec{r}'$ contributes nothing to the current at $\vec{r}''$. This means there is no direct interaction between currents flowing at different points on the same flat surface.
3. The effect of any interactions is delayed by R/c. It is this important fact that permits the numerical solution of (2.13).
4. The three dimensional case differs from the cylindrical case because in the three dimensional case three coupled integro-differential equations must be solved.

As in the cylindrical case equation (2.13) may be solved numerically on the computer by stepping on in time. This is possible since the current at some time t is given in terms of the incident field at time t (which is known) and the current at previous times (which has been computed).

In most applications the quantity of interest is the far scattered field. When the distance from the scatterer,

R, is large then the contribution of the first term in the square brackets of (2.10) to the integral is negligible. In addition the following approximations can be made.

$$\frac{1}{R} \longrightarrow \frac{1}{r}$$

$$\hat{a}_R \longrightarrow \hat{a}_r \quad .$$

Thus, (2.10) reduces to the following expression for the far scattered field.

$$\vec{H}^s(\vec{r},t) = \frac{1}{4\pi rc} \int_S \left[\frac{\partial \vec{J}(\vec{r}',\tau)}{\partial \tau}\right]_{\tau=t-R/c} x\hat{a}_r dS' \quad . \qquad (2.14)$$

CHAPTER 3

NUMERICAL SOLUTION OF CYLINDRICAL PROBLEMS

3.1 Preliminary Discussion

The equations derived in Section 2.2 give the field on the surface of a general cylindrical scatterer due to a plane wave incident at an arbitrary direction. The special case of normal incidence permits a simpler interpretation of the results and is somewhat easier to implement (although extension of the numerical procedure to an arbitrary angle of incidence would be straightforward). Moreover, it is suspected that consideration of an arbitrary angle of incidence would not add appreciably to understanding of the scattering phenomena. Hence, the following discussion is limited to the case of normal incidence, i.e., $\theta_i = 90°$.

It is also convenient at this point to change the units of time from seconds to light meters where one light-meter is defined as the time it takes light moving at velocity c to travel a distance of one meter, i.e., $t_{new} = ct_{old}$. This change of units facilitates interpretation of the results; in addition it also removes the cumbersome factor c from the formulation.

For the new unit of time and the case of normal incidence, the integro-differential equations for the field

on the surface of the scatterer given in (2.7) and (2.8) become

$$H_z(\vec{\rho}'',t) = 2H_z^i(\vec{\rho}'',t) + \frac{1}{\pi}\int_s ds'(\hat{a}_1'\cdot\hat{a}_\rho)\int_{t'=-\infty}^{t-P} \frac{dt'}{\sqrt{(t-t')^2 - P^2}}\left[\frac{H_z(\vec{\rho}',t')}{(t-t')+P} + \frac{\partial H_z(\vec{\rho}',t')}{\partial t'}\right] \tag{3.1}$$

$$H_2(\vec{\rho}'',t) = 2H_2^i(\vec{\rho}'',t) + \frac{1}{\pi}\int_s ds'(\hat{a}_1''\cdot\hat{a}_\rho)\int_{t'=-\infty}^{t-P} \frac{dt'}{\sqrt{(t-t')^2 - P^2}}\left[\frac{H_2(\vec{\rho}',t')}{(t-t')+P} + \frac{\partial H_2(\vec{\rho}',t')}{\partial t'}\right] . \tag{3.2}$$

In addition the expression for the far scattered field given in (2.9) becomes

$$\vec{H}^s(\vec{\rho},t) = \frac{1}{\sqrt{\rho}}\frac{1}{2\pi\sqrt{2}}\left[\hat{a}_z\int_s ds'(\hat{a}_1'\cdot\hat{a}_\rho)\int_{t'=-\infty}^{t-P} \frac{dt'}{\sqrt{(t-t') - P'}}\frac{\partial H_z(\vec{\rho}',t')}{\partial t'}\right.$$

$$+ \quad \hat{a}_\phi \int_s ds' \int_{t'=-\infty}^{t-P} \frac{dt'}{\sqrt{(t-t') - P}} \frac{\partial H_2(\vec{\rho}', t')}{\partial t'}] \quad . \qquad (3.3)$$

3.2 Numerical Approximation of Integro-Differential Equation

3.2.1 Space Integration

It is important to observe that the space integration is essentially the integration of a periodic function, $f(\phi)$, (or for multiple scatterers a sum of periodic functions) over one period. This suggests that $f(\phi)$ may be represented by the Fourier series

$$f(\phi) = \frac{a_o}{2} + \sum_{m=1}^{\infty} a_m \cos m\phi + b_m \sin m\phi$$

where

$$a_m = \frac{1}{\pi} \int_0^{2\pi} f(\phi) \cos m\phi \, d\phi$$

$$b_m = \frac{1}{\pi} \int_0^{2\pi} f(\phi) \sin m\phi \, d\phi \quad .$$

If the Fourier series representation is possible, then the integral of $f(\phi)$ over one period is simply πa_o. The rectangular approximation for the integral giving a_o would

be

$$A_o = \frac{1}{\pi} \sum_{m=o}^{N-1} f\left(\frac{2\pi m}{N}\right) \frac{2\pi}{N}$$

where

N = number of subintervals taken in one period.

In fact, Hamming (1962) shows that a_o and A_o are related exactly by

$$a_o = A_o - 2 \sum_{m=1}^{\infty} a_{mN} \quad , \tag{3.4}$$

where a_{mN} is the $m \times N$ Fourier coefficient of $f(\phi)$. Thus, the error incurred using the rectangular approximation for the space integration is

$$\text{error} = 2\pi \sum_{m=1}^{\infty} a_{mN} \quad .$$

This equation not only indicates how large the error is, but it also indicates how many sample points must be taken to obtain a given error. That is, the number of sample points, N, must be chosen large enough so that the N^{th} Fourier coefficient of $f(\phi)$ is negligible.

Appendix VI shows that the Fourier series representations of the space integration arguments in (3.1), (3.2), and (3.3) are valid, and also that the absolute value of the resultant Fourier coefficients are less than $M/m^{2-\varepsilon}$ where ε is an arbitrarily small positive number and M is some positive number independent of m. Thus, the error incurred by using an N point rectangular approximation for

the space integration argument is essentially the N^{th} Fourier coefficient of the space integration argument.

One might ask if it is possible to do better by using a higher order polynominal approximation for the space integration. It is easy to show that the trapazoidal rule gives exactly the same results as the rectangular rule. The second order polynominal approximation, Simpson's rule, gives two possible results depending upon where the first sample point is taken, but there is no way of knowing which result is more accurate. Moreover, if the average of the two results is taken, then the answer given by the rectangular rule is obtained.

Hence, the rectangular rule was used for the space integration because of its simplicity, good accuracy, and ease with which errors could be estimated. In addition, it implies a method for choosing the number of sample points to make the error below some acceptable minimum.

3.2.2 Time Integration

The time integrations in (3.1) and (3.2) are essentially the same, and thus, it is sufficient to consider only one of these equations. For the purpose of this discussion consider the time integration in (3.1)

$$f(\vec{\rho}') = \hat{a}_1' \cdot \hat{a}_P \int_{t'=t_1}^{t-P} \frac{dt'}{\sqrt{t-t' - P}} \left[\frac{1}{\sqrt{t-t' + P}} \left\{ \frac{H(\vec{\rho}', t')}{t-t' + P} \right. \right.$$

$$+ \quad \frac{\partial H(\vec{\rho}',t')}{\partial t'} \}] \quad .$$

For the case when P is zero (i.e., $\vec{\rho}' = \vec{\rho}''$) the value of $f(\vec{\rho}')$ was obtained from (VI.6) in Appendix VI giving

$$f(\vec{\rho}'') \quad = \quad - \quad \frac{H_o}{2R}$$

where

R = radius of curvature of contour at $\vec{\rho}''$

H_o = $H(\vec{\rho}'',t)$.

Note that this result depends upon $H(\vec{\rho}'',t)$ which is the item to be computed. In order to obviate this difficulty, an estimate, using the value of $H(\vec{\rho}'',t-\Delta t)$ for $H(\vec{\rho}'',t)$, was first made for $f(\vec{\rho}'')$. The value of $H(\vec{\rho}'',t)$ was computed using this estimate for $f(\vec{\rho}'')$, and then a new value of $f(\vec{\rho}'')$ was calculated. This process could be iterated more times; however, one iteration was sufficient for the cases treated because the contribution of $f(\vec{\rho}'')$ to the total field was relatively small (less than 10 percent).

For the case when P is not zero, the time integration was broken into two parts so that the integration about the singularity at the upper limit could be handled numerically, i.e.,

$$f(\vec{\rho}') \quad = \quad \int_{t=t_1}^{t_N-\Delta t} \quad + \quad \int_{t_N=\Delta t}^{t-P}$$

where t_N was chosen such that

$$0 \leq t - P - t_N \leq \Delta t$$

Δt = time increment for the numerical integration.

The integration from t_1 to $(t_N - \Delta t)$ was carried out using Simpson's rule.

The integration near the singularity, I_2, where

$$I_2 = \int_{t_N-\Delta t}^{t-P} \frac{dt'}{\sqrt{t-t' - P}} \left[\frac{1}{\sqrt{t-t' + P}} \left\{\frac{H(\vec{\rho}',t')}{t-t' + P} + \frac{\partial H(\vec{\rho}',t')}{\partial t'}\right\}\right] \tag{3.5}$$

was performed analytically using the following procedure. The quantity within the square brackets of (3.5)

$$v(t') = \frac{1}{\sqrt{t-t' + P}} \left\{ \frac{H(\vec{\rho}',t')}{\sqrt{t-t' + P}} + \frac{\partial H(\vec{\rho}',t')}{\partial t'}\right\}$$

was approximated by the fourth order polynominal

$$v(t') = v_0 + v_1(t-t'-P) + v_2(t-t'-P)^2 + v_3(t-t'-P)^3 + v_4(t-t'-P)^4$$

and then integrated analytically to give

$$I_2 = 2\sqrt{t-t_{N-1}-P}\left[v_0 + \frac{1}{3} v_1(t-t_{N-1}-P) + \frac{1}{5} v_2(t-t_{N-1}-P)^2 + \frac{1}{7} v_3(t-t_{N-1}-P)^3 + \frac{1}{9} v_4(t-t_{N-1}-P)^4\right]$$

where

$$t_{N-1} = t_N - \Delta t \quad .$$

The far field time integration in (3.3) was somewhat simpler than the time integrations in (3.1) and (3.2) because in (3.3) the value of P is never zero. The techniques used for the time integration in (3.3) were the same as those used in (3.1) and (3.3) for the case when P is not zero.

3.2.3 Time Differentiation

The time derivative of the H field on the surface of the scatterer was computed numerically. This was done by approximating the H field with a fourth order polynominal and then differentiating the result analytically. The best approximation occurs when the derivative is evaluated near the middle of the five points used to compute the coefficients of the fourth order polynominal approximation. Hence, the numerical derivative was evaluated as close as possible to the center of these five points.

3.3 Numerical Solution

3.3.1 General Procedure

The general procedure for the numerical solution of (3.1) is essentially the same as the procedure for the solution of (3.2). Hence, it is sufficient to describe only the solution of (3.1). Discussion of the procedure for the

numerical solution of (3.1) is facilitated by considering the space-time picture of the problem as shown in Figure 3.1. The space coordinates are the usual x and y coordinates, and the time coordinate, t, is the vertical axis. The contour of the scatterer in space-time is then represented by the cylindrical surface shown. It is desired to find the field, $H(\vec{\rho},t)$, at all points on this cylindrical surface.

In order to numerically solve (3.1) for $H(\vec{\rho},t)$, it is necessary to choose points in space-time at which to compute $H(\vec{\rho},t)$. The cylindrical surface was broken into patches as shown in Figure 3.1 and the H field was computed at the center of each of these patches numerically using (3.1). The actual choice of the sample points is discussed in Section 3.3.2.

The general procedure for the numerical solution of (3.1) is as follows. The incident H field is assumed to be zero at the scatterer for all times less than some value t_o. Hence, the total H field on the surface is also zero for all times less than t_o. Suppose at $t_1 = t_o + \Delta t$ the incident H field just reaches the scatterer. Thus, at t_1 on part of the scatterer an H field that is simply twice the tangential component of the incident H field is set up. As time marches on, the incident H field envelops more of the scatterer and the field at each point is given by the incident field, which is known, and the field at other points on the scatterer at

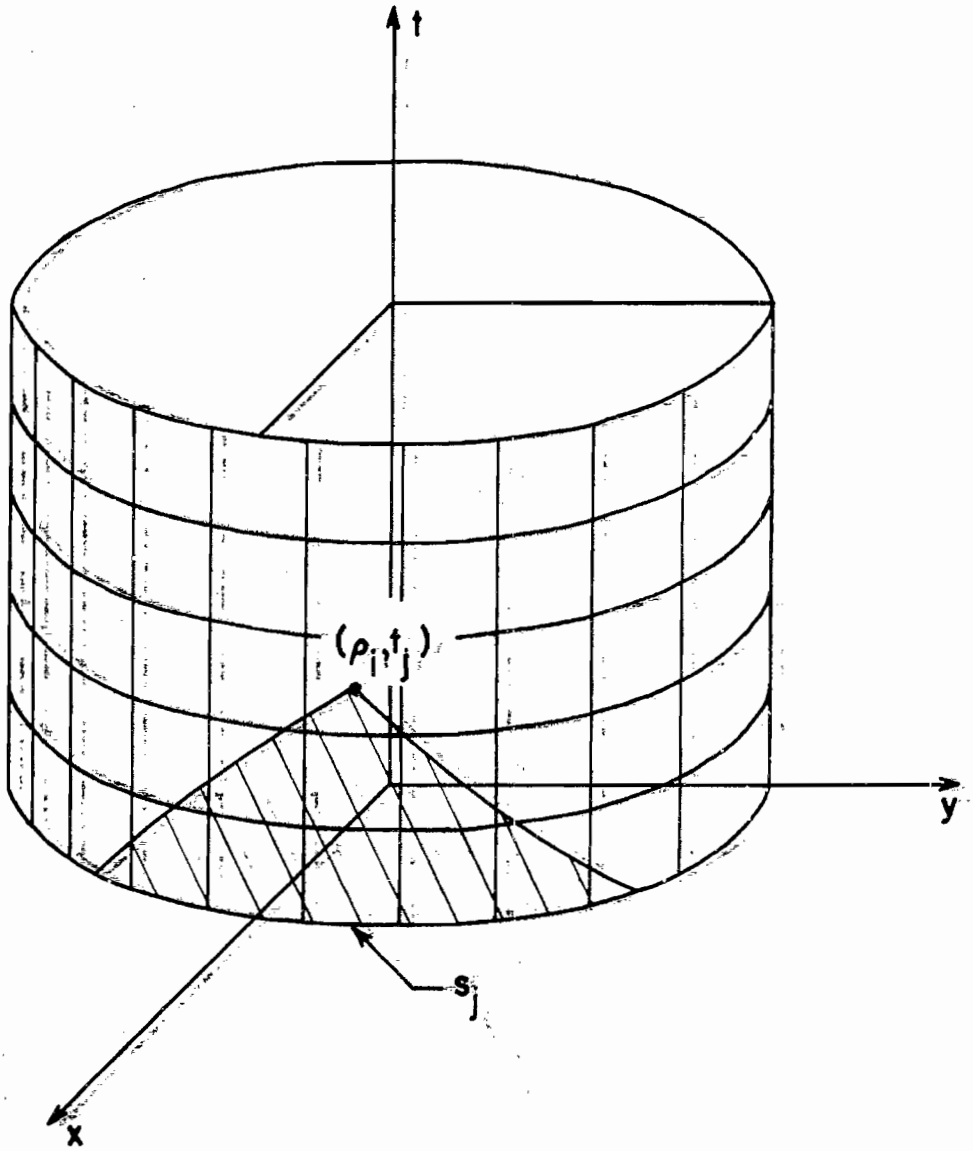

FIGURE 3.1 SPACE–TIME PICTURE OF SCATTERING PROBLEM

earlier times, which has been computed. So by simply marching on in time, the entire H field on the scatterer contour can be generated by using equation (3.1).

3.3.2 Choice of Sample Points in Space-Time

In this discussion it is assumed that both the scatterer and the incident H field are given. First consider a point (ρ_i, t_j) on the scatterer contour as shown in Figure 3.1. The cross-hatched region on the cylindrical space-time surface in Figure 3.1 is called the dependence domain of point (ρ_i, t_j) and is defined by

$$t < t_j - P$$

where

$$P = |\vec{\rho} - \vec{\rho}_i| \quad .$$

The H field at (ρ_i, t_j) depends on only the H field at points that lie in the dependence domain.

The numerical solution of (3.1) is performed by stepping on in time, and thus, the value of $H(\rho_{i\pm1}, t_j - P)$ must be known in order to compute the value of $H(\rho_i, t_j)$. But this is only assured if

$$t_j - P < t_j - \Delta t$$

where

Δt = the time increment.

Therefore, one restriction on the choice of sample points is

$$\Delta t < P_{min}$$

where

P_{min} is the minimum distance between space sample points. This says that the spacing in time must be less than the time it takes a wave, moving at the velocity of light, to travel between the closest space points.

As was pointed out in Section 3.2.1, the N sample points in space should be chosen such that the amplitude of the N^{th} Fourier coefficient of the space integration argument, $f(\phi)$, be negligible. In practice it is impossible to determine the argument of the space integration beforehand. Consequently, the time derivative of the incident H field set-up on the scatterer was used as an estimate of the argument of the space integration. Moreover, the points on the scatterer contour were chosen with approximately equal spacing to minimize computer time.

A fine time increment was used from the time the incident field arrived at the scatterer until the time the incident field passed the scatterer. The reason a fine time increment is necessary during the initial part of the sequential computation is as follows. In the integro-differential equation the total H field separates into two parts: (1) the incident H field which is the field that would exist if the scatterer were not present and (2) the scattered H field which is the field produced by the induced currents on the scatterer. However, on the shadow side of

the scatterer the incident field and the scattered field have opposite signs but equal or very nearly equal amplitudes during the initial period of time. This is because the total field, which is the sum of the incident field and the scattered field, is zero or near zero in this region of space-time. The greatest numerical error will occur in this region because there is a subtraction of two numbers which are large compared with their difference. Moreover, this error will be propagated since the numerical solution is obtained by stepping on in time. Thus, a fine time increment was used during the critical period of time to improve the accuracy. After the incident wave had passed the scatterer the normal time increment was used to reduce computer time.

3.4 Choice of Incident Field

Up to this point the only restrictions on the incident field have been that it reach the scatterer at some finite time in the past and that it has no variation with z, i.e., the previously described procedures may be applied to all cylindrical incident fields with arbitrary time variation. As noted in Chapter 1, the incident field of greatest interest is a plane impulse in space-time because solutions for all other plane incident fields may be obtained from the impulse response. Thus, in this work an approximation to a plane impulse was used for the incident $\vec{H}$ field, and the resulting scattered fields constitute an approximate

electromagnetic impulse response.

Three alternate approximations to the impulse are the Gaussian pulse,

$$\delta_n(t) = \frac{n}{\sqrt{\pi}} e^{-n^2t^2} ,$$

the sin (t) over t pulse,

$$\delta_n(t) = \frac{\sin nt}{\pi t} ,$$

and the polynominal pulse,

$$\delta_n(t) = \frac{n}{\pi(1+n^2t^2)} .$$

The Gaussian pulse approximation was chosen because it decays toward zero very rapidly as shown in Figure 3.2. The incident H field was taken to be

$$H^i(\vec{\rho},t) = \frac{n}{\sqrt{\pi}} e^{-n^2(t + x \cos \phi^i + y \sin \phi^i)^2}$$

where

ϕ^i = angle the Poynting vector of incident field makes with negative x-axis.

3.5 Relation Between Frequency Response and Approximate Impulse Response

The electromagnetic scattering problem can be considered a linear system with one input (the incident field) and many outputs (the resultant field at all points in space). Shown in Figure 3.3 is a block diagram of the linear system

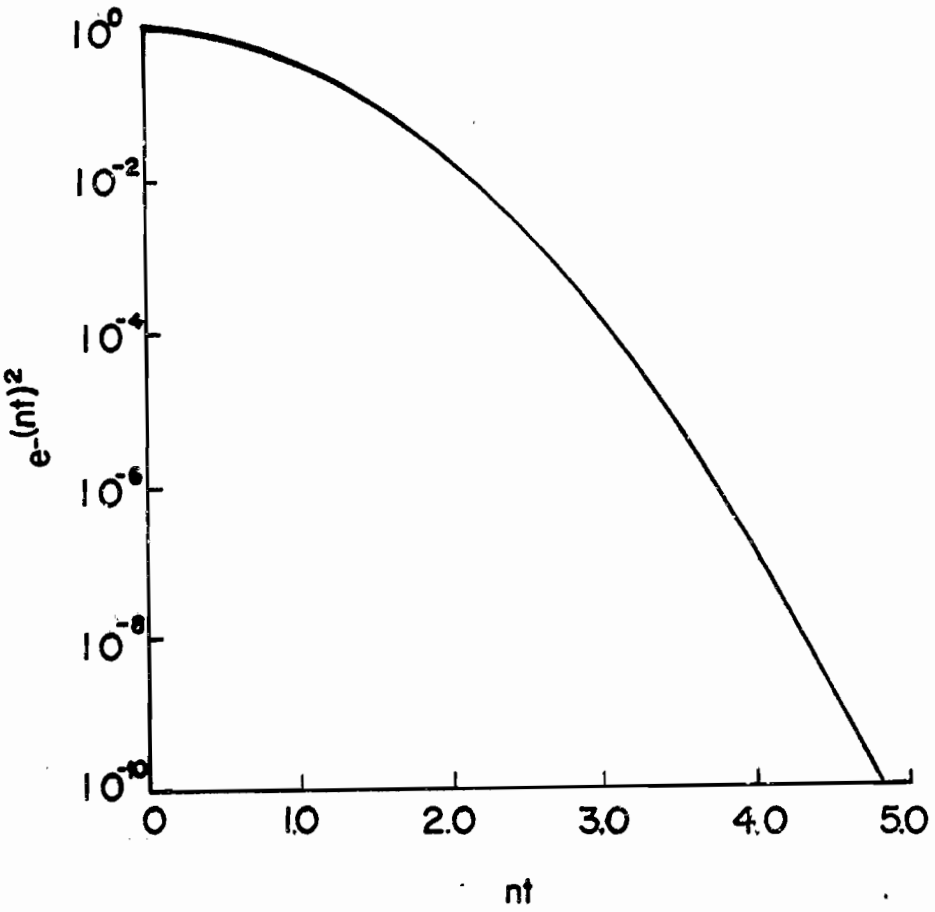

FIGURE 3.2 LOGARITHMIC PLOT OF GAUSSIAN PULSE SHOWING RAPID DECAY

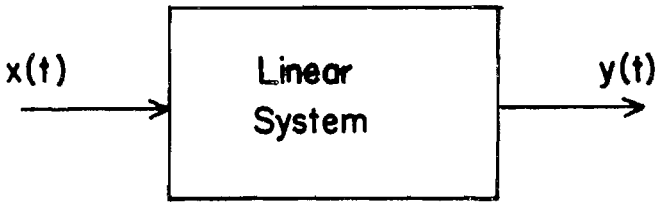

FIGURE 3.3 BLOCK DIAGRAM OF LINEAR SYSTEM

representation with only one of the outputs indicated.

In this study the input, $x(t)$, to the linear system was the approximate impulse

$$x(t) = \frac{n}{\sqrt{\pi}} e^{-n^2 t^2}$$

and the output, $y(t)$, was the approximate impulse response. The frequency response, $H(\omega)$, is simply the ratio of the Fourier transform of the output, $Y(\omega)$, to the Fourier transform of the input $X(\omega)$, i.e.,

$$H(\omega) = \frac{Y(\omega)}{X(\omega)} \qquad (3.6)$$

where

$$X(\omega) = e^{-(\frac{\omega}{2n})^2}$$

$$Y(\omega) = F\{y(t)\} \quad .$$

Hence, the frequency response may be obtained from the approximate impulse response by

$$H(\omega) = e^{(\frac{\omega}{2n})^2} F\{y(t)\} \quad . \qquad (3.7)$$

On the other hand, the approximate impulse response may be obtained from the frequency response by

$$y(t) = F^{-1}\{e^{-(\frac{\omega}{2n})^2} H(\omega)\} \qquad (3.8)$$

where

$F^{-1}\{\ \}$ indicates the inverse Fourier transform.

In this thesis the Fourier transform and inverse Fourier transform operations were performed numerically by using the finite Fourier transform computer program written by Cooley (1966).

It should be pointed out that there is an upper frequency limit for which the frequency response can be computed using (3.7). There are several reasons for this. First, the amplitude of the high frequency components of the incident field are small. Second, the numerical accuracy for higher frequency components is reduced because the error in the space integration is proportional to the N^{th} Fourier component of the integrand. Third, the error incurred in the numerical computation of the time derivative and its subsequent use in the analytical time integration becomes larger for the higher frequency components contained in the field. The results of this investigation indicate that satisfactory answers are obtained if as few as four space sample points occur in one wavelength.

3.6 Numerical Examples

3.6.1 Circular Cylinder

The feasibility of the actual numerical solution of the integro-differential equation was first demonstrated by considering the case of a circular cylinder. The circular cylinder was chosen as the test case for several reasons. First, the frequency response of a circular cylinder can be

obtained exactly by classical techniques, and thus, provided a check on the validity of the computer program and numerical techniques. And second, the choice of sample points on a circular cylinder was relatively straightforward.

The actual circular cylinder used for the test case had a radius of one meter as shown in Figure 3.4 and the incident field was the approximate impulse

$$H^i(\vec{\rho},t) = \frac{2}{\sqrt{\pi}} e^{-4(x+t)^2}$$

which possessed a width approximately equal to the diameter of the cylinder. The sample points on the cylinder were spaced every 15° or approximately every 0.25 meters. Finally, the fine time increment was chosen to be 0.1 lightmeters and the course time increment was taken as 0.2 lightmeters.

The total field on the surface of the scatterer was found by solving the integro-differential equation with the numerical procedure discussed in Section 3.3. This result, in turn, was used to numerically compute the far scattered field, which is the approximate impulse response.

In Figure 3.5 the approximate impulse response in the backscatter direction is shown for the TE case. The result calculated directly in the time domain using (3.1) and (3.3) is compared with the result obtained by performing an inverse Fourier transform of the classical frequency response solution as described in Section 3.5. As can be seen in

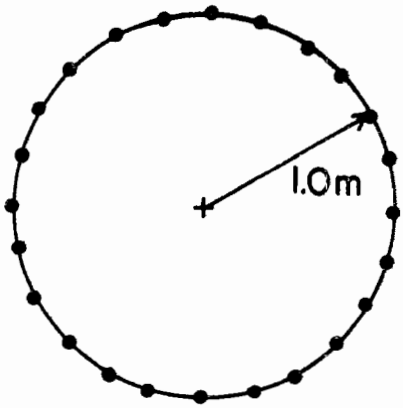

FIGURE 3.4 GEOMETRY OF CIRCULAR CYLINDER

Figure 3.5, the two results in the backscatter direction are essentially identical. The comparison of the approximate impulse response obtained by these two techniques for other directions was also very good.

The initial peak in Figure 3.5 corresponds to specular reflection from the front side of the cylinder and would have been predicted by geometric optics. The negative swing that follows is similar to what would be given by the physical optics approximation. And finally, the subsequent positive swing may be interpreted as due to a wave traveling around the backside of the cylinder. This wave is often called the creeping wave. The time of arrival of the second positive peak (at approximately 4.0 light-meters) indicates, in this case, that the velocity of the creeping wave is approximately 0.8 times the speed of light. An inspection of the current density on the surface of the scatterer does indeed reveal two pulses, one on each side of the scatterer, traveling from the illuminated region to the unilluminated region of the scatterer. These two pulses continue on into the shadow region, diminishing in amplitude as they go, until they meet at which time they coalesce and lose much of their shape and identity.

In Figure 3.6 the approximate impulse response in the backscatter direction is shown for the TM case. Again the result calculated directly in the time domain using (3.2) and (3.3) compares quite well with the result obtained by

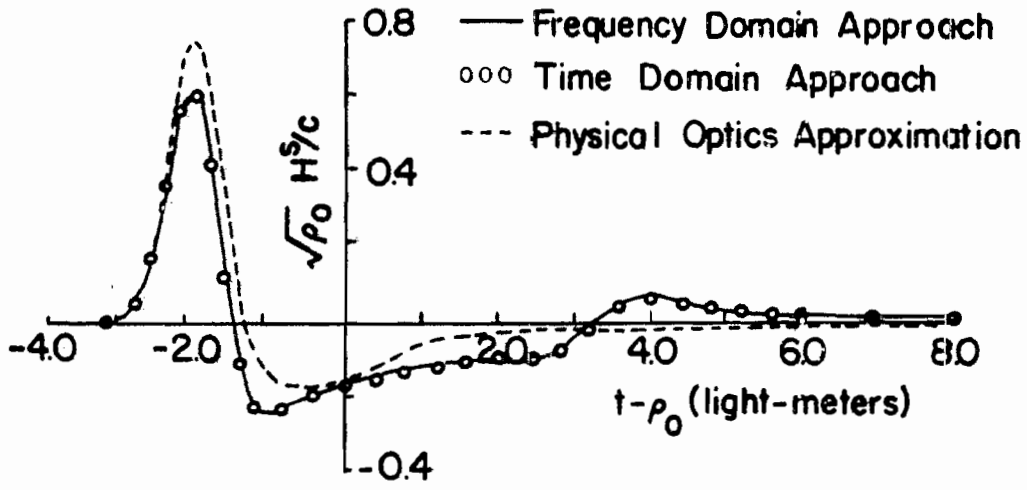

FIGURE 3.5 TE APPROXIMATE IMPULSE RESPONSE OF CIRCULAR CYLINDER IN BACKSCATTER DIRECTION

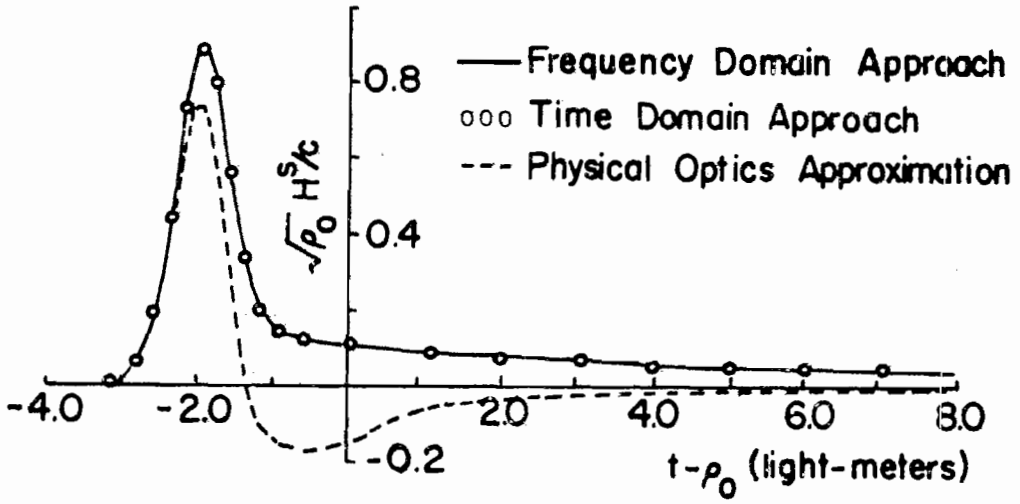

FIGURE 3.6 TM APPROXIMATE IMPULSE RESPONSE OF CIRCULAR CYLINDER IN BACKSCATTER DIRECTION

performing an inverse Fourier transform of the classical frequency response. However, the character of the back-scattered far field for the TM case is distinctly different from the TE case. The initial peak in the TM case, as in the TE case, corresponds to the specular reflection from the front side of the cylinder. However, the negative swing predicted by the physical optics approximation does not occur. Furthermore, there is no creeping wave contribution to the scattered field. This is not surprising since a creeping wave in the TM case would be similar to a horizontally polarized wave propagating over a conducting surface, which would be attenuated very rapidly. On the other hand, the creeping wave in the TE case would be similar to a vertically polarized wave propagating over a conducting surface, which would have very little attenuation.

The approximate electromagnetic impulse response of a circular cylinder for the TE case is shown in Figure 3.7 along with the incident pulse. This figure may be viewed as a "snapshot" of the waveforms in space, with all dimensions to scale, except the distance to the cylinder. The outer semi-circle represents the points in space that the peak of the incident pulse would have reached if it were reflected from the origin (the center of the cylinder in this case). The amplitude of the scattered H field is normalized by the multiplying factor of $\sqrt{\rho_0}$, where ρ_0 is the distance of the outer semi-circle from the origin. Each scattered field

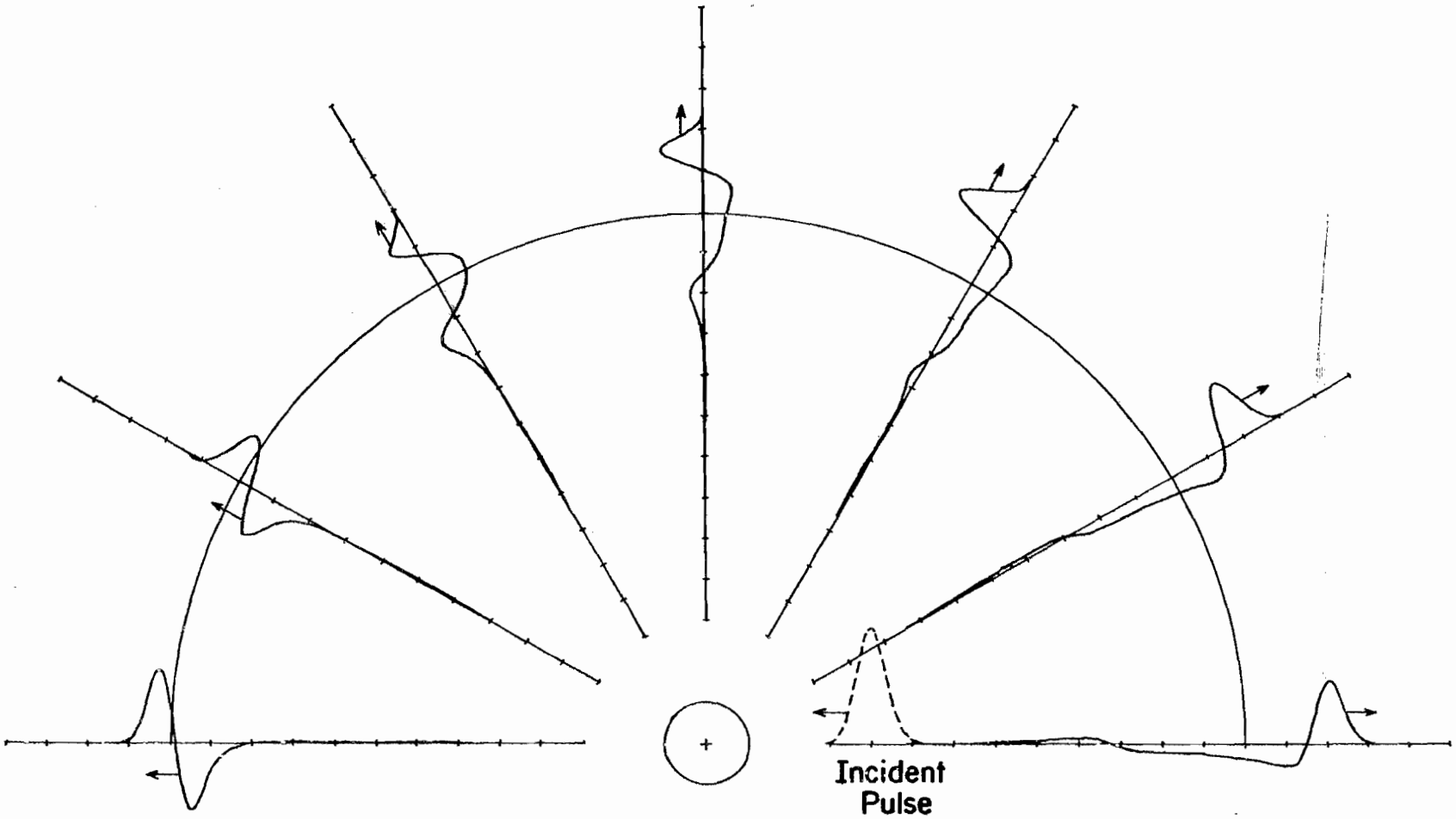

FIGURE 3.7 TE APPROXIMATE IMPULSE RESPONSE OF CIRCULAR CYLINDER

consists of an initial pulse which represents the contribution due to specular reflection and could be predicted by geometric optics. This initial pulse is followed by smaller pulses that may be interpreted as the wave traveling around the cylinder (creeping wave).

The approximate electromagnetic impulse response of a circular cylinder for the TM case is shown in Figure 3.8. As in the TE case, each scattered field consists of an initial pulse which represents the contribution due to specular reflection. However, there is no indication of a creeping wave contribution to the scattered field.

Finally, using the technique discussed in Section 3.5, the frequency response of the circular cylinder was computed from the approximate impulse response. The frequency response is plotted as a function of k where k is defined to be ω/c and ω is the radian frequency. In Figure 3.9 the TE result in the backscatter direction is compared with the classical frequency response. The comparison is excellent up to approximately $k = 6$, and satisfactory up to approximately $k = 8$. Hence, this technique gives acceptable results when as few as three sample points on the scatterer occur in a wavelength.

The TM frequency response calculated from the approximate impulse response in the backscatter direction is compared with the classical frequency response in Figure 3.10. The comparison is excellent from approximately $k = 0.2$ up

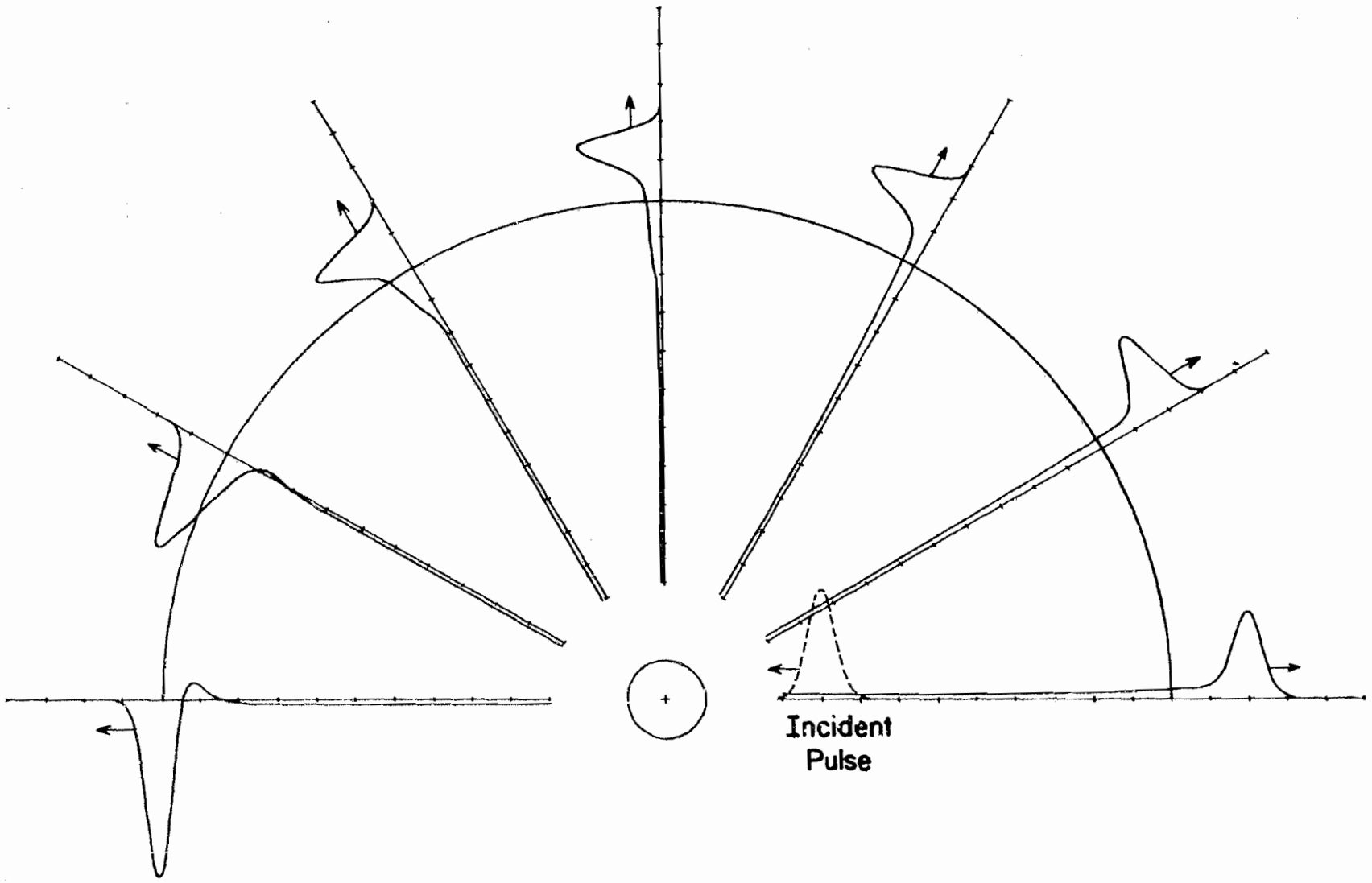

FIGURE 3.8 TM APPROXIMATE IMPULSE RESPONSE OF CIRCULAR CYLINDER

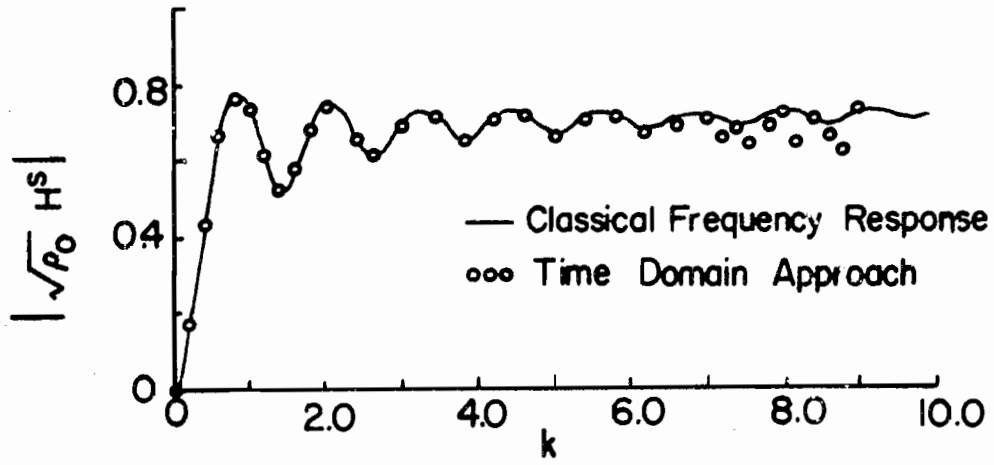

FIGURE 3.9 TE FREQUENCY RESPONSE IN BACKSCATTER DIRECTION OF CIRCULAR CYLINDER WITH ONE METER RADIUS

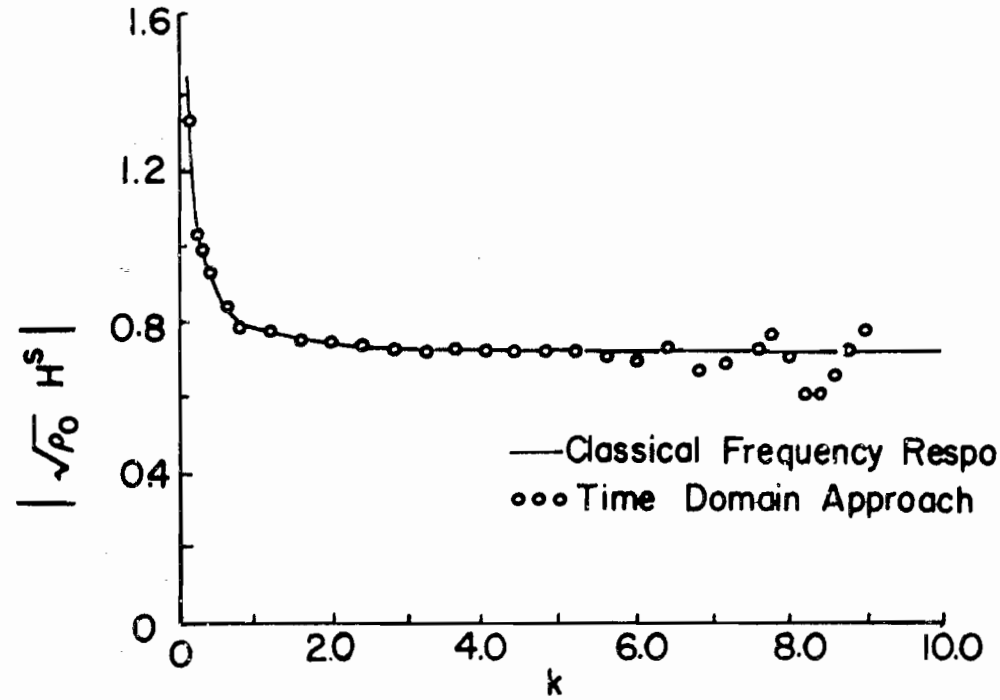

FIGURE 3.10 TM FREQUENCY RESPONSE IN BACKSCATTER DIRECTION OF CIRCULAR CYLINDER WITH ONE METER RADIUS

to k = 6. The error at low frequencies is due to the long "tail" occurring in the approximate impulse response. For the numerical computation of the Fourier transform, this tail of the approximate impulse response was extrapolated linearly to zero, giving rise to the small error at low frequencies. Figure 3.9 and Figure 3.10 indicate that the frequency response can be obtained over a wider range for the TE case than for the TM case by using this technique.

3.6.2 Strip

A strip with the cross-section shown in Figure 3.11 was the second shape considered. This shape was chosen to demonstrate the feasibility of numerical solution of the integro-differential equation for convex scatterers for which the frequency domain solution has not been obtained by classical techniques. Moreover, the strip geometry provides two flat surfaces which saves computer time since there is no direct interaction between currents on the same flat surface. Finally, the strip ends are circular cylinder halves, and thus, some interesting comparisons can be made between the approximate impulse responses of the strip and the circular cylinder. The sample points on the contour were chosen with a spacing of approximately 0.25 meters as indicated in Figure 3.11. The incident field and the time increments were taken to be the same as for the case of the circular cylinder.

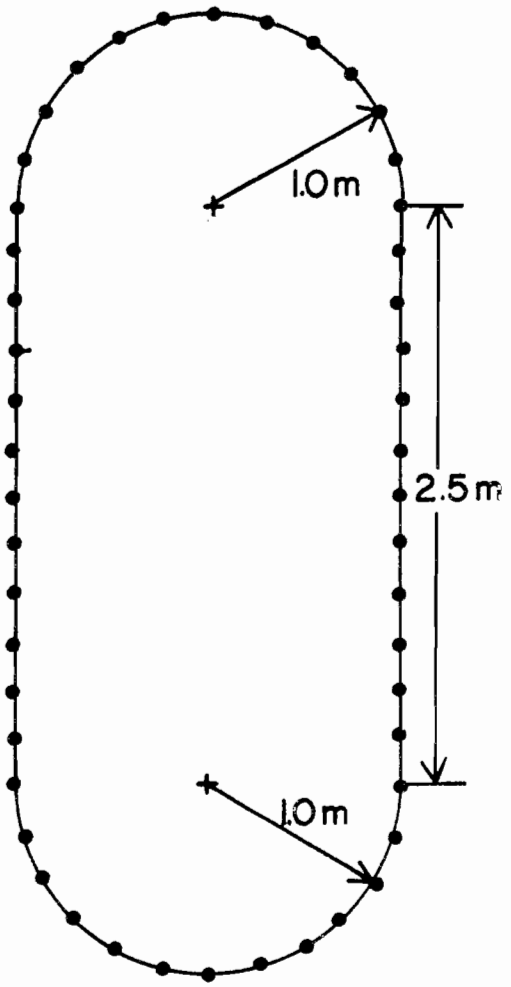

FIGURE 3.11 GEOMETRY OF STRIP

The approximate impulse response of the strip with broadside incidence is shown in Figure 3.12 for the TE case. As a test of the validity of the computer program and the accuracy of the results, the approximate impulse response of strip was again computed for end-on incidence as shown in Figure 3.13. By the time domain reciprocity theorem (Cheo, 1965), the scattered field should be the same if the direction of the incident field and the scattered field are interchanged. As can be seen in Figure 3.13, the numerical solution of the integro-differential equation gives results which agree very well with the time domain reciprocity theorem. That is, the field scattered off the end of the strip with broadside incidence in Figure 3.12 is the same as the field scattered off the side of the strip with end-on incidence in Figure 3.13.

Shown in Figure 3.14 and 3.15 for the TM case are the numerically computed approximate impulse responses of the strip with broadside incidence and end-on incidence, respectively. Again these numerical results agree well with the time domain reciprocity theorem.

A comparison of the approximate impulse response of the strip with the approximate impulse response of the circular cylinder is now made. Consider first the TE case with broadside incidence shown in Figure 3.12. In both the backscatter and forwardscatter directions the initial portion of the return from the strip is enhanced. In the

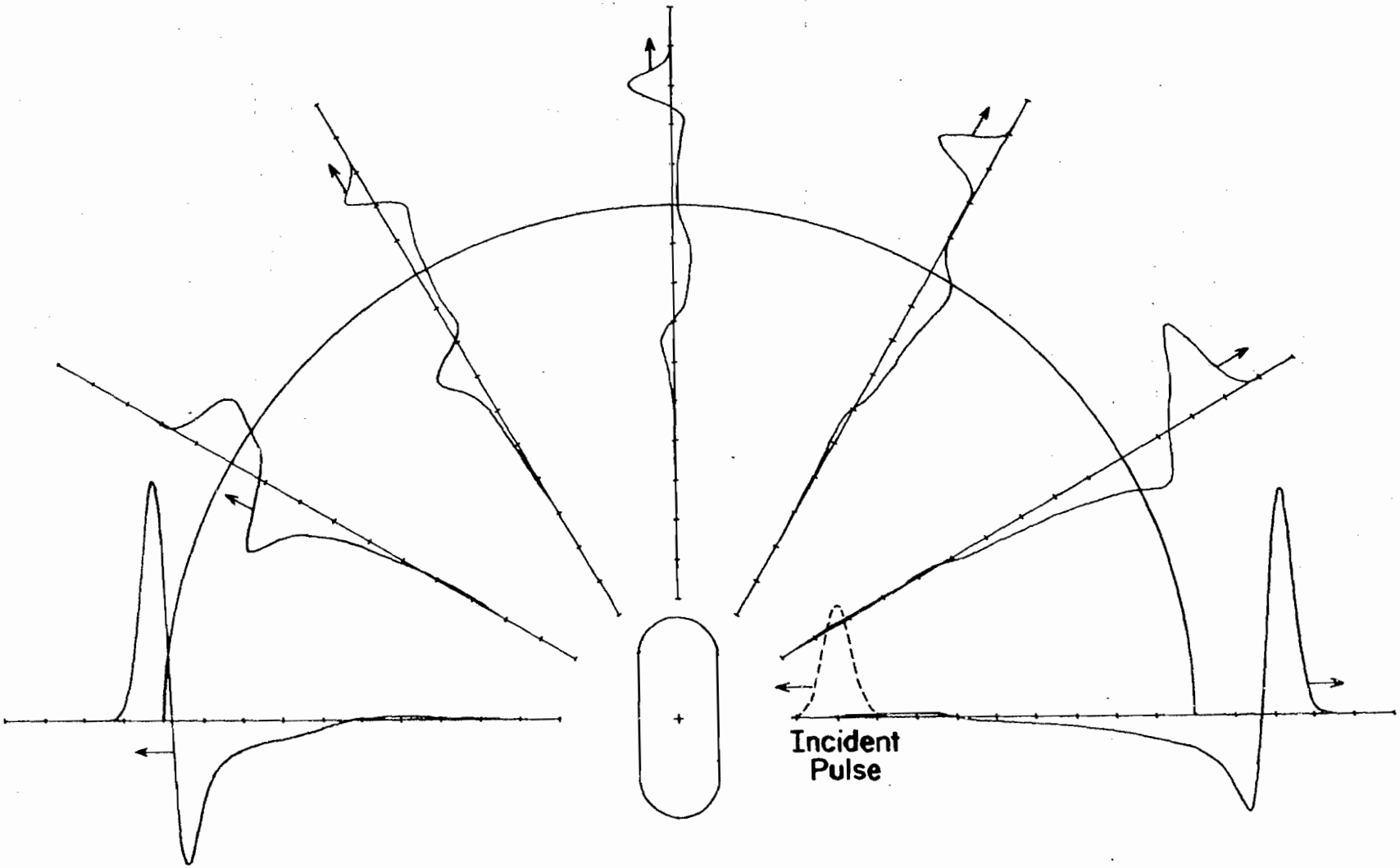

FIGURE 3.12 TE APPROXIMATE IMPULSE RESPONSE OF STRIP WITH BROADSIDE INCIDENCE

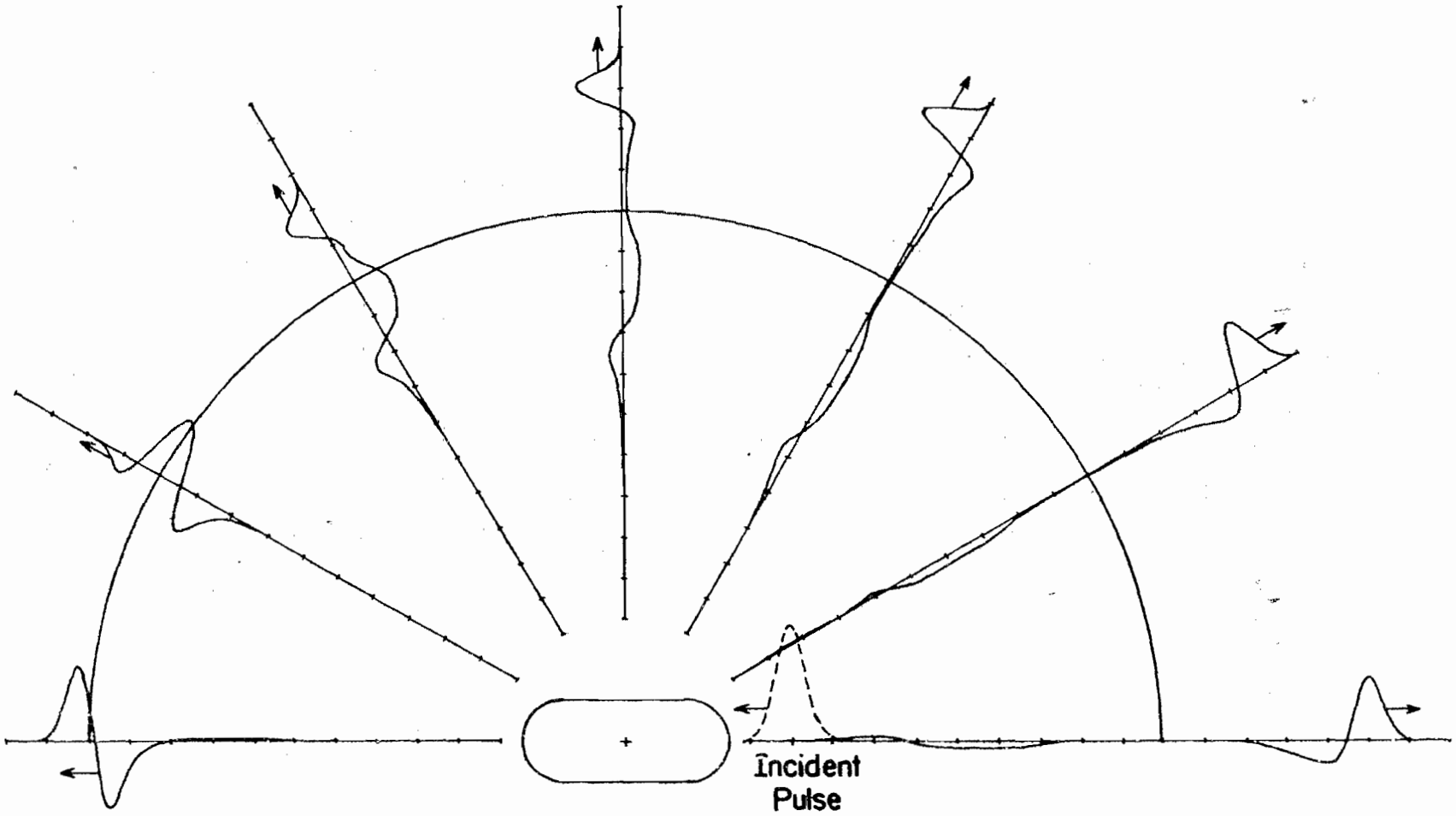

FIGURE 3.13 TE APPROXIMATE IMPULSE RESPONSE OF STRIP WITH END-ON INCIDENCE

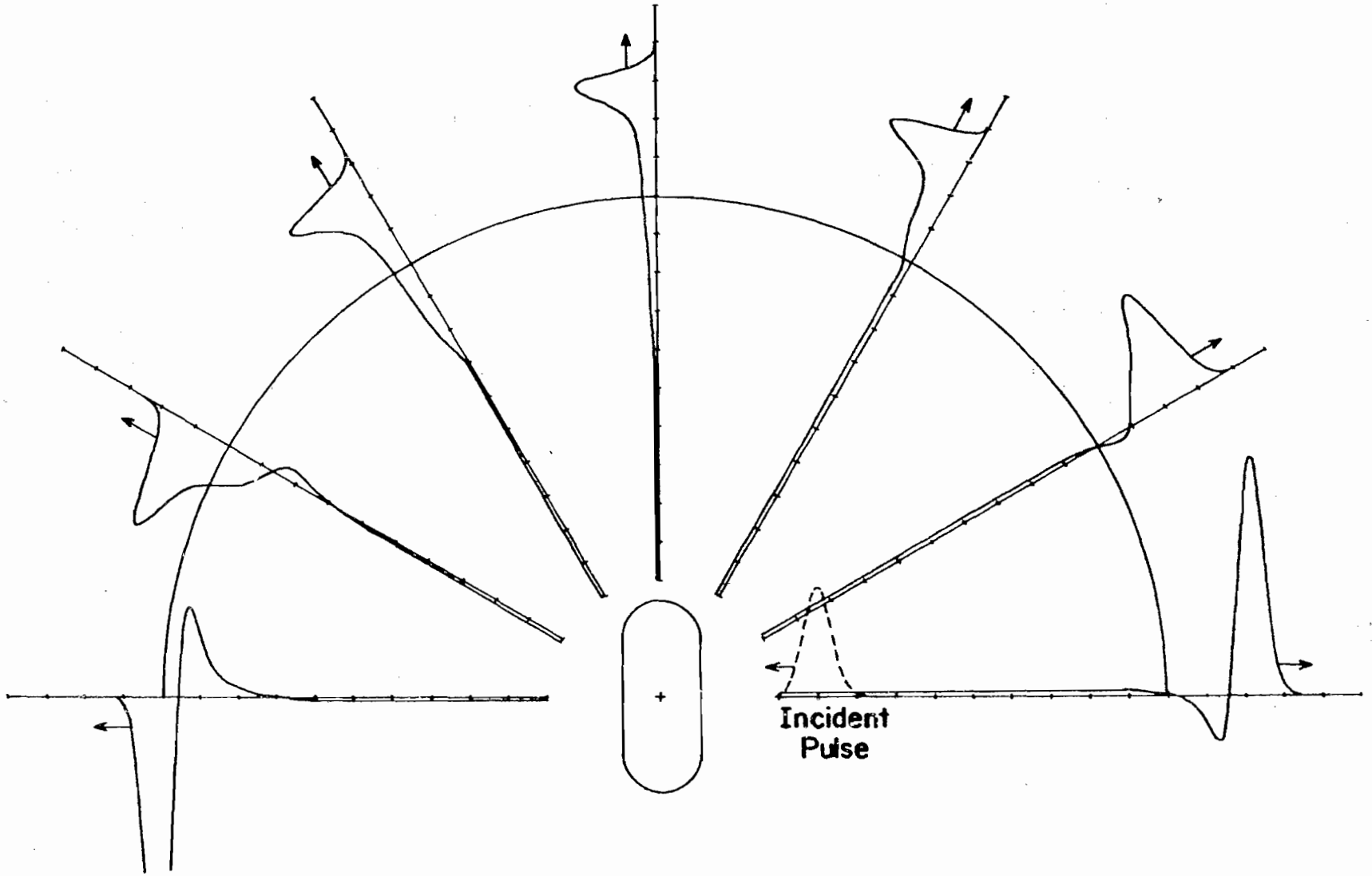

FIGURE 3.14 TM APPROXIMATE IMPULSE RESPONSE OF STRIP WITH BROADSIDE INCIDENCE

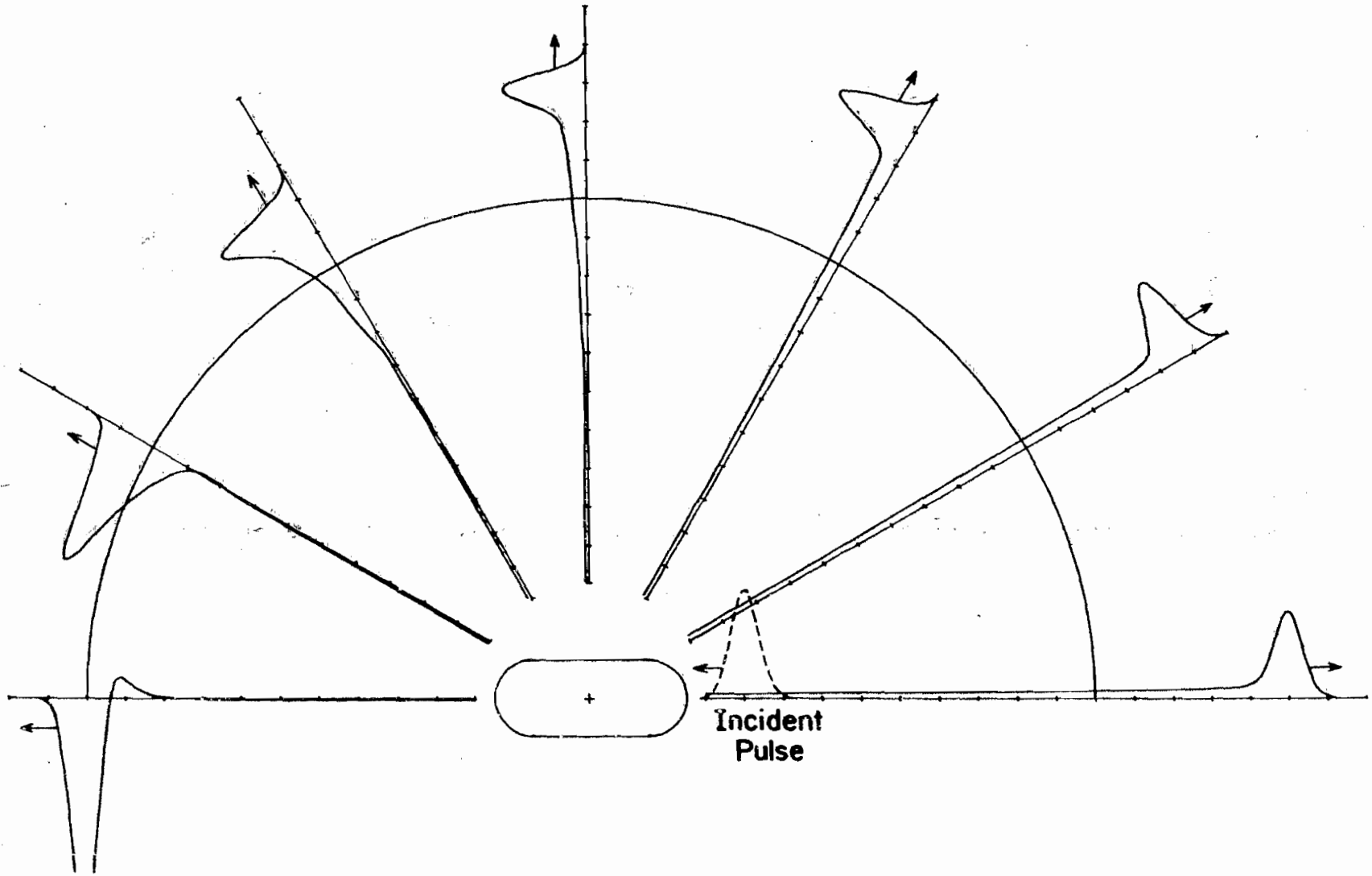

FIGURE 3.15 TM APPROXIMATE IMPULSE RESPONSE OF STRIP WITH END-ON INCIDENCE

backscatter direction the creeping wave contribution to the response of the strip has a shape very similar to the circular cylinder case, however, its magnitude is somewhat smaller. The time of arrival of the creeping wave contribution does indicate that the creeping wave velocity is between approximately 0.8 and 0.9 times the speed of light.

The TE case of the strip with end-on incidence is shown in Figure 3.13. The initial portion of the return is very close both in size and shape to the return from the circular cylinder. In fact, in the forward direction the entire response of the strip appears from the curve to be the same as for the circular cylinder. However, a closer examination of the numerical results reveals small differences which may be attributed to a wave traveling one and a half times around the structure. In the backscatter and near backscatter directions the near-zero region in the strip response indicates that the contribution due to the sides is very small for the TE case with end-on incidence. After this near-zero region in the strip response, a negative swing occurs. The timing of this negative swing indicates that it may be associated with the boundary between the flat side and the curved backside of the strip. Next, the response again swings positive. This may be attributed to a creeping wave traveling around the rear of the strip at approximately 0.8 times the speed of light.

The TM case of the strip with broadside incidence, shown in Figure 3.14, is less interesting than the TE case. The response of the strip is enhanced with respect to the response of the circular cylinder in both the backscatter and forwardscatter directions. However, the response in the other directions shown is not very different from the circular cylinder. It is interesting to note that the response of the strip in the backscatter direction possesses a negative swing as predicted by the physical optics approximation. This is reasonable since the physical optics approximation becomes better as the relative size of scatterer's flat region increases.

In Figure 3.15 is shown the TM case for the strip with end-on incidence. It is very striking how closely the response of the strip with end-on incidence is to the response of the circular cylinder for the TM case. In the backscatter direction the comparison is so good that differences cannot be detected in the plotted curves. However, inspection of the numerical results reveals that the magnitude of the tail is slightly larger for the case of the strip. In other directions the amplitudes of the returns from the strip are somewhat larger but the shapes remain very close to those of the circular cylinder.

The frequency response of the strip with broadside incidence is shown in Figure 3.16 for the backscatter direction. In this Figure it is noted that the responses in the

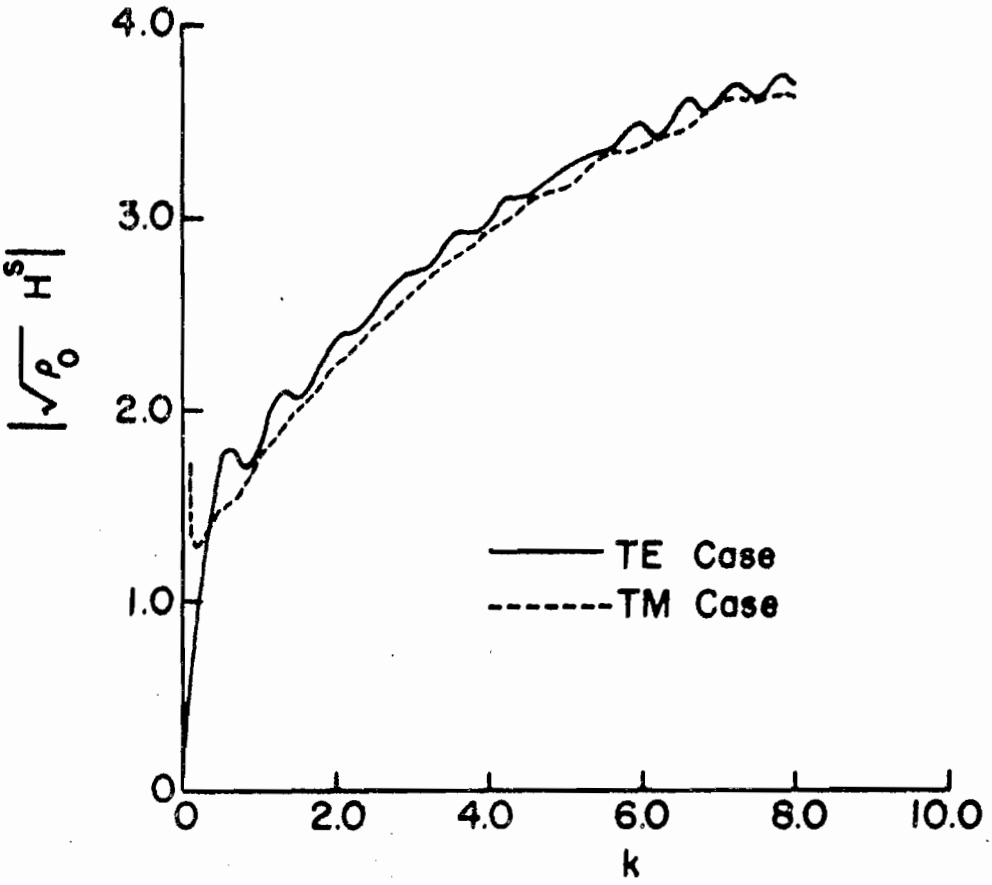

FIGURE 3.16 FREQUENCY RESPONSE IN BACKSCATTER DIRECTION OF STRIP WITH BROADSIDE INCIDENCE

TM case and the TE case differ widely near k = 0, but approach each other as k increases. This is an expected result. The TE response possesses small resonances which may be attributed to interference between the specular return and the creeping wave return. On the other hand, the TM case has no appreciable resonances since it has no significant creeping wave.

The frequency response of the strip with end-on incidence is shown in Figure 3.17 for the backscatter direction. In view of the very close similarity between the TM time domain response of the strip with end-on incidence and the circular cylinder, it is not surprising to find that the TM frequency responses of both shapes are almost identical. On the other hand, the resonances appearing in the TE responses for the two shapes are different. This is reasonable since these resonances may be attributed to an interference between the return from the front side of the body and return due to a wave traveling around the rear of the body. The creeping wave contribution for the strip appears later and with lower amplitude than for the circular cylinder. Finally, the TE and TM cases for both the strip with end-on incidence and the circular cylinder all approach the same value $(1/\sqrt{2})$ with increasing k as expected.

3.6.3 Corner Reflector

To further illustrate the application of this technique to problems for which the frequency response has not been

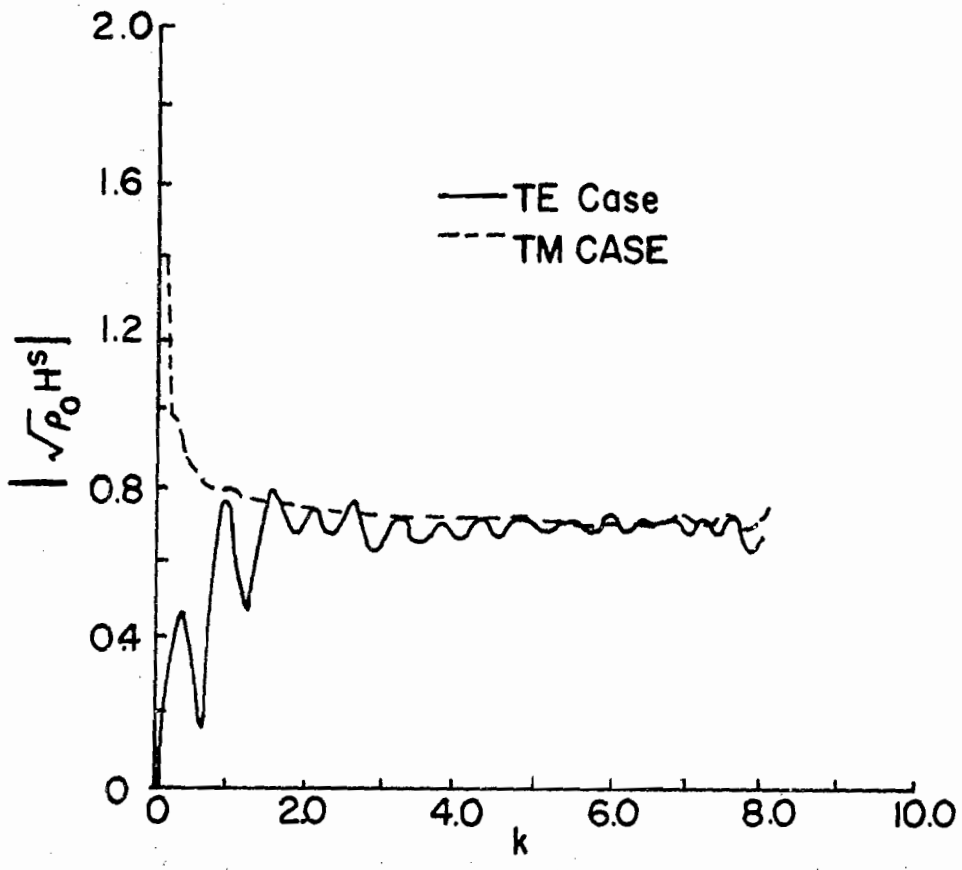

FIGURE 3.17 FREQUENCY RESPONSE IN BACKSCATTER DIRECTION OF STRIP WITH END-ON INCIDENCE

obtained by classical techniques, the corner reflector shown in Figure 3.18 was considered. This shape represents a scattering body with concave surfaces which allow multiple reflections of the incident field. The spacing between the sample points on the contour was chosen to be approximately 0.25 meters as shown in Figure 3.18. The incident field and the time increments were taken to be the same as for the case of the circular cylinder.

In Figure 3.19 is shown the approximate impulse response of the corner reflector with frontside incidence for the TE case. In the backscatter direction the first pulse is due to the specular return from the top and bottom edges. The second positive pulse and the subsequent negative swing may be interpreted as due to the double reflection by the inner sides of the corner reflector. This return approximates a differentiation of the incident pulse. Finally, the third positive, yet smaller, pulse can be considered due to the creeping wave. The scattered field at an angle of 30° from the backscatter direction is quite interesting. The first pulse, which may be interpreted as the specular return from the top edge, is followed by a second pulse which may be interpreted as the specular return from the bottom edge. The third positive pulse and its subsequent negative swing may be attributed to the inside corner. Finally, the fourth positive, yet smaller pulse may be explained by means of a creeping wave. In the forwardscatter direction the initial

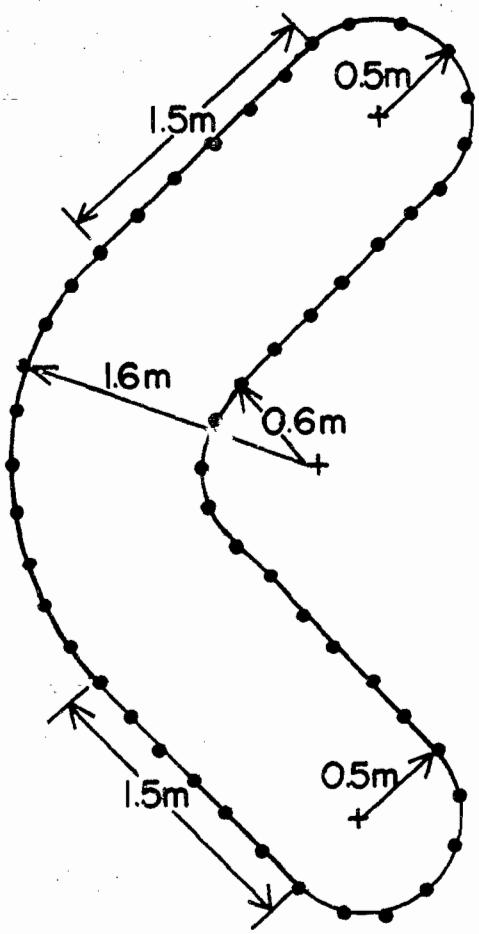

FIGURE 3.18 GEOMETRY OF CORNER REFLECTOR

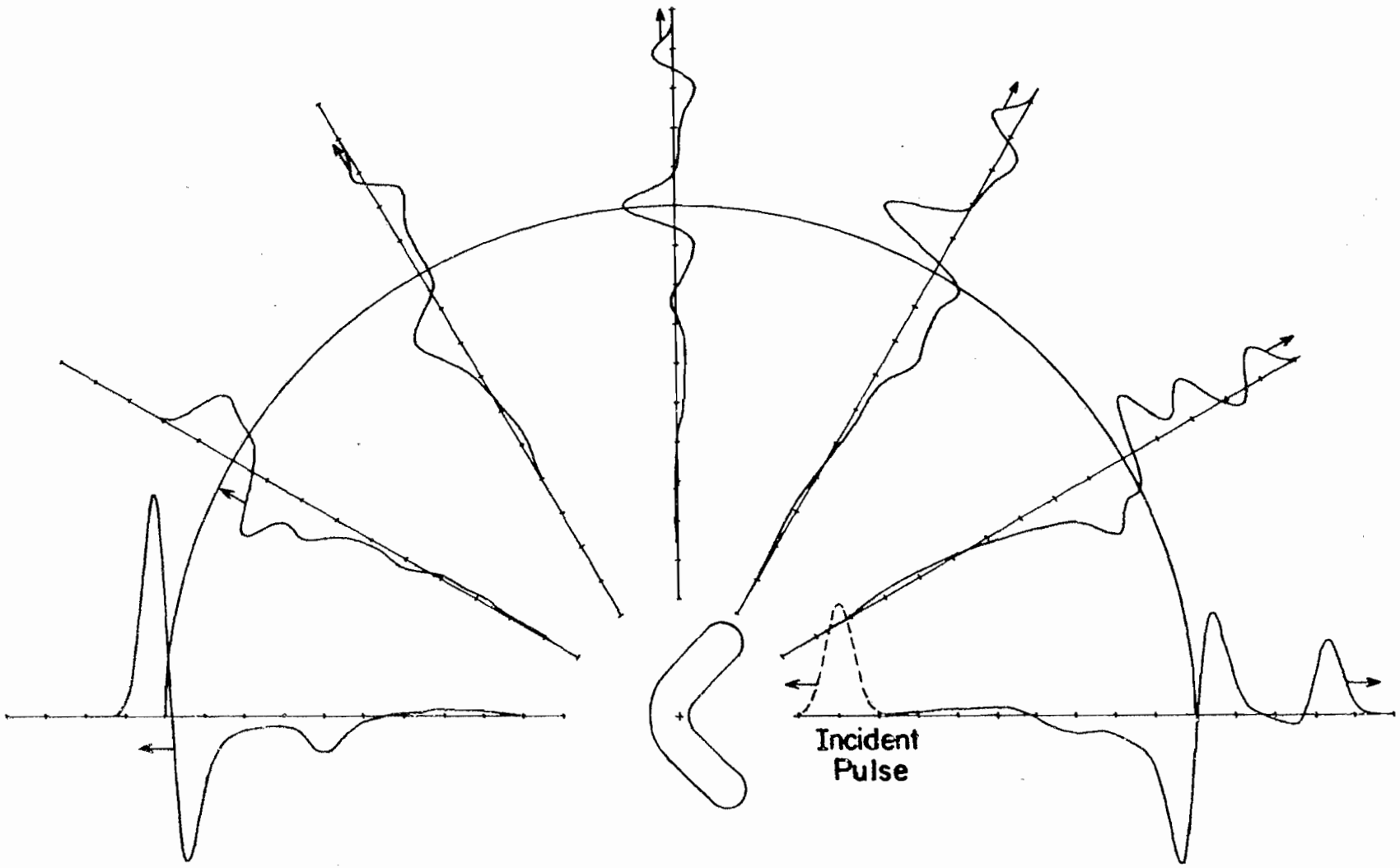

FIGURE 3.19 TE APPROXIMATE IMPULSE RESPONSE OF CORNER REFLECTOR WITH FRONTSIDE INCIDENCE

negative pulse and the positive swing that follows is similar in shape to the response of the circular cylinder and the strip in the forwardscatter direction. However, the appearance of the second positive pulse is new. This pulse may be attributed to the incident field being reflected once by the inner side of the corner and then traveling around the opposite edge to be scattered in the forward direction.

As a check on the validity of the computer program and also on the accuracy of the numerical techniques, the approximate impulse response of the corner reflector was computed with backside incidence as shown in Figure 3.20. By the time domain rec procity theorem the forward scattered field in Figure 3.19 should be the same as the forward scattered field in Figure 3.20. In this case the numerical results check out very well with the reciprocity theorem.

The approximate impulse response of the corner reflector with frontside incidence is shown in Figure 3.21 for the TM case. In the backscatter direction the first pulse is due to the specular returns from the top and bottom edges. The first negative pulse and its subsequent positive swing may be interpreted as due to the double reflection by the inner sides of the corner. Note that the sign of this contribution is opposite from the sign of the equivalent contribution in the TE case. This is because there is a change in polarity of the $\vec{H}$ field for the TM case upon

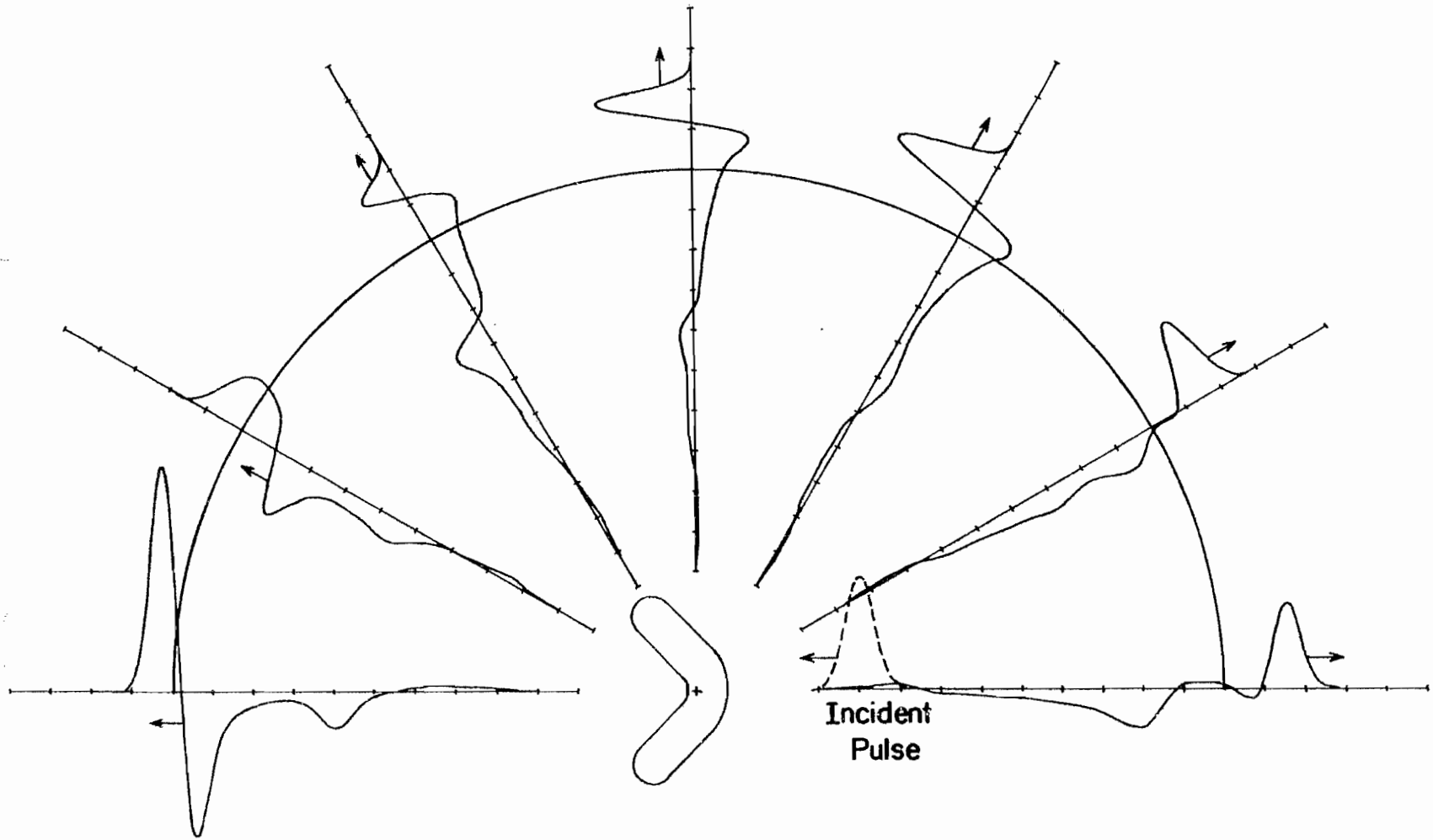

FIGURE 3.20 TE APPROXIMATE IMPULSE RESPONSE OF CORNER REFLECTOR WITH BACKSIDE INCIDENCE

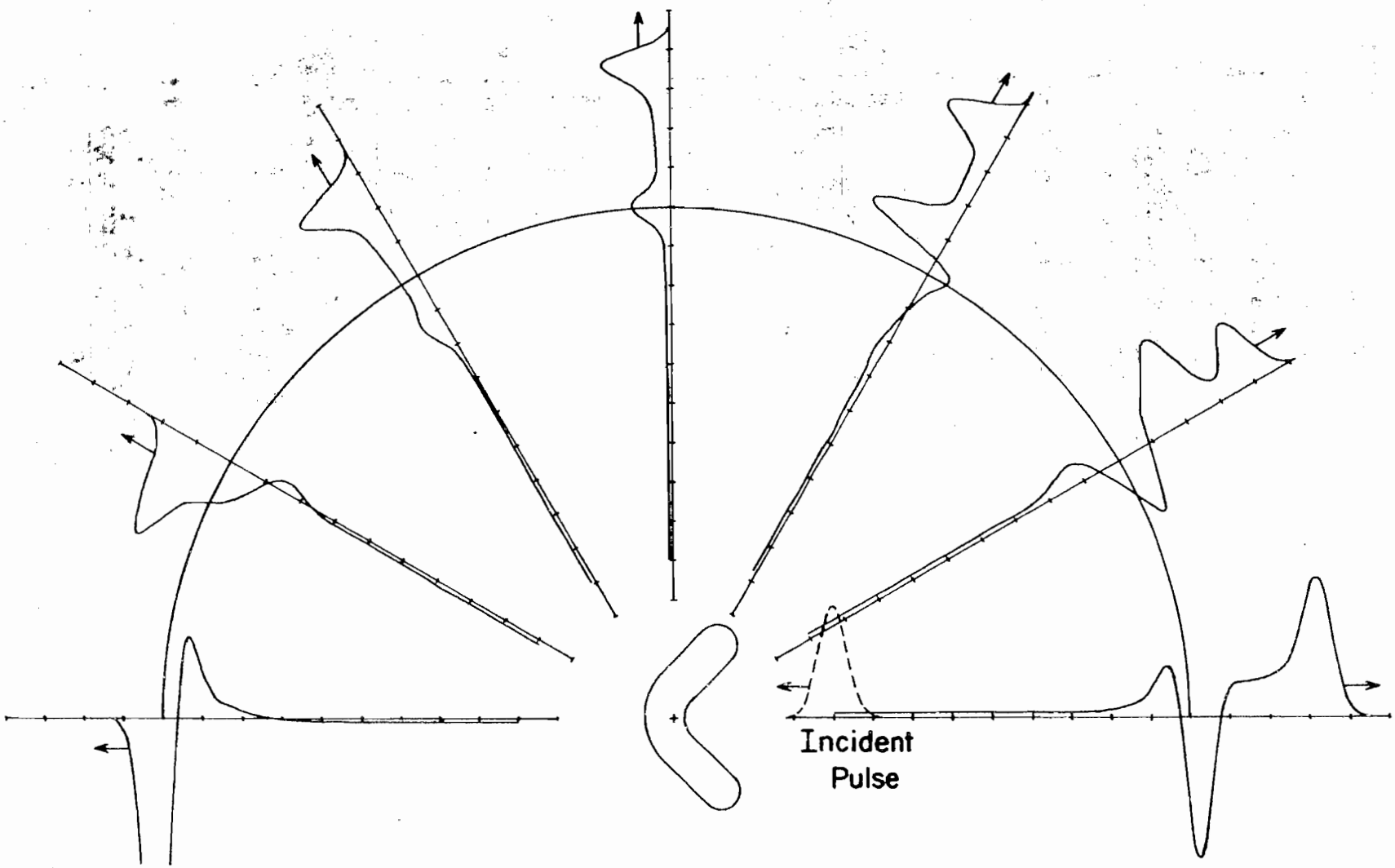

FIGURE 3.21 TM APPROXIMATE IMPULSE RESPONSE OF CORNER REFLECTOR WITH FRONTSIDE INCIDENCE

reflection from a corner, whereas, there is no change in polarity for the TE case. There is no creeping wave contribution in the TM case, as expected.

Finally, as a check on the validity of the computer program and the accuracy of the results, the approximate impulse response of the corner reflector with backside incidence was computed for the TM case. The result is shown in Figure 3.22. The numerically computed forwardscattered fields are seen to be the same for both backside incidence (Figure 3.22) and frontside incidence (Figure 3.21), as they should be by virtue of the reciprocity theorem.

In Figure 3.23 is shown the frequency response of the corner reflector in the backscatter direction with frontside incidence. Both the TE and the TM cases exhibit strong resonances. The peaks, for example, of the frequency response may be interpreted as the constructive interference of the return from the edges and the return from the inside corner. Note that the peaks of the TE case occur approximately where the nulls of the TM case occur, and vice versa. This may be explained by recalling the fact that in the time domain the returns from the inside corner have opposite signs for the TE and the TM cases. On the other hand, the returns from the edges have the same sign for the two cases. Thus, in the frequency domain the TE peaks should occur where the TM nulls occur.

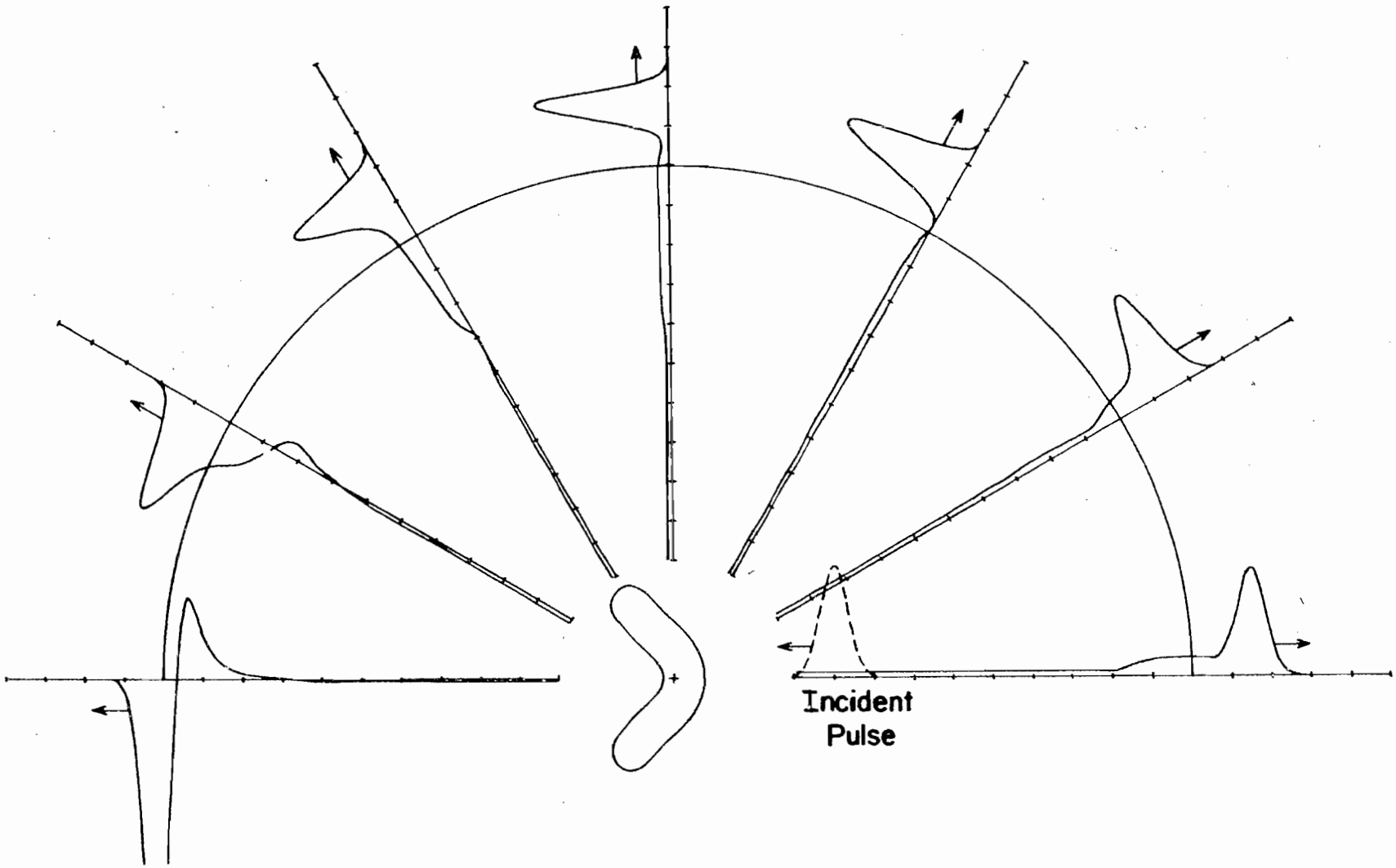

FIGURE 3.22 TM APPROXIMATE IMPULSE RESPONSE OF CORNER REFLECTOR WITH BACKSIDE INCIDENCE

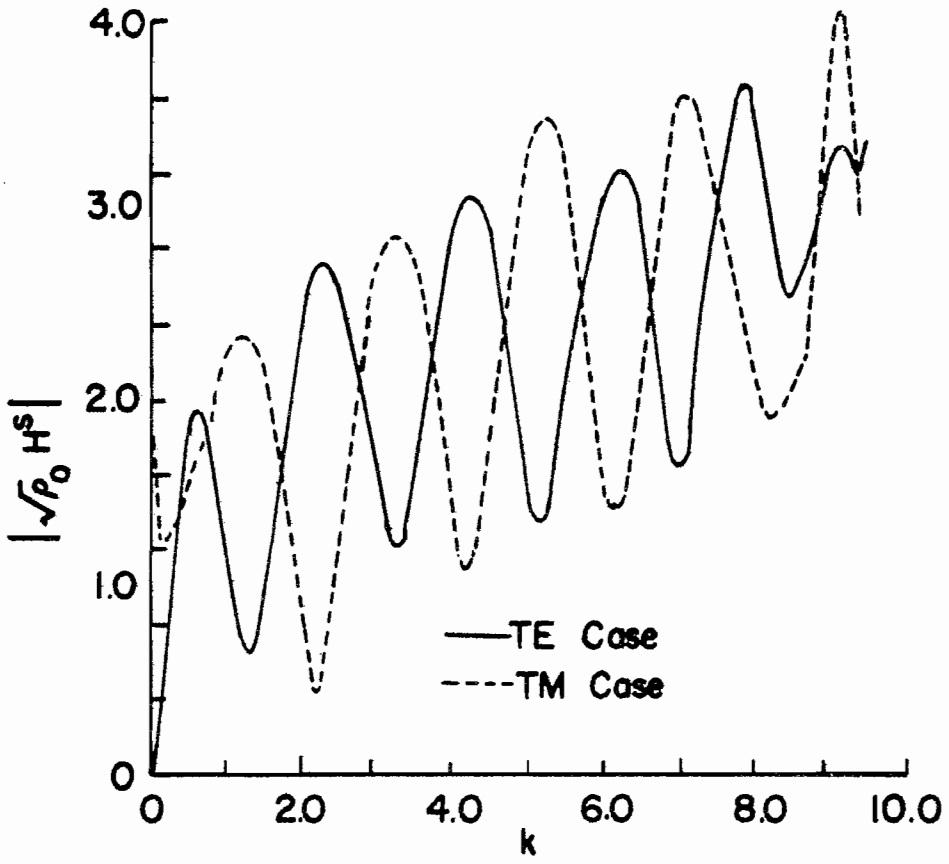

FIGURE 3.23 FREQUENCY RESPONSE IN BACKSCATTER DIRECTION OF CORNER REFLECTOR WITH FRONTSIDE INCIDENCE

The frequency response of the corner reflector in the backscatter direction with backside incidence is shown in Figure 3.24. Interference effects are present for both cases, however, they are much stronger for the TE case. The peaks in the frequency response may be interpreted as in-phase addition of the return from the nose and the return from the edge. In the time domain the effect of the edges is smaller in the TM case than in the TE case. Thus, the interference effects in the frequency domain should also be smaller for the TM case, as the numerical results illustrate.

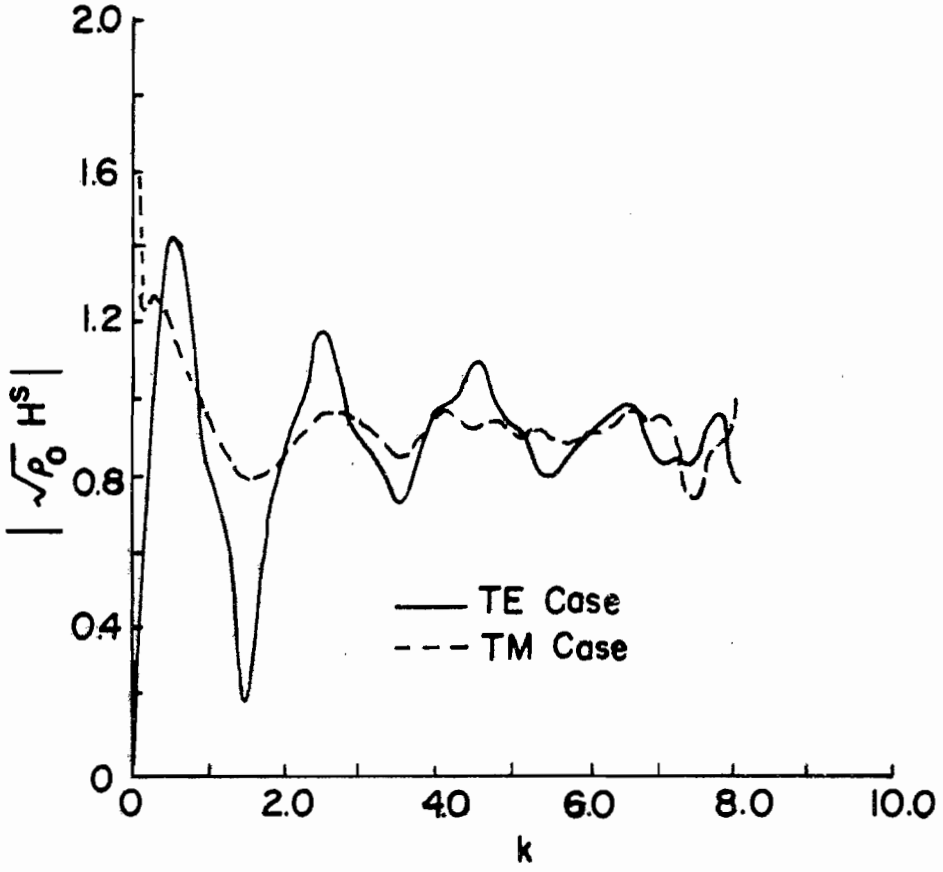

FIGURE 3.24 FREQUENCY RESPONSE IN BACKSCATTER DIRECTION OF CORNER REFLECTOR WITH BACKSIDE INCIDENCE

CHAPTER 4

NUMERICAL SOLUTION OF THREE DIMENSIONAL PROBLEMS

4.1 Preliminary Discussion

The equation (2.13) in Section 2.3 gives the current on the surface of an arbitrarily shaped three dimensional scatterer due to an arbitrary incident wave. As was the case for the cylindrical problem, it is convenient to change the units of time to light-meters. Then (2.13) becomes

$$\vec{J}(\vec{r}",t) = 2\hat{a}_1" x \vec{H}^i(\vec{r}",t)$$

$$+ \frac{1}{2\pi} \int_S \hat{a}_1" x \left[\left\{ \frac{\vec{J}(\vec{r}',\tau)}{R^2} + \frac{1}{R} \frac{\partial \vec{J}(\vec{r}',\tau)}{\partial \tau} \right\}_{\tau=t-R} x \hat{a}_R \right] dS' \,. \tag{4.1}$$

With the change of time units, equation (2.14) for the far scattered field becomes

$$\vec{H}^s(\vec{r},t) = \frac{1}{4\pi r} \int_S \left[\frac{\partial \vec{J}(\vec{r}',\tau)}{\partial \tau} \right]_{\tau=t-R} x \hat{a}_r \, dS' \,. \tag{4.2}$$

The task of this chapter is to demonstrate that numerical solution of (4.1) and (4.2) is feasible and also gives good

results.

To handle arbitrarily shaped geometries completely, it is convenient to expand (4.1) in the rectangular coordinate system. Doing this gives the components of $\vec{J}$ as:

$$J_x(\vec{r}'',t) = 2(n_y H_z^i - n_z H_y^i) + \frac{1}{2\pi}\int_S \{(\frac{J_x}{R^2} + \frac{1}{R}\frac{\partial J_x}{\partial \tau})(n_y n_{Ry} + n_z n_{Rz}) - (\frac{J_y}{R^2} + \frac{1}{R}\frac{\partial J_y}{\partial \tau}) n_y n_{Rx} - (\frac{J_z}{R^2} + \frac{1}{R}\frac{\partial J_z}{\partial \tau}) n_z n_{Rx}\}_{\tau=t-R} dS' \quad (4.3a)$$

$$J_y(\vec{r}'',t) = 2(n_z H_x^i - n_x H_z^i) + \frac{1}{2\pi}\int_S \{(\frac{J_y}{R^2} + \frac{1}{R}\frac{\partial J_y}{\partial \tau})(n_z n_{Rz} + n_x n_{Rx}) - (\frac{J_z}{R^2} + \frac{1}{R}\frac{\partial J_z}{\partial \tau}) n_z n_{Ry} - (\frac{J_x}{R^2} + \frac{1}{R}\frac{\partial J_x}{\partial \tau}) n_x n_{Ry}\}_{\tau=t-R} dS' \quad (4.3b)$$

$$J_z(\vec{r}'',t) = 2(n_x H_y^i - n_y H_x^i) + \frac{1}{2\pi}\int_S \{(\frac{J_z}{R^2} + \frac{1}{R}\frac{\partial J_z}{\partial \tau})(n_x n_{Rx} - n_y n_{Ry}) - (\frac{J_x}{R^2} + \frac{1}{R}\frac{\partial J_x}{\partial \tau}) n_x n_{Rz} - (\frac{J_y}{R^2} + \frac{1}{R}\frac{\partial J_y}{\partial \tau}) n_y n_{Rz}\}_{\tau=t-R} dS' \quad (4.3c)$$

where

$$\vec{J} = J_x\hat{a}_x + J_y\hat{a}_y + J_z\hat{a}_z$$

$$\hat{a}_i'' = n_x\hat{a}_x + n_y\hat{a}_y + n_z\hat{a}_z$$

$$\hat{a}_R = n_{Rx}\hat{a}_x + n_{Ry}\hat{a}_y + n_{Rz}\hat{a}_z \ .$$

The coupled integro-differential equations in (4.3) give the solution of the current on the surface of the scatterer. However, by virtue of the fact that the current is constrained to flow on the surface only two of these equations are independent. Hence, only two of the components of $\vec{J}$ need to be found from (4.3). The remaining component of $\vec{J}$ is given by

$$n_x J_x + n_y J_y + n_z J_z = 0 \ , \qquad (4.4)$$

where n_x, n_y, and n_z are the rectangular components of the unit normal at the observer.

To find the far field from the current density for arbitrarily shaped geometries it is convenient to expand (4.2) in rectangular coordinates. Carrying out this operation on (4.2) yields

$$H_x^s = \frac{1}{4\pi r}\int_S \left(\frac{\partial J_x}{\partial \tau} n_{rz} - \frac{\partial J_z}{\partial \tau} n_{ry}\right)_{\tau=t-R} dS' \qquad (4.5a)$$

$$H_y^s = \frac{1}{4\pi r}\int_S \left(\frac{\partial J_z}{\partial \tau} n_{rx} - \frac{\partial J_x}{\partial \tau} n_{rz}\right)_{\tau=t-R} dS' \qquad (4.5b)$$

$$H_z^s = \frac{1}{4\pi r} \int_S \left(\frac{\partial J_x}{\partial \tau} n_{ry} - \frac{\partial J_y}{\partial \tau} n_{rx} \right)_{\tau=t-R} dS' \qquad (4.5c)$$

where

$$\vec{H}^s = H_x^s \hat{a}_x + H_y^s \hat{a}_y + H_z^s \hat{a}_z$$

$$\hat{a}_r = n_{rx} \hat{a}_x + n_{ry} \hat{a}_y + n_{rz} \hat{a}_z \ .$$

4.2 Numerical Approximation of Integro-Differential Equation

The equations for the current on the surface of a three dimensional scatterer given in (4.3) and (4.4) are somewhat more complicated to solve numerically than the analogous equations for cylindrical scatterers in several respects. First, the argument of the integral must be evaluated at arbitrary points in time rather than at only the time sample points. Second, a set of three coupled equations must be solved rather than only two decoupled equations. Finally, many more sample points must be used to describe a surface than a contour with the same linear dimension.

On the other hand, the cylindrical equations possess a time integration that is not present in the three dimensional formulation. The explanation for this is that in the cylindrical case the space integration over z has been replaced by a time integration over t. It should be noted that cylindrical problems may also be solved by the three dimensional formulation discussed in this Chapter.

It is convenient to view the space integration in (4.3) and (4.5) as an integration over the variables ϕ and θ in a spherical coordinate system. The integration over ϕ is essentially the integration of a periodic function over one period. Thus, conclusions similar to those reached for the space integration in the cylindrical case apply here for the ϕ-integration. They are principally: (1) the rectangular approximation for the ϕ-integration gives good results, and (2) the error incurred using the rectangular approximation for the ϕ-integration is essentially the N_ϕ^{th} Fourier coefficient of the ϕ-integration argument where N_ϕ is the number of sample points at a given value of θ. Thus, the rectangular rule was sed for the ϕ-integration.

The θ-integration can be viewed as the integration over a half period of a periodic function that is symmetric about its mid-point. So the rectangular approximation for the θ-integration gives good results and produces an error that is essentially the $2N_\theta^{th}$ Fourier coefficient of the θ integration argument where N_θ is the number of θ sample points. Hence, the rectangular rule was also used for the θ-integration.

Since the rectangular rule was used for both the ϕ-integration and the θ-integration, then the numerical approximation of the space integration that was used may be viewed in the following manner. The surface of the scatterer was broken into a number of patches. The contribution of each

of these patches to the surface integral in (4.3) was then approximated as the value of the argument of the integral at some point in the patch times the area of the patch.

The technique used for the numerical time differentiation was the same as that used in the cylindrical case. The current was approximated by a fourth order polynominal. The numerical approximation for the time derivatives of the current was obtained by analytically differentiating this polynominal approximation. In order to achieve the best accuracy, the five points used for the polynominal approximation of the current were chosen such that the derivative would be evaluated as near as possible to the middle of them.

4.3 Numerical Solution

The numerical solution of (4.3) and (4.4) was accomplished by first breaking the scatterer surface into patches and choosing a time increment. Next, the current at each of these patches was computed numerically using (4.3) and (4.4). The computation was carried out sequentially in time with the starting point in time being when the incident field arrived at the scatterer. This process of marching on in time is possible since (4.3) gives the current at a point in space-time in terms of (a) the incident field at the same point in space-time (which is known) and (b) currents at other points in space but at earlier times (which either are zero or have been previously calculated).

Finally, (4.5) in conjunction with the numerically computed surface currents was used to calculate the far scattered fields.

The criteria for the choice of sample points in space-time for the three dimensional case are quite similar to the criteria for the cylindrical case. The first restriction is that

$$\Delta t < R_{min}$$

where

Δt = time increment

R_{min} = minimum distance between space sample points.

This restriction says that the time increment must be less than the time it takes a wave, moving at the speed of light, to travel between the closest space sample points.

As in the cylindrical case, the sample points in space were chosen so that a good representation of the time derivative of the incident field would be obtained. In addition, the sample points in ϕ at each level of θ were equally spaced. The sample points in θ were chosen such that the distances between adjacent levels in θ were approximately the same.

The largest error in the numerical solution occurs initially in time on the unilluminated side of the scatterer where the incident H field is tangent to the surface. In this region of space-time there is in the numerical process

a subtraction of two numbers which are large compared with their difference. In the cylindrical case it was necessary to use a fine time increment during this critical period of time in order to obtain good results. However, for the three dimensional cases considered it was found that good accuracy could be obtained without resorting to a fine time increment. An explanation for this is that the relative size of the critical region in space-time was significantly smaller for the three dimensional scatterers considered than for the cylindrical scatterers considered. Thus, the relative size of the contribution to the scattered field from the critical region in space-time would also be significantly smaller for the three dimensional cases.

4.4 Numerical Examples

4.4.1 Sphere with 1.0 Meter Radius

The feasibility of actual numerical solution of the integro-differential equation for three dimensional problems was first demonstrated by considering the case of a sphere centered at the origin. The sphere was chosen as the test case because the results could be checked by using the classical frequency response of a sphere. Moreover, the choice of sample points on the surface of a sphere was relatively straightforward.

The actual sphere used for the test case had a radius of 1.0 meter and the incident field was the approximate

plane impulse

$$\vec{H}^i(\vec{r},t) = -\hat{a}_y \frac{2}{\sqrt{\pi}} e^{-4(z+t)^2} \qquad (4.6)$$

which possessed a width approximately equal to the diameter of the sphere. Thus, the incident field was a plane wave polarized in the x-direction and propagating in the negative z-direction as shown in Figure 4.1. It should be noted that numerical solution of the integro-differential equation is also possible for other incident fields such as a spherical wave. The sample points in ϕ at a given level of θ were equally spaced such that the spacing was approximately 0.25 meters. The sample points in θ were spaced every 15° starting at $\theta = 7.5°$. Finally, the time increment was chosen to be 0.2 light-meters.

The current on the scatterer was found by solving (4.3) and (4.4) with the numerical procedure described in Section 4.3. This current, in turn, was used to numerically compute the far scattered field with (4.5). This far scattered field may be interpreted as the approximate impulse response of the sphere. During the numerical computations the symmetry possessed by this problem was exploited and a significant saving in both computer time and computer memory resulted.

The far field is shown in Figure 4.2 for the backscatter direction. Also shown is the result obtained by performing the inverse Fourier transform of the classical frequency

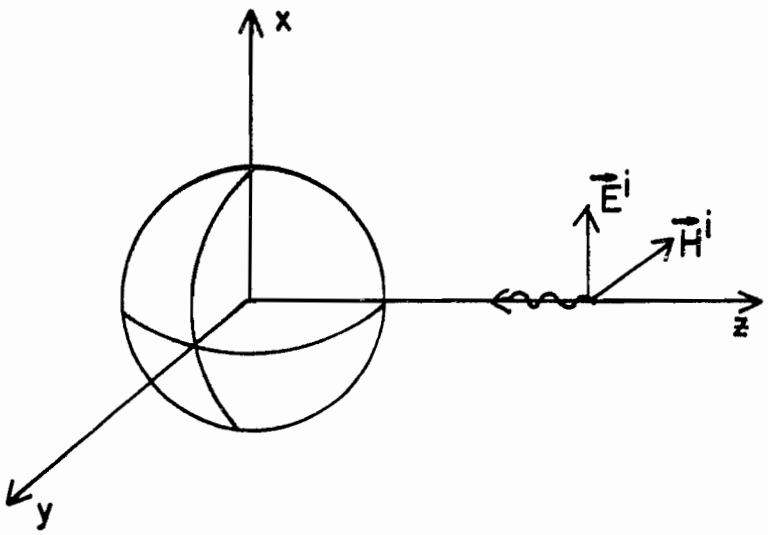

FIGURE 4.1 GEOMETRY OF THREE DIMENSIONAL SCATTERING PROBLEM

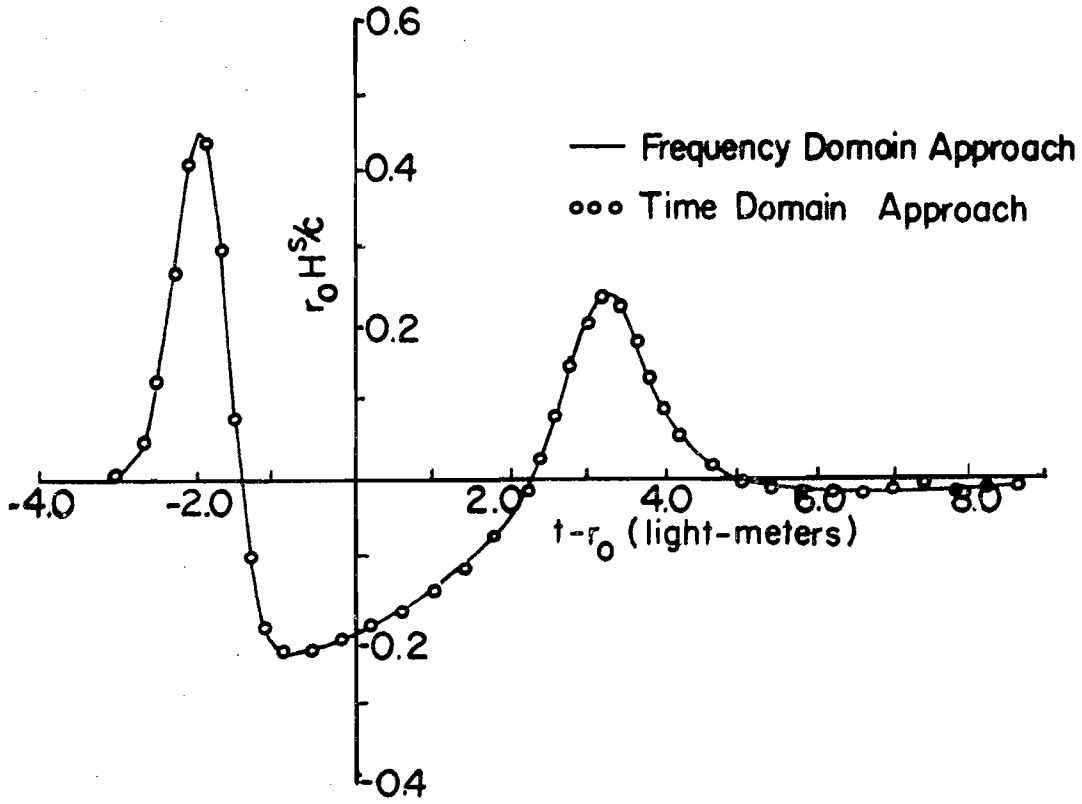

FIGURE 4.2 APPROXIMATE IMPULSE RESPONSE OF SPHERE BACKSCATTER DIRECTION

response using the technique described in Section 3.5. As can be seen in Figure 4.2 the two results compare well in the backscatter direction. The comparison of the far scattered fields obtained by these two techniques was also good for other directions.

The initial peak in Figure 4.2 corresponds to the specular reflection from the sphere and would be predicted by geometric optics. The negative swing that follows is similar to what would be given by the physical optics approximation. And finally, the second positive pulse may be interpreted as due to a wave traveling around the backside of the sphere.

The E-plane approximate electromagnetic impulse response (i.e., the y component of the $\vec{H}^s$ field in the x-z plane) of the 1.0 meter sphere is shown in Figure 4.3. The H-plane approximate impulse response (i.e., the θ component of the $\vec{H}^s$ field in the y-z plane) is shown in Figure 4.4. As in the cylindrical case this figure may be viewed as a "snapshot" of the waveforms in space, with all dimensions to scale, except the distance to the sphere. The outer semicircle represents the points in space that the peak of the incident pulse would have reached if it were reflected from the origin (the center of the sphere in this case). The amplitude of the scattered H field is normalized by the multiplying factor r_o, where r_o is the distance of the outer semicircle from the origin. The initial positive pulses of the waveforms

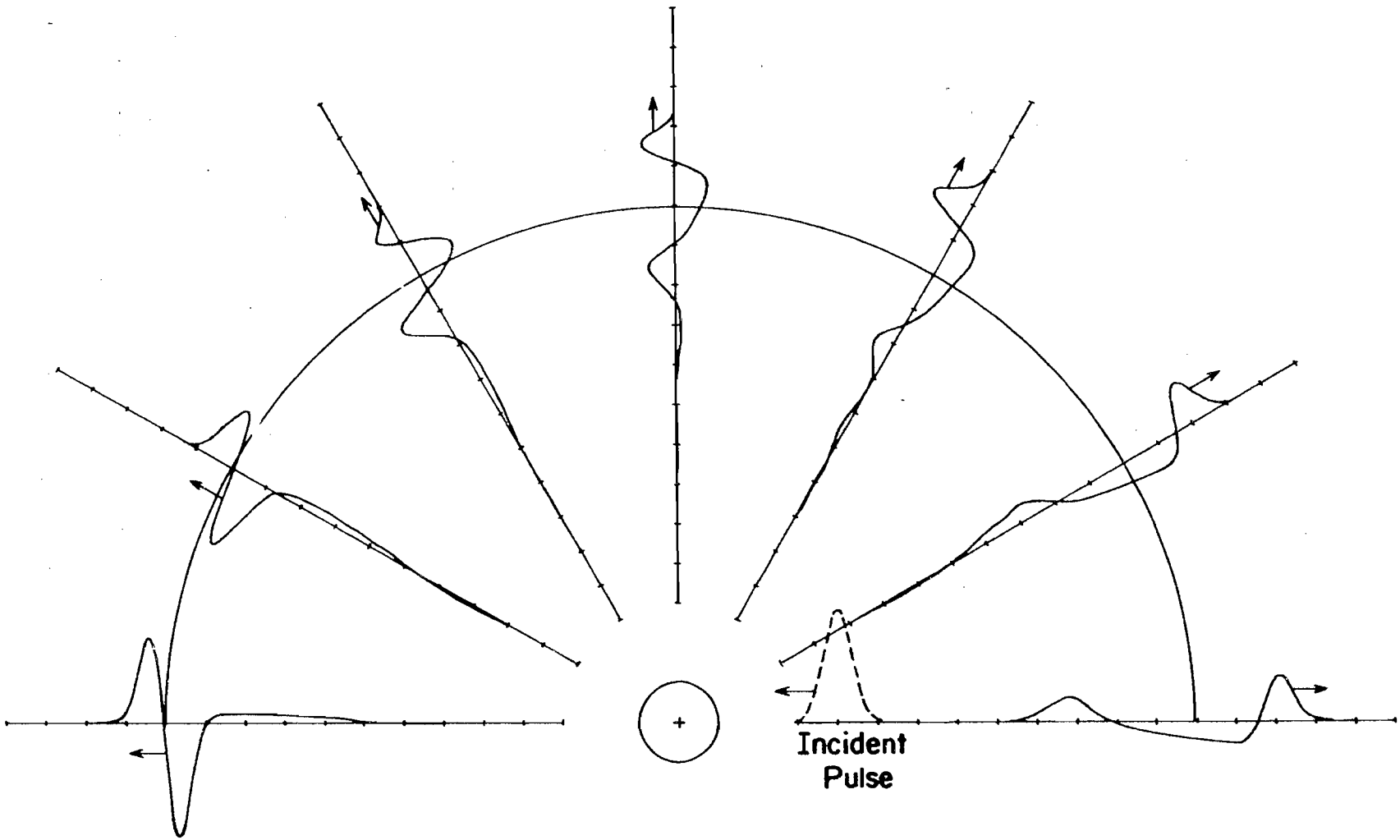

FIGURE 4.3 APPROXIMATE IMPULSE RESPONSE OF SPHERE IN E—PLANE

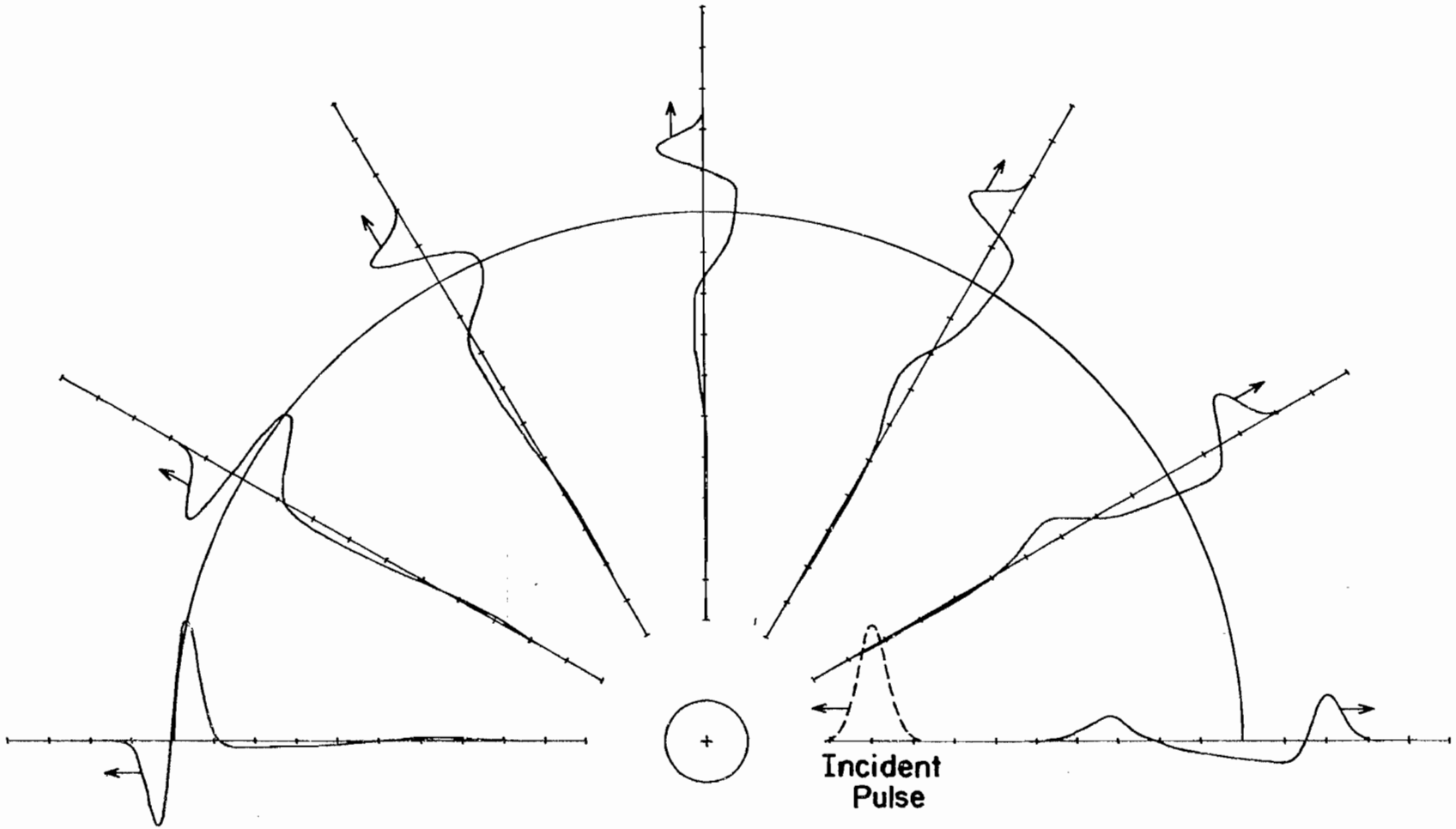

FIGURE 4.4 APPROXIMATE IMPULSE RESPONSE OF SPHERE IN H—PLANE

in the various directions may be interpreted as the contribution due to specular reflection and would be predicted by geometric optics. The subsequent positive pulse may be interpreted as due to waves traveling around the scatterer. As in the cylindrical case, these waves are often called creeping waves. It is interesting to note that at an angle of 90° the contribution due to the creeping wave appears earlier and is stronger in the E-plane than in the H-plane.

Finally, using the technique discussed in Section 3.5, the frequency response of the 1.0 meter sphere was computed from the approximate impulse response. The frequency response is plotted as a function of k where k is defined to be ω/c and ω is the radian frequency. In Figure 4.5 the result in the backscatter direction is compared with the classical frequency response. The comparison is good up to approximately $k = 6$.

In general, the results obtained for the sphere were not quite as good as the results obtained for the circular cylinder. However, this is not surprising since the numerical techniques used for the three dimensional case were less refined than those used for the cylindrical case.

4.4.2 Sphere with 0.5 Meter Radius

The sphere with a 0.5 meter radius was the second shape considered. This sphere was chosen because it permits a further check on the validity of the computer program.

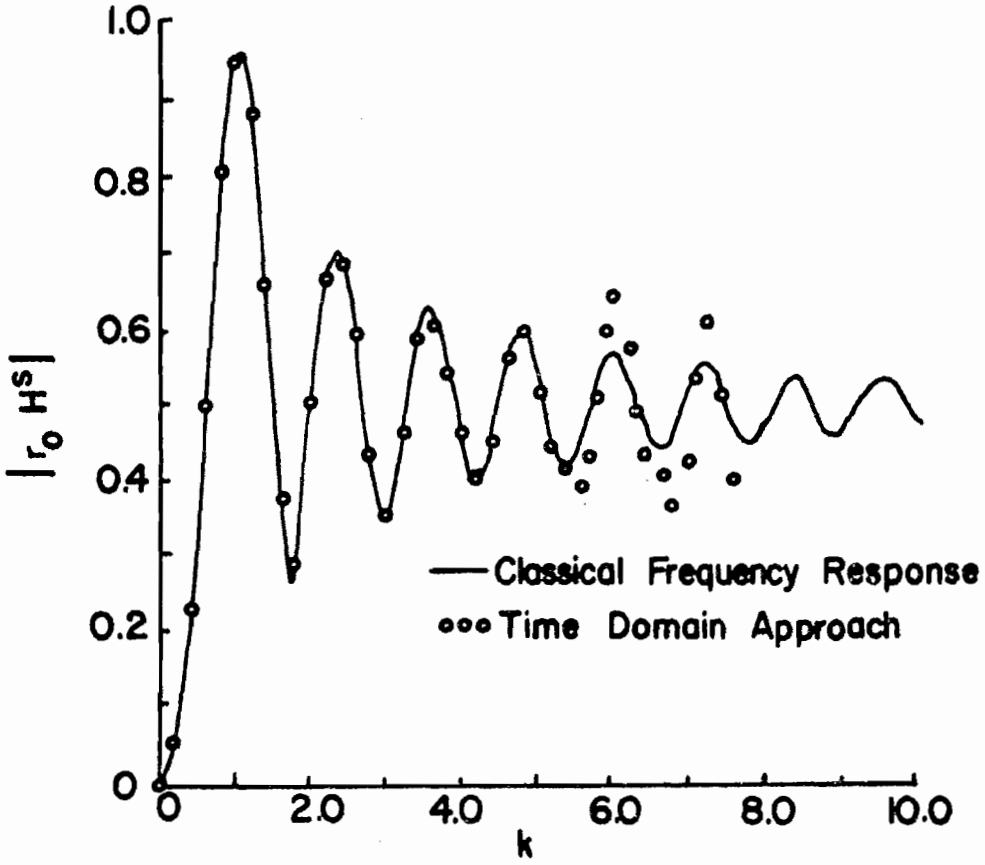

FIGURE 4.5 FREQUENCY RESPONSE IN BACKSCATTER DIRECTION OF SPHERE WITH ONE METER RADIUS

In addition, the response of the 0.5 meter sphere may be easily compared to the response of the cylinder with hemispherical caps which is considered in Section 4.4.3.

The incident $\vec{H}$ field was taken to be the same approximate impulse as was used for the 1.0 meter sphere, and thus, possessed a width approximately equal to twice the diameter of the 0.5 meter sphere. The sample points on the surface were chosen in the same manner as for the case of the 1.0 meter sphere. And finally, the time increment was taken to be 0.2 light-meters.

The approximate impulse response of the 0.5 meter sphere in the E-plane is shown in Figure 4.6 and the response in the H-plane is shown in Figure 4.7. It is noted that the relative size of the creeping wave contribution with respect to the specular contribution is larger for the 0.5 meter sphere than for the 1.0 meter sphere. Moreover, the approximate impulse response in the backscatter direction begins to look similar to the second derivative of the incident pulse, which would be predicted by the Rayleigh approximation.

4.4.3 Cylinder with Hemispherical Caps

The final shape considered was a cylinder of radius 0.5 meters and length 2.0 meters with hemispherical end caps. The axis of the cylinder was the z-axis. This shape was chosen to demonstrate the numerical solution of a problem directly in the time domain that has not been solved by classical techniques in the frequency domain. This shape

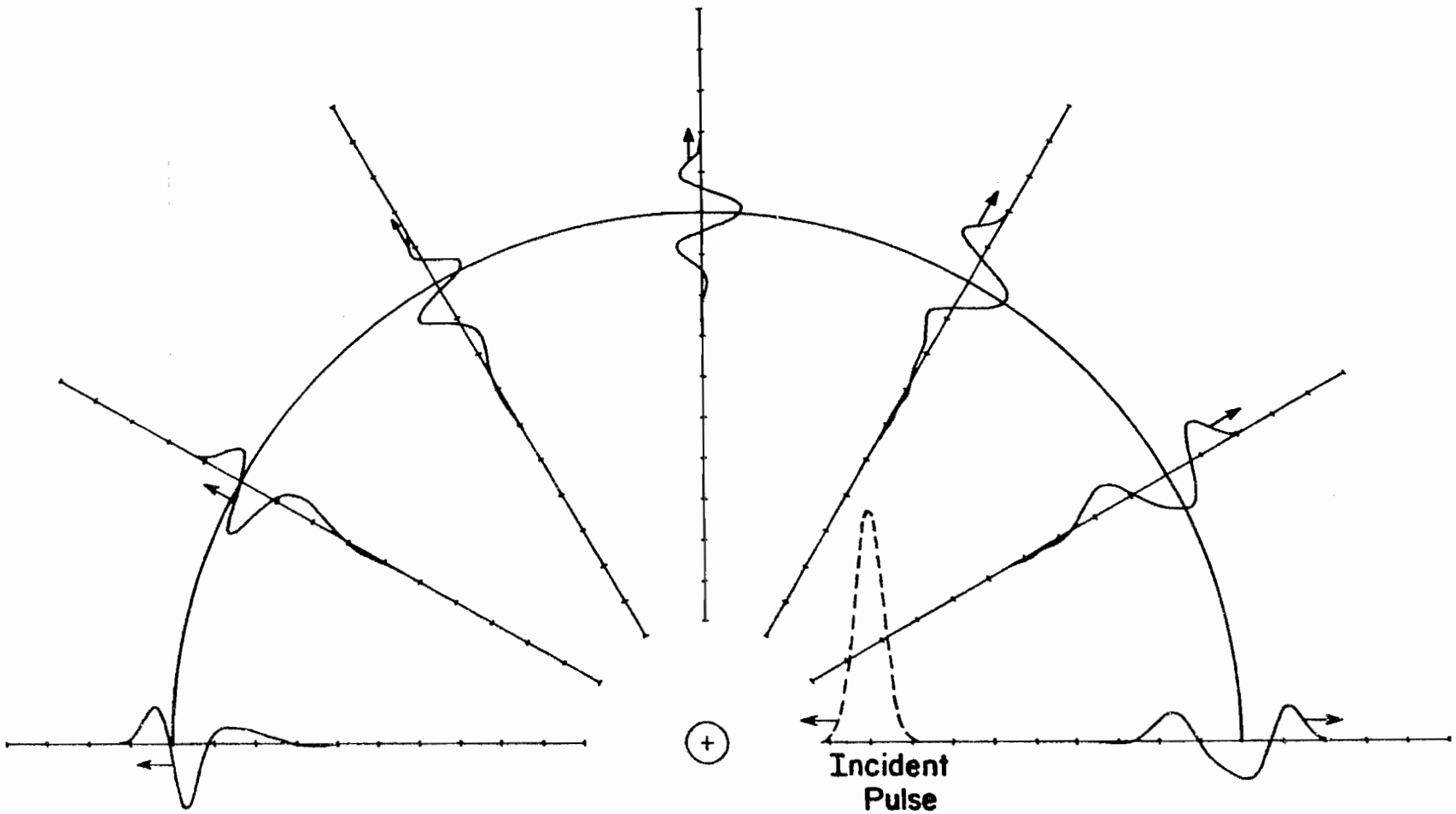

FIGURE 4.6 APPROXIMATE IMPULSE RESPONSE OF SPHERE IN E— PLANE

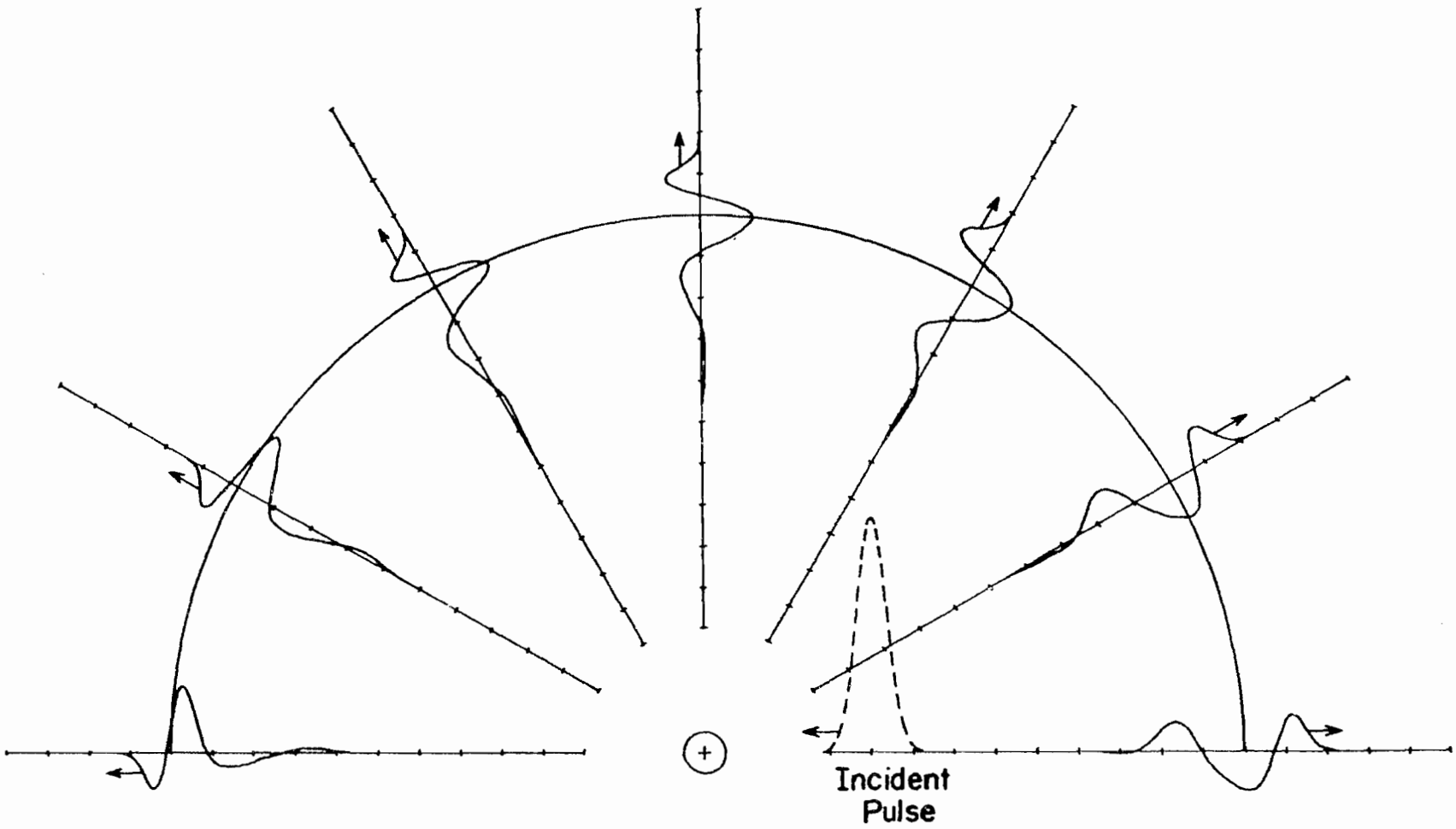

FIGURE 4.7 APPROXIMATE IMPULSE RESPONSE OF SPHERE IN H-PLANE

may be thought of as a 0.5 meter sphere that has been bisected and pulled apart. Thus, the finite cylinder with hemispherical caps is a natural extension of the sphere geometry.

The incident $\vec{H}$ field was taken to be the same as used for both the 1.0 meter sphere and the 0.5 meter sphere. The sample points on the hemispherical caps were chosen to be the same as those on the 0.5 meter sphere in Section 4.4.2. On the cylinder itself the sample points were equally spaced every 30° in ϕ and every 0.25 meters in z. The time increment was taken to be 0.2 light meters as before. Finally, in the interest of economy only axial incidence was considered.

The E-plane approximate impulse response of the finite cylinder is shown in Figure 4.8 and the H-plane response is shown in Figure 4.9. As before, the initial positive pulses may be interpreted as the contribution due to specular reflection and would be predicted by geometric optics. Moreover, the numerical results show that the initial part of the responses of the finite cylinder are the same as the initial part of the responses of the 0.5 meter sphere, as they should be. Subsequently, in the backscatter and near backscatter directions the response becomes very small, indicating that in these directions there is very little return from the sides of the cylinder. The following negative swing may be interpreted as the return from the junction of the

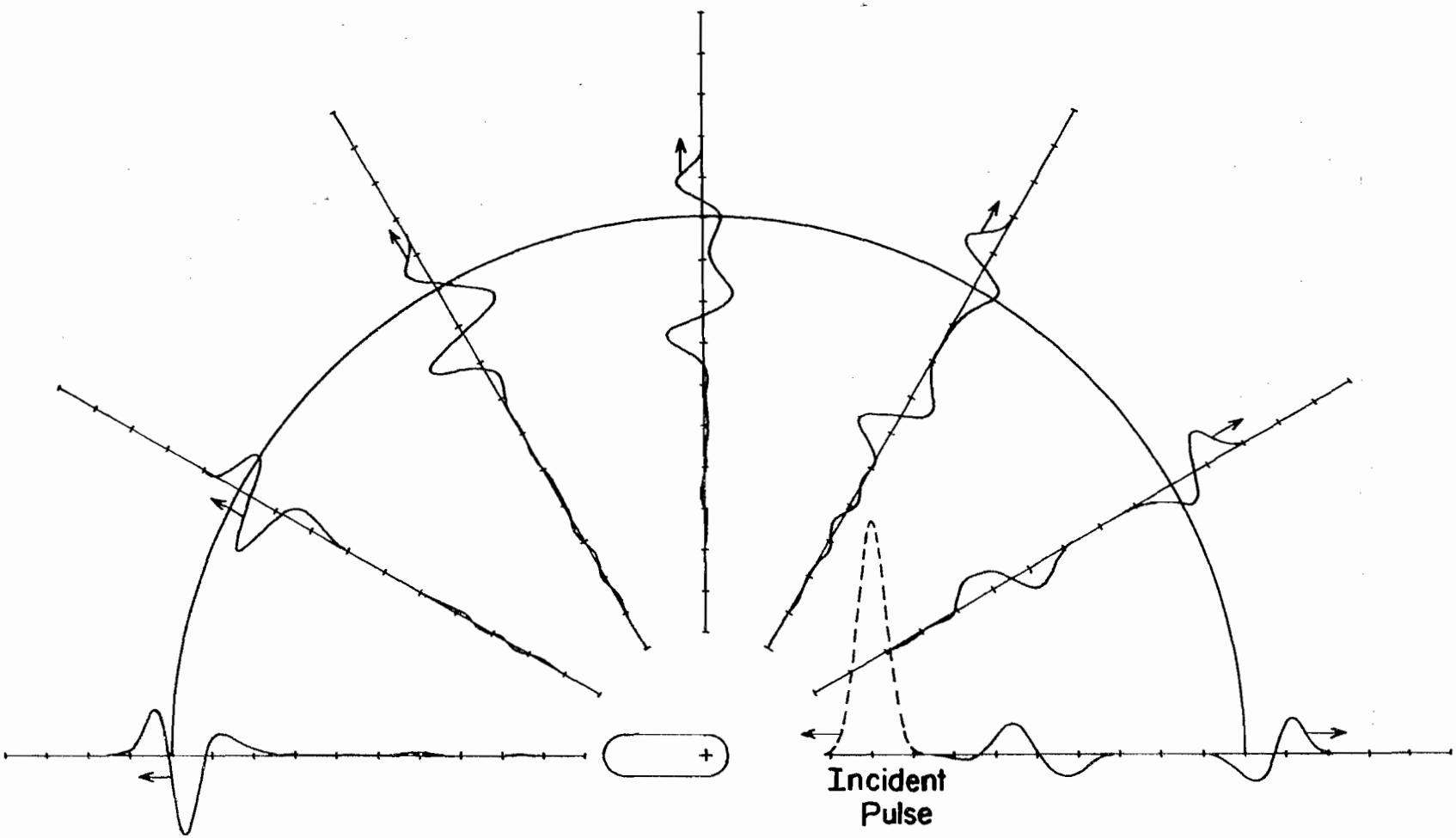

FIGURE 4.8 APPROXIMATE IMPULSE RESPONSE OF FINITE CYLINDER WITH AXIAL INCIDENCE IN E—PLANE

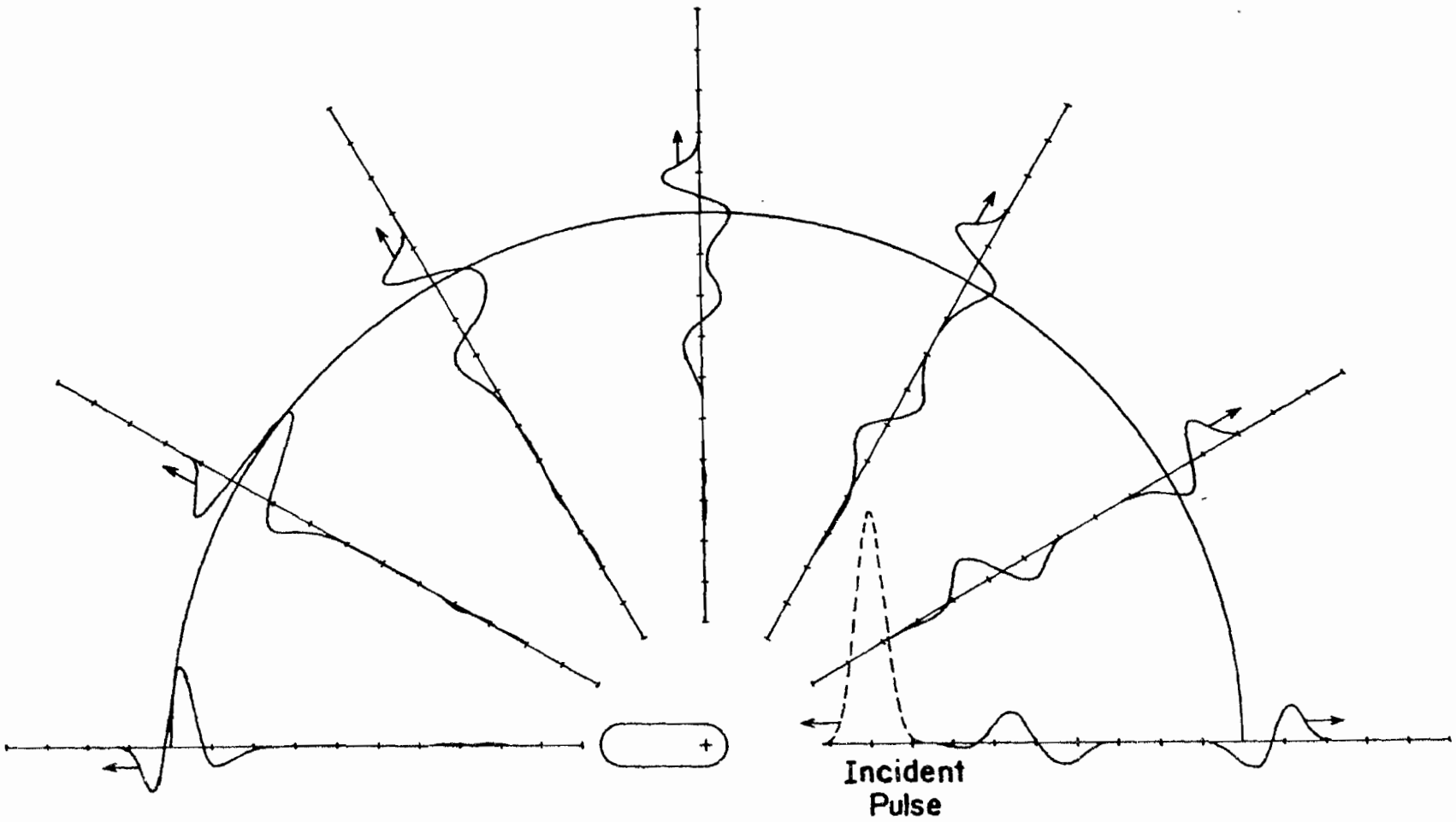

FIGURE 49 APPROXIMATE IMPULSE RESPONSE OF FINITE CYLINDER WITH AXIAL INCIDENCE IN H—PLANE

cylinder and the backside hemispherical cap. Finally, the second positive pulse may be attributed to a wave traveling around the rear of the cylinder.

In Figure 4.10 the frequency response in the backscatter direction is shown for the finite cylinder with axial incidence. This frequency response contains strong resonances at the lower frequencies which may be interpreted as due to interference between the return from the nose of the cylinder and the return from the rear of the cylinder. As the frequency increases these resonances appear to diminish and approach a value of 0.25 which is the result predicted by geometric optics. The accuracy of the frequency response diminishes r.pidly beyond k = 6, which corresponds to the frequency when the spacing between sample points is approximately a quarter wavelength.

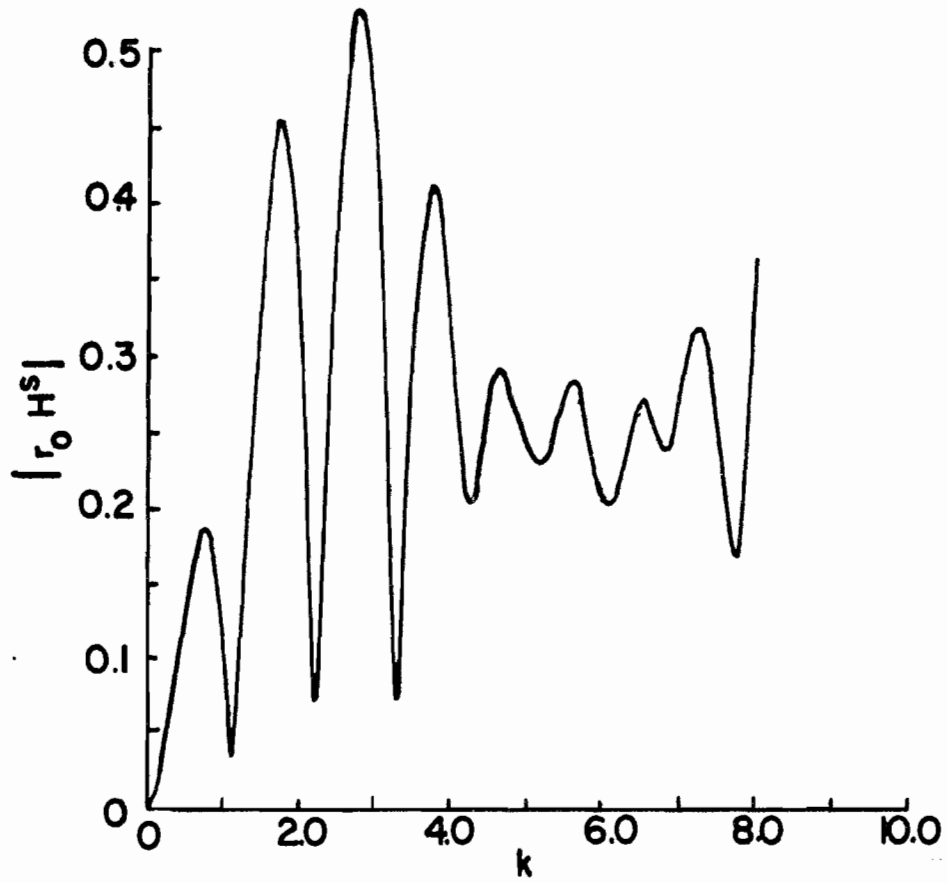

FIGURE 4.10 FREQUENCY RESPONSE IN BACKSCATTER DIRECTION OF FINITE CYLINDER WITH AXIAL INCIDENCE

CHAPTER 5

DISCUSSION

5.1 Summary and Conclusions

In this thesis integro-differential equations for solving time domain electromagnetic scattering problems have been derived. In addition it has been demonstrated that numerical solution of these equations is feasible and gives good results. In Chapter 2 time domain integro-differential equations are derived for (1) the magnetic field intensity on the surface of a conducting cylindrical scatterer with arbitrary cross section and (2) the current density on the surface of a conducting three dimensional scatterer with arbitrary shape. These equations give the magnetic field intensity (current density) at a point in space-time in terms of the incident field at that point in space-time and also in terms of the magnetic field intensity (current density) at other points in space but at earlier points in time. An important feature of these formulations is that the incident wave need not be plane.

The feasibility and accuracy of numerical solution of the cylindrical formulation is demonstrated in Chapter 3 by considering the case of a circular cylinder with a normally incident approximate plane impulse. The resulting far

scattered field is the approximate electromagnetic impulse response of the circular cylinder. To illustrate the generality of this technique the approximate impulse response of both a strip and a corner reflector were obtained. In the resulting approximate impulse responses the contributions due to different scattering mechanisms can be easily discerned. The specular reflection appears as a positive pulse with the appropriate time delay near the beginning of the response. The double reflection by the corner reflector is also clearly evident. Finally, the contribution due to a wave traveling around the rear of the scatterer can be clearly distinguished. The approximate impulse responses also graphically illustrate some striking differences between the TE and the TM cases. For example, the response in the TM case has a very long tail and also possesses no creeping wave contribution, whereas, the response in the TE case dies out more quickly and does possess a significant creeping wave contribution. As an additional check on the validity of the computer program and the numerical techniques, it was demonstrated that the numerical results are consistent with the time domain reciprocity theorem. Finally, the frequency response was computed from the approximate impulse response in order to further illustrate the usefulness of the impulse response concept in electromagnetic scattering problems.

In Chapter 4 the feasibility and accuracy of numerical solution of the three dimensional formulation is demonstrated by considering the case of a sphere with an incident approximate plane impulse. To further illustrate the use of this technique the approximate impulse response of a finite cylinder with axial incidence was calculated. As in the cylindrical formulation, the portions of the approximate impulse response due to the different scattering mechanisms can be clearly distinguished. One interesting result is that the sides of the finite cylinder do not appear to radiate in the backscatter and near backscatter directions for the case of axial incidence. Another result for the bodies considered is that the creeping wave effect arrives earlier and is larger for the scattered field in the E-plane than for the scattered field in the H-plane. The frequency response was calculated from the approximate impulse response as in the cylindrical formulation.

The ultimate limitations on this technique are the computer memory size and the required computer time. The time increment must be less than the time it takes a wave, traveling at the speed of light, to travel between the closest points in space. Moreover, the distance between adjacent space points should be less than a quarter wavelength of the "highest" frequency contained in the incident wave. And finally, there must be an adequate number of space sample points to give a "good" representation of the

scatterer. Thus, if the scatterer size and complexity is increased, then the number of sample points in space-time must also be increased. Likewise, if the length of the incident approximate impulse is decreased, then the number of sample points in space-time again must be increased. This, in turn, requires more computer time and memory, which ultimately limits the size and complexity of the bodies that can be considered.

5.2 Recommendations for Further Study

There are numerous opportunities for further study of electromagnetic problems directly in the time domain using the techniques developed in this thesis. A natural extension of this work would be to consider the problem of scattering by bodies with edges. There are two possible approaches to this problem. One approach would be to derive a new integro-differential equation that holds for bodies with mathematical edges. A second approach would be to use the integro-differential equations developed in this thesis on scatterers with rounded edges having radii of curvature much less than the length of the approximate incident impulse. Although the basic theory developed in this thesis applies to such problems, new numerical techniques must be developed to handle regions of small radius of curvature in order to carry out the study of bodies with edges economically using this second approach.

Another extension of this work would be to develop techniques for obtaining a better approximation for the exact electromagnetic impulse response using the approximate impulse response calculated in this thesis. Both the incident approximate impulse and the approximate impulse response are known. In addition, the convolution gives an integral equation relating the incident approximate impulse and the approximate impulse response to the exact impulse response. Thus, numerical solution of this integral equation would yield the exact impulse response. However, numerical solution is not possible if the exact impulse response contains singularity functions. But by applying the theory of geometric optics the singularity functions could be determined and their effect subtracted from the approximate impulse response. Then an augmented exact impulse response could be computed numerically. The final step would be to add the singularity functions to the augmented impulse response.

Another possible approach to the problem of obtaining a better approximation to the exact impulse response would be to use a ramp for the incident wave. The numerically computed ramp response could be differentiated twice in order to obtain a good approximation to the impulse response.

As has been illustrated in this thesis, there is a close correlation between the electromagnetic impulse response and the actual geometry of the scatterer. The

techniques developed in this thesis would permit the orderly construction of a catalogue of approximate impulse responses for interesting shapes. This catalogue should allow extrapolation to new shapes and attitudes differing somewhat from the ones in the catalogue. Finally, this cataloguing could help determine more relationships between the approximate impulse response and the geometry of the scatterer. The ultimate goal would be to develop techniques for determining the electromagnetic impulse response of a scatterer by a simple inspection of its geometry.

Although not considered in this thesis, another area of study would be the experimental measurement of electromagnetic impulse response. There are two reasons behind the desire to measure electromagnetic impulse response. First, it would give an additional check on the results obtained by using the technique introduced in this thesis. Second, it would allow the consideration of bodies with virtually any complexity. However, in many cases the experimental results would have much less accuracy and be more expensive to obtain than the numerical results. The feasibility of such an experimental measurement today appears to be only borderline. The present state of the art permits production of 100 volt voltage steps with 10 percent to 90 percent rise times of 100 pico seconds. Display of voltages with these fast rise times is also possible with present day sampling oscilloscopes. So production and display of voltages with

adequate amplitude and sufficiently small rise times are possible today. But somehow an approximate electromagnetic impulse (or step) must be launched and the resulting response must be detected if approximate electromagnetic impulse response is to be measured experimentally. This seems to be the major problem today since the transient response of antennas is not yet well understood. However, it appears that a time domain formulation similar to the one presented in this thesis could be developed to study the transient response of antennas.

LIST OF REFERENCES

M.G. Andreasen, "Scattering from Rotationally Symmetric Metallic Bodies," DDC-610-607, April 1964.

Yu. N. Barabanenkov, A.A. Tolkachev, N.A. Aytkhozhiz, and O.K. Lesota, "Scattering of Electromagnetic Pulses by Ideally Conducting Bodies of Finite Dimensions," Radio Engineering and Electronic Physics, Vol. 8, pp. 1061-63, June 1963.

H.S. Carslaw, Introduction to the Theory of Fourier's Series and Integrals. New York: Dover, 1930.

B.R. Cheo, "A Reciprocity Theorem for Electromagnetic Fields with General Time Dependence," IEEE Trans. Antennas and Propagation, Vol. AP-13, pp. 278-284, March 1965.

J.W. Cooley, "Finite Complex Fourier Transform," IBM SHARE Program Library No. SDA 3465, New York, 1966.

F.J. Friedlaender, Sound Pulses. London: Cambridge University Press, 1958.

M.B. Friedman and R. Shaw, "Diffraction of Pulses by Cylindrical Obstacles of Arbitrary Cross-Section," Trans. ASME-Series E, Vol. 29, pp. 40-46, March 1962.

R.W. Hamming, Numerical Methods for Scientists and Engineers. New York: McGraw-Hill, 1962.

R.F. Harrington, Time Harmonic Electromagnetic Fields. New York: McGraw-Hill, 1961.

S. Hong and S.L. Borison, "Short Pulse Scattering by a Cone-Direct and Inverse," IEEE Trans. Antennas and Propagation, Vol. AP-16, pp. 98-102, January 1968.

E.M. Kennaugh, "The Scattering of Short Electromagnetic Pulses by a Conducting Sphere," Proc. IRE (Correspondence), Vol. 49, p. 380, January 1961.

E.M. Kennaugh and R.L. Cosgriff, "The Use of Impulse Response in Electromagnetic Scattering Problems," 1958 IRE Nat'l Conv. Rec., pt. 1, pp. 72-77.

E.M. Kennaugh and D.L. Moffatt, "On the Axial Echo Area of the Cone Sphere Shape," Proc. IRE (Correspondence), Vol. 50, p. 199, February 1962.

E.M. Kennaugh and D.L. Moffatt, "Transient and Impulse Response Approximations," Proc. IEEE, Vol. 53, pp. 893-901, August 1965.

D.L. Moffatt and E.M. Kennaugh, "The Axial Echo Area of a Perfectly Conducting Prolate Spheriod," IEEE Trans. Antennas and Propagation, Vol. AP-13, pp. 401-409, May 1965.

P.M. Morse and H. Feshbach, Methods of Theoretical Physics. New York: McGraw-Hill, 1953.

F.K. Oshiro, F.P. Torres, and H.C. Heath, "A Source Distribution Technique for the Solution of General Electromagnetic Scattering Problems," DDC-624-586, October 13, 1965.

J. Rheinstein, "Backscatter from Spheres: A Short Pulse View," IEEE Trans. Antennas and Propagation, Vol. AP-16, pp. 89-97, January 1968.

J.A. Stratton, Electromagnetic Theory. New York: McGraw-Hill, 1941.

W.L. Weeks (with G.R. Cooper and C.D. McGillem), "Random Signal Radar," Purdue University School of Electrical Engineering, Lafayette, Final Technical Report 4696, pp. 5.1-5.34, June 1967.

APPENDIX I

GREEN'S FUNCTION FOR CYLINDRICAL PROBLEMS

In Chapter 2 the result that

$$G = \int_{-\infty}^{+\infty} \frac{\delta\left(\frac{R - z' \cos\theta_i}{c} - \tau\right)}{4\pi R}\, dz'$$

$$= \begin{cases} \dfrac{c}{2\pi\sqrt{c^2\tau^2 - P^2 \sin^2\theta_i}} & ; \quad \dfrac{P \sin\theta_i}{c} < \tau \\ 0 & ; \quad \dfrac{P \sin\theta_i}{c} > \tau \end{cases} \qquad (I.1)$$

was used.

This integral is the Green's function for cylindrical problems with an arbitrary angle of incidence. It is the purpose of this appendix to develop the above result.

In order to perform the integration in (I.1) it is convenient to make a change of variables,

$$w = \frac{R - z' \cos\theta_i}{c} \qquad (I.2)$$

$$\frac{dz'}{R} = \frac{c\,dw}{z' - R\cos\theta_i}\,, \qquad (I.3)$$

where

$$R^2 = P^2 + z'^2$$

$$0 < \theta_i \leq \pi/2 \quad .$$

In (I.3) it is necessary to get the right hand side in terms of w only. This can be done by noting that

$$(z' - R \cos \theta_i)^2 = c^2w^2 - P^2 \sin^2 \theta_i \quad .$$

Hence,

$$z' - R \cos \theta_i = \begin{cases} +\sqrt{c^2w^2 - P^2 \sin^2 \theta_i} \; ; & z' > R \cos \theta_i \\ -\sqrt{c^2w^2 - P^2 \sin^2 \theta_i} \; ; & z' < R \cos \theta_i \end{cases} .$$

Compute the value of z_o' at which $z_o' = R \cos \theta_i$.

$$z_o'^2 \sin^2 \theta_i = P^2 \cos^2 \theta_i .$$

So

$$z_o' = \frac{P \cos \theta_i}{\sin \theta_i} \; ; \quad 0 < \theta_i \leq \pi/2 \quad .$$

The value of w for which this occurs is found to be

$$w_o = \frac{P \sin \theta_i}{c}$$

by substituting z_o with (I.2).

Thus

$$\frac{dz'}{R} = \begin{cases} + \dfrac{cdw}{\sqrt{c^2w^2 - P^2 \sin^2 \theta_i}} & ; \quad w > \dfrac{P \sin \theta_i}{c} \\ - \dfrac{cdw}{\sqrt{c^2w^2 - P^2 \sin^2 \theta_i}} & ; \quad w < \dfrac{P \sin \theta_i}{c}. \end{cases} \quad (I.4)$$

Substituting (I.2) and (I.4) into (I.1) gives

$$G = \frac{c}{2\pi} \int_{\frac{P \sin \theta_i}{c}}^{\infty} \frac{\delta(w - \tau)}{\sqrt{c^2w^2 - P^2 \sin^2 \theta_i}} \, dw \, .$$

The integration is now trivial and gives

$$G = \begin{cases} \dfrac{c}{2\pi\sqrt{c^2\tau^2 - P^2 \sin^2 \theta_i}} & ; \quad \tau > \dfrac{P \sin \theta_i}{c} \\ 0 & ; \quad \tau < \dfrac{P \sin \theta_i}{c} \end{cases}$$

which is the desired result.

APPENDIX II

DERIVATION OF $\nabla \times \vec{A}$ FOR CYLINDRICAL PROBLEMS

In Chapter 2 the expression for the magnetic vector potential was derived as

$$\vec{A}(\vec{\rho},t) = \frac{c}{2\pi} \int_s ds' \int_{t'=-\infty}^{t - \frac{P \sin \theta_i}{c}} \frac{\vec{J}(\vec{\rho}',t')}{\sqrt{c^2(t-t')^2 - P^2 \sin^2 \theta_i}} dt' \quad .$$

It is the object of this Appendix to derive $\nabla \times \vec{A}$.

It is convenient to change variables,

$$w = t' + \frac{P \sin \theta_i}{c} \quad .$$

Substitution gives

$$\vec{A}(\vec{\rho},t) = \frac{c}{2\pi} \int_s ds' \int_{w=-\infty}^{t} \frac{\vec{J}(\vec{\rho}',w - \frac{P \sin \theta_i}{c})}{\sqrt{c(t-w)}\sqrt{c(t-w) + 2P \sin \theta_i}} dw \quad .$$

Now compute $\nabla \times \vec{A}$. Since the curl is with respect to the

unprimed variables, it may be taken inside the integral which gives

$$\nabla x \vec{A}(\vec{\rho},t) = \frac{c}{2\pi} \int_S ds' \int_{w=-\infty}^{t} \frac{dw}{\sqrt{c(t-w)}} \left\{ \nabla x \frac{\vec{J}(\vec{\rho}', w - \frac{P \sin\theta_i}{c})}{\sqrt{c(t-w) + 2P \sin\theta_i}} \right\} .$$

Applying a vector identity to the above equation yields

$$\nabla x \vec{A}(\vec{\rho},t) =$$

$$\frac{c}{2\pi} \int_S ds' \int_{w=-\infty}^{t} \frac{dw}{\sqrt{c(t-w)}} \left\{ \nabla \left(\frac{1}{\sqrt{c(t-w) + 2P \sin\theta_i}} \right) x \vec{J}(\vec{\rho}', w - \frac{P \sin\theta_i}{c}) + \frac{\nabla x \vec{J}(\vec{\rho}', w - \frac{P \sin\theta_i}{c})}{\sqrt{c(t-w) + 2P \sin\theta_i}} \right\} . \qquad \text{(II.1)}$$

It is convenient to work in Cartesian coordinates. In (II.1) the gradient term in the curly brackets may be written

$$\nabla \left(\frac{1}{\sqrt{c(t-w) + 2P \sin\theta_i}} \right)$$

$$= \left\{ \hat{a}_x \frac{\partial P}{\partial x} + \hat{a}_y \frac{\partial P}{\partial y} \right\} \left\{ \frac{-\sin\theta_i}{[c(t-w) + 2P\sin\theta_i]^{3/2}} \right\} .$$

But

$$P = |\vec{\rho} - \vec{\rho}'| = \sqrt{(x-x')^2 + (y-y')^2} .$$

Performing the differentiation of P gives

$$\nabla \left\{ \frac{1}{\sqrt{c(t-t') + 2P\sin\theta_i}} \right\} = - \frac{\hat{a}_p \sin\theta_i}{[c(t-w) + 2P\sin\theta_i]^{3/2}} \qquad (II.2)$$

where

$$\hat{a}_p = (\vec{\rho} - \vec{\rho}')/P .$$

In (II.1) the second term in the curly brackets is

$$\nabla x \vec{J}(\vec{\rho}', w - \frac{P\sin\theta_i}{c}) = \hat{a}_x \frac{\partial J_z}{\partial y} - \hat{a}_y \frac{\partial J_z}{\partial x} + \hat{a}_z \left\{ \frac{\partial J_y}{\partial x} - \frac{\partial J_x}{\partial y} \right\} .$$

Define $\tau = w - \frac{P\sin\theta_i}{c}$ so

$$\nabla x \vec{J}(\vec{\rho}', \tau) = \hat{a}_x \frac{\partial J_z}{\partial \tau}\frac{\partial \tau}{\partial y} - \hat{a}_y \frac{\partial J_z}{\partial \tau}\frac{\partial \tau}{\partial x} + \hat{a}_z \left\{ \frac{\partial J_y}{\partial \tau}\frac{\partial \tau}{\partial x} - \frac{\partial J_x}{\partial \tau}\frac{\partial \tau}{\partial y} \right\} .$$

Using the above definition for τ and performing the differentiation gives

$$\nabla x\vec{J}\left(\vec{\rho}', w - \frac{P \sin\theta_i}{c}\right) = -\frac{\sin\theta_i}{c}\left[\hat{a}_x \frac{\partial J_z}{\partial \tau}\left(\frac{y-y'}{P}\right)\right.$$

$$\left. - \hat{a}_y \frac{\partial J_z}{\partial \tau}\left(\frac{x-x'}{P}\right) + \hat{a}_z\left(\frac{\partial J_y}{\partial \tau}\frac{x-x'}{P} - \frac{\partial J_x}{\partial \tau}\frac{y-y'}{P}\right)\right] .$$

This may be written in the form

$$\nabla x\vec{J}\left(\vec{\rho}', w - \frac{P \sin\theta_i}{c}\right) = \frac{\sin\theta_i}{c}\left[\frac{\partial \vec{J}(\vec{\rho}', \tau)}{\partial \tau}\right]_{\tau = w - \frac{P\sin\theta_i}{c}} x\hat{a}_p \qquad \text{(II.3)}$$

Substituting (II.2) and (II.3) into (II.1) gives

$$\nabla x\vec{A}(\vec{\rho}, t) = \frac{c \sin\theta_i}{2\pi}\int_s ds' \int_{w=-\infty}^{t} \frac{dw}{\sqrt{c(t-w)}}\left\{\frac{\vec{J}(\vec{\rho}', \tau)}{[c(t-w) + 2P\sin\theta_i]^{3/2}}\right.$$

$$\left. + \frac{1}{c\sqrt{c(t-w) + 2P\sin\theta_i}}\frac{\partial \vec{J}(\vec{\rho}', \tau)}{\partial \tau}\right\}_{\tau = w - \frac{P\sin\theta_i}{c}} x\hat{a}_p .$$

Changing back to the original variable $t' = w - \frac{P \sin\theta_i}{c}$ gives

$$\nabla x\vec{A}(\vec{\rho}, t) = \frac{c \sin\theta_i}{2\pi}\int_s ds' \int_{t'=-\infty}^{t - \frac{P\sin\theta_i}{c}} \frac{dt'}{\sqrt{c^2(t-t')^2 - P^2\sin^2\theta_i}}$$

$$\cdot \left[\frac{\vec{J}(\vec{\rho}',t')}{c(t-t') + P \sin\theta_i} + \frac{1}{c}\frac{\partial \vec{J}(\vec{\rho}',t')}{\partial t'}\right] x\hat{a}_p \quad , \quad \text{(II.4)}$$

which is the desired result.

APPENDIX III

LIMITING PROCEDURE FOR CYLINDRICAL PROBLEMS

The purpose of this Appendix is to carry out the limiting procedure in equations (2.5) and (2.6) of Chapter 2. Consider the limit occuring in (2.5) first and define

$$I(\vec{\rho}'',t) =$$

$$\lim_{\vec{\rho} \to \vec{\rho}''} \frac{c \sin\theta_i}{2\pi} \int_S ds'(\hat{a}_1' \cdot \hat{a}_\rho) \int_{t'=-\infty}^{t - \frac{P \sin\theta_i}{c}} \frac{dt'}{\sqrt{c^2(t-t')^2 - P^2 \sin^2\theta_i}}$$

$$\cdot \left[\frac{H_z(\vec{\rho}',t')}{c(t-t') + P \sin\theta_i} + \frac{1}{c} \frac{\partial H_z(\vec{\rho}',t')}{\partial t'}\right] . \qquad (III.1)$$

This may be written as

$$I(\vec{\rho}'',t) =$$

$$\lim_{\vec{\rho} \to \vec{\rho}''} \frac{c \sin\theta_i}{2\pi} \int_{S-S_\varepsilon} ds'(\hat{a}_1' \cdot \hat{a}_\rho) \int_{t'=-\infty}^{t - \frac{P \sin\theta_i}{c}} \frac{dt'}{\sqrt{c^2(t-t')^2 - P^2 \sin^2\theta_i}}$$

$$\cdot \left[\frac{H_z(\vec{\rho}',t')}{c(t-t') + P \sin\theta_i} + \frac{1}{c}\frac{\partial H_z(\vec{\rho}',t')}{\partial t'}\right]$$

$$+ \lim_{\vec{\rho}\to\vec{\rho}''} \frac{c \sin\theta_i}{2\pi} \int_{s_\varepsilon} ds'(\hat{a}_1' \cdot \hat{a}_\rho) \int_{t'=-\infty}^{t - \frac{P \sin\theta_i}{c}} \frac{dt'}{\sqrt{c^2(t-t')^2 - P^2 \sin^2\theta_i}}$$

$$\cdot \left[\frac{H_z(\vec{\rho}',t')}{c(t-t') + P \sin\theta_i} + \frac{1}{c}\frac{\partial H_z(\vec{\rho}',t')}{\partial t'}\right] \qquad \text{(III.2)}$$

where s_ε is a small segment of s containing the point $\vec{\rho}''$. Define the first term n the right hand side of (III.2) to be $I_1(\vec{\rho}'',t)$. This term causes no trouble and may be written simply as

$$I_1(\vec{\rho}'',t) =$$

$$\frac{c \sin\theta_i}{2\pi} \int_{s-s_\varepsilon} ds'(\hat{a}_1' \cdot \hat{a}_\rho) \int_{t'=-\infty}^{t - \frac{P \sin\theta_i}{c}} \frac{dt'}{\sqrt{c^2 (t-t')^2 - P^2 \sin^2\theta_i}}$$

$$\cdot \left[\frac{H_z(\vec{\rho}',t')}{c(t-t') + P \sin\theta_i} + \frac{1}{c}\frac{\partial H_z(\vec{\rho}',t')}{\partial t'}\right] . \qquad \text{(III.3)}$$

Assume that $H_z(\vec{\rho},t) = 0$ for $t < (t_1 - P \sin\theta_i/c)$, so the second term on the right hand side of (III.2) may be

written as

$$I_2(\vec{\rho}'',t) =$$

$$\lim_{\vec{\rho}\to\vec{\rho}''} \frac{c \sin\theta_i}{2\pi} \int_{S_\varepsilon} ds'(\hat{a}_1'\cdot\hat{a}_p) \int_{t'=t_1 - \frac{P\sin\theta_i}{c}}^{t - \frac{P\sin\theta_i}{c}} \frac{dt'}{\sqrt{c^2(t-t')^2 - P^2\sin^2\theta_i}}$$

$$\cdot \left[\frac{H_z(\vec{\rho}',t')}{c(t-t') + P\sin\theta_i} + \frac{1}{c}\frac{\partial H_z(\vec{\rho}',t')}{\partial t'}\right] . \qquad \text{(III.4)}$$

It is convenient at this point to change variables,

$$w = t' + \frac{P\sin\theta_i}{c} ,$$

and also to break (III.4) into three pieces (I_{2a}, I_{2b}, and I_{2c}) as follows:

$$I_{2a} =$$

$$\lim_{\vec{\rho}\to\vec{\rho}''} \frac{c \sin\theta_i}{2\pi} \int_{S_\varepsilon} ds'(\hat{a}_1'\cdot\hat{a}_p) \int_{w=t_1}^{t-\Delta t} \frac{dw}{\sqrt{c(t-w)}\sqrt{c(t-w) + 2P\sin\theta_i}}$$

$$\cdot \left[\frac{H_z(\vec{\rho}',\tau)}{c(t-w) + 2P\sin\theta_i} + \frac{1}{c}\frac{\partial H_z(\vec{\rho}',\tau)}{\partial\tau}\right]_{\tau = w - \frac{P\sin\theta_i}{c}}$$

(III.5)

$$I_{2b} =$$

$$\lim_{\vec{\rho} \to \vec{\rho}''} \frac{c \sin \theta_i}{2\pi} \int_{s_\varepsilon} ds' (\hat{a}_1' \cdot \hat{a}_p) \int_{t-\Delta t}^{t} \frac{dw}{\sqrt{c(t-w)}\sqrt{c(t-w) + 2P \sin \theta_i}}$$

$$\cdot \left[\frac{1}{c} \frac{\partial H_z(\vec{\rho}', \tau)}{\partial \tau} \right]_{\tau = w - \frac{P \sin \theta_i}{c}} \qquad \text{(III.6)}$$

$$I_{2c} =$$

$$\lim_{\vec{\rho} \to \vec{\rho}''} \frac{c \sin \theta_i}{2\pi} \int_{s_\varepsilon} ds' (\hat{a}_1' \cdot \hat{a}_p) \int_{t-\Delta t}^{t} \frac{dw}{\sqrt{c(t-w)}\sqrt{c(t-w) + 2P \sin \theta_i}}$$

$$\cdot \frac{H_z(\vec{\rho}', w - \frac{P \sin \theta_i}{c})}{c(t-w) + 2P \sin \theta_i} \; . \qquad \text{(III.7)}$$

Let s_ε be a segment of the contour s with length 2ε and center at $\vec{\rho}''$ as shown in Figure III.1 and let $\vec{\rho}$ be a distance δ from $\vec{\rho}''$, assuming $\delta << \varepsilon$. So $\vec{\rho} \to \vec{\rho}''$ is equivalent to $\delta \to 0$. Finally, take ε small enough so that the curvature of s_ε is negligible. (Note that this last step is possible at all smooth points on the contour.) Thus, on s_ε the following terms may be approximated as

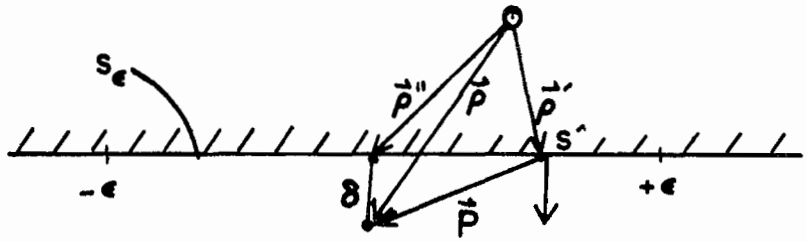

FIGURE III.1 EVALUATION OF INTEGRAL OVER S_ϵ AS $\vec{\rho} \longrightarrow \vec{\rho}''$

$$P = \sqrt{\delta^2 + s'^2}$$

$$\hat{a}_1' \cdot \hat{a}_P = \frac{\delta}{\sqrt{\delta^2 + s'^2}} \quad .$$

First consider I_{2a}. Changing the order of integration and substituting the approximation formulas into (III.5) gives

$$I_{2a} =$$

$$\lim_{\delta \to 0} \frac{c \sin \theta_i}{2\pi} \int_{w=t_1}^{t-\Delta t} \frac{dw}{\sqrt{c(t-w)}} \int_{-\varepsilon}^{\varepsilon} \frac{ds'}{\sqrt{c(t-w) + 2P \sin \theta_i}}$$

$$\cdot \left[\frac{H_z(\vec{\rho}', \tau)}{c(t-w) + 2P \sin \theta_i} + \frac{1}{c} \frac{\partial H_z(\vec{\rho}', \tau)}{\partial \tau} \right] \frac{\delta}{\sqrt{\delta^2 + s'^2}} \quad .$$

$$\tau = w - \frac{P \sin \theta_i}{c}$$

But since $P \geq 0$ and $\Delta t > 0$, we can write

$$\left| I_{2a} \right| \leq \lim_{\delta \to 0} M_1 \left| \frac{1}{2} \int_{t_1}^{t-\Delta t} \frac{dw}{\sqrt{t-w}} \right| \left| \delta \int_{-\varepsilon}^{+\varepsilon} \frac{ds'}{\sqrt{\delta^2 + s'^2}} \right|$$

where

$$\text{Max}\left|\frac{c\sin\theta_i}{\pi\sqrt{c}}\,\frac{1}{\sqrt{c(t-w)+2P\sin\theta_i}}\left[\frac{H_z(\vec{\rho}',t)}{c(t-w)+2P\sin\theta_i}+\frac{1}{c}\,\frac{\partial H_z(\vec{\rho}',t)}{\partial\tau}\right]\right| \le M_1 \quad .$$

Performing the integration gives

$$\left|I_{2a}\right| \le M_1\left(\sqrt{t-t_1}-\sqrt{\Delta t}\right)\lim_{\delta\to 0}\delta\left|\ln\left(\varepsilon+\sqrt{\varepsilon^2+\delta^2}\right)+\ln\frac{1}{\delta}\right| \quad .$$

Thus, $I_{2a}\to 0$ as $\delta\to 0$.

Second, consider I_{2b}. Equation (III.6) may be written as

$$\left|I_{2b}\right| \le \lim_{\delta\to 0} M_2\int_{-\varepsilon}^{\varepsilon} ds'\left|\hat{a}_1'\cdot\hat{a}_p\right|\int_{t-\Delta t}^{t}\frac{cdw}{\sqrt{c(t-w)}\sqrt{c(t-w)+2P\sin\theta_i}}$$

where

$$\frac{\sin\theta_i}{2\pi c}\left|\frac{\partial H_z(\vec{\rho},t)}{\partial t}\right| \le M_2 \quad .$$

Changing variables $x = c(t-w)$ gives

$$\left|I_{2b}\right| \le \lim_{\delta\to 0} M_2\int_{-\varepsilon}^{+\varepsilon} ds'\left|\hat{a}_1'\cdot\hat{a}_p\right|\int_{0}^{c\Delta t}\frac{dx}{\sqrt{x^2+2P\sin\theta_i\,x}}$$

Integrating gives

$$\left|I_{2b}\right| \leq \lim_{\delta \to 0} M_2 \int_{-\varepsilon}^{\varepsilon} ds' \left|\hat{a}_1' \cdot \hat{a}_p\right| \left| \ln 2(\sqrt{c^2\Delta t^2 + 2P \sin\theta_i \, c\Delta t} + c\Delta t + P \sin\theta_i) + \ln \frac{1}{2P \sin\theta_i} \right| .$$

Since $\Delta t > 0$

$$\left| \ln 2(\sqrt{c^2\Delta t^2 + 2P \sin\theta_i \, c\Delta t} + c\Delta t + P \sin\theta_i) \right| \leq M_3 .$$

Substituting in the approximate formulas for P and $\hat{a}_1' \cdot \hat{a}_p$ gives

$$\left|I_{2b}\right| \leq \lim_{\delta \to 0} M_2 M_3 \, \delta \int_{-\varepsilon}^{\varepsilon} \frac{ds'}{\sqrt{\delta^2 + s'^2}}$$

$$+ \lim_{\delta \to 0} M_2 \, \delta \int_{-\varepsilon}^{\varepsilon} \frac{ds'}{\sqrt{\delta^2 + s'^2}} \left| \ln \left(\frac{1}{2 \sin\theta_i \sqrt{\delta^2 + s'^2}} \right) \right| .$$

But the first term is zero as was shown for I_{2a}. Thus,

$$\left|I_{2b}\right| \leq \lim_{\delta \to 0} M_2 \, \delta \ln \frac{1}{2 \sin\theta_i} \, \delta \int_{-\varepsilon}^{\varepsilon} \frac{ds'}{\sqrt{\delta^2 + s'^2}} .$$

Carrying out the integration gives

$$\left|I_{2b}\right| \leq \lim_{\delta \to 0} 2M_2\, \delta \left[\left|\ln \frac{1}{\delta}\right| \left|\ln(\varepsilon + \sqrt{\varepsilon^2 + \delta^2}) + \ln \frac{1}{\delta}\right|\right] .$$

Hence, $I_{2b} \to 0$ as $\delta \to 0$.

Finally, consider I_{2c}. Assume that ε and Δt are small enough so that H_z in I_{2c} may be approximated by

$$H_z(\vec{\rho}', w - P/c) = H_z(\vec{\rho}'', t) .$$

Thus, (III.7) may be written as

$$I_{2c} =$$

$$\frac{H_z(\vec{\rho}'', \tau) \sin\theta_i}{2} \lim_{\delta \to 0} \frac{c}{\pi} \int_{-\varepsilon}^{\varepsilon} ds'(\hat{a}_1' \cdot \hat{a}_p) \int_{t-\Delta t}^{t} \frac{dw}{\sqrt{c(t-w)}\,[c(t-w) + 2P \sin\theta_i]^{3/2}} .$$

Change variables $x = c(t-w)$ to give

$$I_{2c} =$$

$$\frac{1}{2} H_z(\vec{\rho}'', t) \sin\theta_i \lim_{\delta \to 0} \frac{1}{\pi} \int_{-\varepsilon}^{\varepsilon} ds'(\hat{a}_1' \cdot \hat{a}_p) \int_{0}^{c\Delta t} \frac{dx}{\sqrt{x}\,[x + 2P \sin\theta_i)^{3/2}} .$$

Integrating out the x-variation gives

$$I_{2c} =$$

$$\frac{1}{2} H_z(\vec{\rho}'',t) \lim_{\delta \to 0} \frac{1}{\pi} \int_{-\varepsilon}^{\varepsilon} ds'(\hat{a}_1' \cdot \hat{a}_p) P \frac{\sqrt{c\Delta t}}{\sqrt{c\Delta t + 2P \sin \theta_i}} .$$

Substitution of the approximation formulas for P and $\hat{a}_1' \cdot \hat{a}_p$ gives

$$I_{2c} =$$

$$\frac{1}{2} H_z(\vec{\rho}'',t) \lim_{\delta \to 0} \frac{2\delta}{\pi} \int_{0}^{\varepsilon} \frac{ds'}{\delta^2 + s'^2} \frac{\sqrt{c\Delta t}}{\sqrt{c\Delta t + 2 \sin \theta_i \sqrt{\delta^2 + s'^2}}} .$$

Upon integration by parts I_{2c} becomes

$$I_{2c} =$$

$$+\frac{1}{2} H_z(\vec{\rho}'',t) \left[\lim_{\delta \to 0} \frac{\sqrt{c\Delta t}}{\sqrt{c\Delta t + 2 \sin \theta_i \sqrt{\delta^2 + \varepsilon^2}}} \frac{2}{\pi} \tan^{-1}\left(\frac{\varepsilon}{\delta}\right) \right.$$

$$\left. + \lim_{\delta \to 0} \int_{0}^{\varepsilon} \frac{\sqrt{c\Delta t} \sin \theta_i \, s'}{\sqrt{\delta^2 + s'^2}\left(c\Delta t + 2 \sin \theta_i \sqrt{\delta^2 + s'^2}\right)^{3/2}} \frac{2}{\pi} \tan^{-1} \frac{\varepsilon}{\delta} \, ds' \right] .$$

Now after moving the limit inside the integral and taking both limits, I_{2c} reduces to

$$I_{2c} =$$

$$\frac{1}{2} H_z(\vec{\rho}'',t)\left[\frac{\sqrt{c\Delta t}}{\sqrt{c\Delta t + 2 \sin\theta_i\, \varepsilon}} + \int_0^{\varepsilon} \frac{\sqrt{c\Delta t}\, \sin\theta_i}{(c\Delta t + 2 \sin\theta_i\, s')^{3/2}}\, ds'\right] .$$

After performing the integration and combining terms, the above expression yields

$$I_{2c} = \frac{1}{2} H_z(\vec{\rho}'',t) \quad .$$

So in summary

$$I(\vec{\rho}'',t) = \frac{1}{2} H_z(\vec{\rho}'',t)$$

$$+ \lim_{s_\varepsilon \to 0} \frac{c \sin\theta_i}{2\pi} \int_{s-s_\varepsilon} ds'(\hat{a}_1' \cdot \hat{a}_p) \int_{t'=-\infty}^{t - \frac{P \sin\theta_i}{c}} \frac{dt'}{\sqrt{c^2(t-t)^2 - P^2 \sin^2\theta_i}}$$

$$\cdot \left[\frac{H_z(\vec{\rho}',t')}{c(t-t') + P \sin\theta_i} + \frac{1}{c} \frac{\partial H_z(\vec{\rho}',t')}{\partial t'}\right] \quad . \quad .$$

The limiting procedure for (2.6) is exactly the same as for (2.5) since $\hat{a}_1' = \hat{a}_1''$ on s_ε. Hence, the result for (2.6) can be written by inspection.

APPENDIX IV

DERIVATION OF $\nabla x\vec{A}$ FOR THREE DIMENSIONAL PROBLEMS

The vector potential $\vec{A}$ due to a current distribution $\vec{J}$ on a surface S is given by

$$\vec{A}(\vec{r},t) = \frac{1}{4\pi}\int_S \frac{\vec{J}(\vec{r}',t - R/c)}{R}\, dS' \qquad (IV.1)$$

where

$$R = |\vec{r} - \vec{r}'| \quad .$$

It is the object of this appendix to show that

$$\nabla x\vec{A}(\vec{r},t) = \frac{1}{4\pi}\int_S \left[\frac{\vec{J}(\vec{r}',\tau)}{R^2} + \frac{1}{Rc}\frac{\partial J(\vec{r},\tau)}{\partial \tau}\right]_{\tau=t-R/c} x\hat{a}_R dS'$$

where

$$\hat{a}_R = \frac{\vec{r} - \vec{r}'}{R} \quad .$$

After taking the curl of $\vec{A}$ with respect to the unprimed variables (IV.1) becomes

$$\nabla x \vec{A}(\vec{r},t) = \frac{1}{4\pi} \int_S \nabla x \left[\frac{\vec{J}(\vec{r}',t - R/c)}{R} \right] dS' \quad .$$

Using a vector identity gives

$$\nabla x \vec{A}(\vec{r},t) =$$

$$\frac{1}{4\pi} \int_S \left[\nabla \left(\frac{1}{R} \right) x \vec{J}(\vec{r}',t - R/c) + \frac{1}{R} \nabla x \vec{J}(\vec{r}',t - R/c) \right] x dS' \quad . \tag{IV.2}$$

It is easy to show that

$$\nabla \left(\frac{1}{R} \right) = - \frac{\hat{a}_R}{R^2} \quad . \tag{IV.3}$$

Now consider the curl term in the square brackets of (IV.2). Expanding this term in Cartesian coordinates gives

$$\nabla x \vec{J}(\vec{r}',t - R/c) =$$

$$\hat{a}_x \left(\frac{\partial J_z}{\partial y} - \frac{\partial J_y}{\partial z} \right) + \hat{a}_y \left(\frac{\partial J_x}{\partial z} - \frac{\partial J_z}{\partial x} \right) + \hat{a}_z \left(\frac{\partial J_y}{\partial x} - \frac{\partial J_x}{\partial y} \right) \quad . \tag{IV.4}$$

Define $\tau = t - R/c$ so (IV.4) can be written as

$$\nabla x \vec{J}(\vec{r}',\tau) = - \frac{1}{c} \left[\hat{a}_x \left(\frac{\partial J_z}{\partial \tau} \frac{\partial \tau}{\partial y} - \frac{\partial J_y}{\partial \tau} \frac{\partial \tau}{\partial z} \right) \right.$$

$$+ \hat{a}_y \left(\frac{\partial J_x}{\partial \tau} \frac{\partial \tau}{\partial z} - \frac{\partial J_z}{\partial \tau} \frac{\partial \tau}{\partial x} \right) + \hat{a}_z \left(\frac{\partial J_y}{\partial \tau} \frac{\partial \tau}{\partial x} - \frac{\partial J_x}{\partial \tau} \frac{\partial \tau}{\partial y} \right)] \quad . \quad \text{(IV.5)}$$

Using the definition of τ and performing the differentiation simplifies (IV.5) to

$$\nabla x \vec{J}(\vec{r}', t - R/c) = \frac{1}{c} \left[\frac{\partial \vec{J}(\vec{r}', \tau)}{\partial \tau} \right]_{\tau = t - R/c} x \hat{a}_R \quad . \quad \text{(IV.6)}$$

Substituting (IV.3) and (IV.6) into (IV.7) gives the desired result

$$\nabla x \vec{A}(\vec{r}, t) = \frac{1}{4\pi} \int_S \left[\frac{\vec{J}(\vec{r}', \tau)}{R^2} + \frac{1}{Rc} \frac{\partial \vec{J}(\vec{r}', \tau)}{\partial \tau} \right]_{\tau = t - R/c} x \hat{a}_R dS' \quad .$$

(IV.7)

APPENDIX V

LIMITING PROCEDURE FOR THREE DIMENSIONAL PROBLEMS

The purpose of this Appendix is to carry out the limiting procedure in equation (2.11) of Chapter 2. Consider the limit occurring in (2.11) and define it to be

$$\vec{I}(\vec{r}'',t) = \lim_{\vec{r}\to\vec{r}''} \frac{1}{4\pi} \int_S \left[\frac{\vec{J}(\vec{r}',\tau)}{R^2} + \frac{1}{Rc}\frac{\partial \vec{J}(\vec{r}',\tau)}{\partial\tau}\right]_{\tau=t-R/c} x\hat{a}_R dS'. \tag{V.1}$$

Equation (V.1) may be written as

$$\vec{I}(\vec{r}'',t) = \vec{I}_1(\vec{r}'',t) + \vec{I}_2(\vec{r}'',t)$$

where

$$\vec{I}_1(\vec{r}'',t) = \lim_{\vec{r}\to\vec{r}''} \frac{1}{4\pi} \int_{S-S_\varepsilon} \left[\frac{\vec{J}(\vec{r}',\tau)}{R^2} + \frac{1}{Rc}\frac{\partial \vec{J}(\vec{r}',\tau)}{\partial\tau}\right]_{\tau=t-R/c} x\hat{a}_R dS'$$

$$\vec{I}_2(\vec{r}'',t) = \lim_{\vec{r}\to\vec{r}''} \frac{1}{4\pi} \int_{S_\varepsilon} \left[\frac{\vec{J}(\vec{r}',\tau)}{R^2} + \frac{1}{Rc}\frac{\partial \vec{J}(\vec{r}',\tau)}{\partial\tau}\right]_{\tau=t-R/c} x\hat{a}_R dS'$$

S_ε is a small patch of surface containing $\vec{r}''$.

The term $\vec{I}_1(\vec{r}'',t)$ causes no trouble and may be written as

$$\vec{I}_1(\vec{r}'',t) = \frac{1}{4\pi}\int_{S-S_\varepsilon}\left[\frac{\vec{J}(\vec{r}',\tau)}{R^2} + \frac{1}{Rc}\frac{\partial\vec{J}(\vec{r}',\tau)}{\partial\tau}\right]_{\tau=t-R/c} x\hat{a}_R dS' \quad . \quad (V.2)$$

Let $\hat{a}_1'$ be the unit outward normal vector at $\vec{r}'$. Upon replacing $\vec{J}$ by $\hat{a}_1'x\vec{H}$ the expression for $\vec{I}_2(\vec{r}'',t)$ becomes

$$\vec{I}_2(\vec{r}'',t) = \lim_{\vec{r}\to\vec{r}''}\frac{1}{4\pi}\int_{S_\varepsilon}\left\{\hat{a}_1' x\left[\frac{\vec{H}(\vec{r}',\tau)}{R^2} + \frac{1}{Rc}\frac{\partial\vec{H}(\vec{r}',\tau)}{\partial\tau}\right]_{\tau=t-R/c}\right\} x\hat{a}_R dS' \quad .$$

To expedite the evaluation of this limit it is helpful to break $\vec{I}_2$ into two parts:

$$\vec{I}_2(\vec{r}'',t) = \vec{I}_{2a}(\vec{r}'',t) + \vec{I}_{2b}(\vec{r}'',t)$$

where

$$\vec{I}_{2a}(\vec{r}'',t) = \lim_{\vec{r}\to\vec{r}''}\frac{1}{4\pi c}\int_{S_\varepsilon}\left\{\hat{a}_1' x\left[\frac{1}{R}\frac{\partial\vec{H}(\vec{r}',\tau)}{\partial\tau}\right]_{\tau=t-R/c}\right\} x\hat{a}_R dS' \quad (V.3)$$

$$\vec{I}_{2b}(\vec{r}'',t) = \lim_{\vec{r}\to\vec{r}''} \frac{1}{4\pi} \int_{S_\varepsilon} \left\{ \hat{a}_1' \times \left[\frac{\vec{H}(\vec{r}',\tau)}{R^2} \right]_{\tau=t-R/c} \right\} \times \hat{a}_R \, dS' \quad . \quad (V.4)$$

Let S_ε be a small circular patch of surface with radius ε and center at $\vec{r}''$ as shown in Figure V.1 and let $\vec{r}$ be a distance δ from $\vec{r}''$, assuming $\delta << \varepsilon$. So $\vec{r} \to \vec{r}''$ is equivalent to $\delta \to 0$. Finally take S_ε small enough so that the curvature of S_ε is negligible. (Note that this last step is possible at all smooth points on the surface.) A cylindrical coordinate system with its origin at $\vec{r}''$ and its z-axis normal to S_ε as shown in Figure V.1 is used. Thus,

$$\hat{a}_1' = \hat{a}_z$$

$$R = \sqrt{\delta^2 + \rho^2}$$

$$\hat{a}_R = \frac{(-\rho \hat{a}_\rho + \delta \hat{a}_z)}{R} \quad .$$

Using the vector identity for a triple cross product casts (V.3) and (V.4) into the form

$$\vec{I}_{2a}(\vec{r}'',t) = \lim_{\delta \to 0} \frac{1}{4\pi c} \int_{S_\varepsilon} \left\{ (\hat{a}_z \cdot \hat{a}_R) \frac{1}{R} \frac{\partial \vec{H}}{\partial \tau} \right.$$

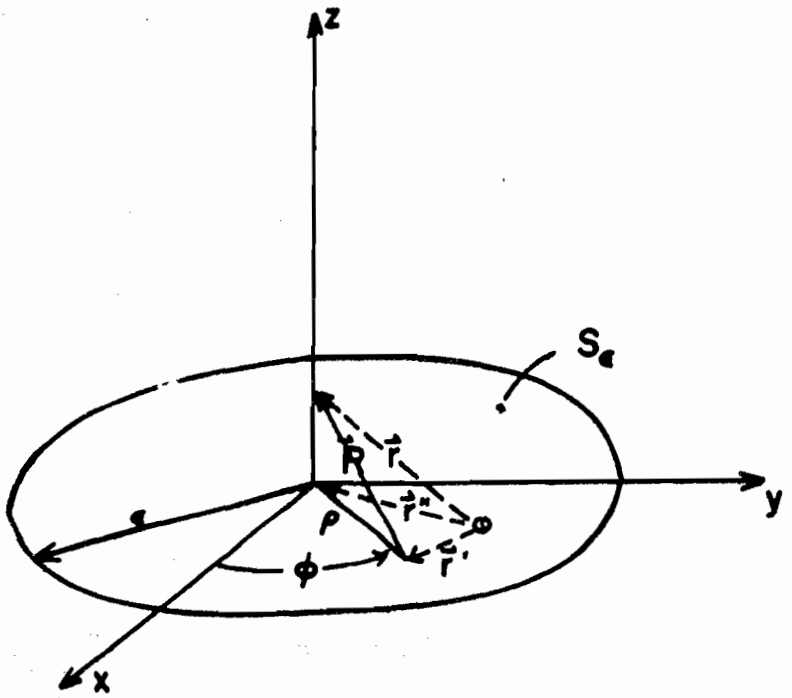

FIGURE V.1 EVALUATION OF INTEGRAL OVER S_ϵ AS $\vec{r} \rightarrow \vec{r}''$

$$- \hat{a}_z \frac{1}{R} (\hat{a}_R \cdot \frac{\partial \vec{H}}{\partial \tau}) \Big\} dS' \qquad (V.5)$$

$$\vec{I}_{2b}(\vec{r}'',t) = \lim_{\delta \to 0} \frac{1}{4\pi} \int_{S_\varepsilon} \Big\{ (\hat{a}_z \cdot \hat{a}_R) \frac{\vec{H}}{R^2}$$

$$- \hat{a}_z \frac{1}{R^2} (\hat{a}_R \cdot \vec{H}) \Big\} dS' \quad . \qquad (V.6)$$

Now take ε small enough so that $\vec{H}$ and $\frac{\partial \vec{H}}{\partial \tau}$ are essentially constant on S_ε. In this case the second terms in (V.5) and (V.6) reduce to an integration of sines and cosines over a complete period, and thus, contribute nothing to the integral. In addition $\vec{H}$ and $\frac{\partial \vec{H}}{\partial \tau}$ may be taken outside the integral giving

$$\vec{I}_{2a}(\vec{r}'',t) = \frac{1}{4\pi c} \frac{\partial \vec{H}(\vec{r}'',t)}{\partial t} \lim_{\delta \to 0} \int_{S_\varepsilon} \frac{\hat{a}_z \cdot \hat{a}_R}{R} dS' \qquad (V.7)$$

$$\vec{I}_{2b}(\vec{r}'',t) = \frac{1}{2}\vec{H}(\vec{r}'',t) \lim_{\delta \to 0} \frac{1}{2\pi} \int_{S_\varepsilon} \frac{\hat{a}_z \cdot \hat{a}_R}{R^2} \, dS' \quad . \quad (V.8)$$

Substitution of the approximation formulas for $\hat{a}_R$ and R into (V.7) yields

$$\vec{I}_{2a}(\vec{r}'',t) = \frac{1}{4\pi c} \frac{\partial \vec{H}(\vec{r}'',t)}{\partial t} \lim_{\delta \to 0} \int_{\rho=0}^{\varepsilon} \int_{\phi=0}^{2\pi} \frac{\delta}{\delta^2 + \rho^2} \rho \, d\rho \, d\phi \quad .$$

Integration reduces $\vec{I}_{2a}$ to

$$\vec{I}_{2a}(\vec{r}'',t) = \frac{1}{2c} \frac{\partial \vec{H}(\vec{r}'',t)}{\partial \tau} \lim_{\delta \to 0} \frac{1}{2} \delta \left[\ln(\delta^2 + \varepsilon^2) + \ln \left[\frac{1}{\delta} \right] \right] .$$

Hence,

$$\vec{I}_{2a}(\vec{r}'',t) = 0 \quad .$$

Finally substitute the approximation formulas for $\hat{a}_R$ and R into (V.8) to obtain

$$\vec{I}_{2b}(\vec{r}'',t) = \frac{1}{2}\vec{H}(\vec{r}'',t) \lim_{\delta \to 0} \frac{1}{2\pi} \int_{\rho=0}^{\varepsilon} \int_{\phi=0}^{2\pi} \frac{\delta}{(\delta^2 + \rho^2)^{3/2}} \rho \, d\rho \, d\phi \quad .$$

Integration then reduces $\vec{I}_{2b}$ to

$$\vec{I}_{2b}(\vec{r}'',t) = \frac{1}{2}\vec{H}(\vec{r}'',t) \lim_{\delta \to 0} \delta\left[\frac{1}{\delta} - \sqrt{\frac{1}{\delta^2 + \varepsilon^2}}\right] .$$

Thus,

$$\vec{I}_{2b}(\vec{r}'',t) = \frac{1}{2}\vec{H}(\vec{r}'',t) .$$

So in summary

$$\vec{I}(\vec{r}'',t) = \frac{1}{2}\vec{H}(\vec{r}'',t)$$

$$+ \lim_{S_\varepsilon \to 0} \frac{1}{4\pi} \int_{S-S_\varepsilon} \left[\frac{\vec{J}(\vec{r}',\tau)}{R^2} + \frac{1}{Rc}\frac{\partial \vec{J}(\vec{r}',\tau)}{\partial \tau}\right]_{\tau=t-R/c} x\hat{a}_R dS' . \quad (V.9)$$

APPENDIX VI

FOURIER SERIES OF SPACE INTEGRATION ARGUMENT

This Appendix shows that the Fourier series representations of the space integration arguments in (3.1), (3.2), and (3.3) are valid and also shows how the resultant Fourier coefficients behave. First consider (3.1) in which the space integration argument is

$$f(\phi) = \hat{a}_1' \cdot \hat{a}_P \int_{t'=t_1}^{t-P} \frac{dt'}{\sqrt{(t-t')^2 - P^2}} \left[\frac{H(\phi,t')}{t - t' + P} + \frac{\partial H(\phi,t')}{\partial t'} \right] \tag{VI.1}$$

where

$$H(\phi,t') \quad \text{replaces} \quad H(\vec{\rho}',t)$$

$$P = P(\phi) \quad .$$

Now expand $H(\phi,t')$ in a Taylor series about $t' = t - P$, i.e.,

$$H(\phi,t') = H_0(\phi) + H_1(\phi)(t-P-t') + \frac{1}{2} H_2(\phi)(t-t'+P)^2 + \ldots$$

Then (VI.1) can be written as

$$f(\phi) = \hat{a}_1' \cdot \hat{a}_P \int \frac{dt'}{\sqrt{t - t' - P}} \left\{ \frac{1}{(t-t'+P)^{3/2}} [H_0 + H_1(t-t'-P) + \ldots] \right.$$

$$\left. + \frac{1}{(t-t'+P)^{3/2}} [H_1 + H_2(t-t'-P) + \ldots] \right\} . \qquad \text{(VI.2)}$$

It is convenient to change variables,

$$x^2 = t - t' - P \ ,$$

in (VI.2) giving

$$f(\phi) = 2\, \hat{a}_1' \cdot \hat{a}_P \int_0^{\sqrt{t-t'-P}} dx \left\{ \frac{1}{(x+2P)^{3/2}} [H_0 + H_1 x^2 + \ldots] \right.$$

$$\left. + \frac{1}{(x+2P)^{1/2}} [H_1 + H_2 x^2 + \ldots] \right\} . \qquad \text{(VI.3)}$$

Integrating (VI.3) term by term yields

$$f(\phi) = 2\, \hat{a}_1' \cdot \hat{a}_P \left\{ H_0 \frac{\sqrt{t - t' - P}}{2P\sqrt{t - t_1 + P}} + H_1 \left[- \frac{\sqrt{t - t_1 - P}}{\sqrt{t - t_1 + P}} \right.\right.$$

$$\left.\left. + \ln \left\{ \frac{\sqrt{t - t_1 + P} + \sqrt{t - t_1 - P}}{\sqrt{2P}} \right\} \right] + \ldots \right\}$$

$$+ \quad 2\,\hat{a}_1' \cdot \hat{a}_P \left\{ H_1 \ln \left[\frac{\sqrt{t - t_1 + P} + \sqrt{t - t_1 - P}}{\sqrt{2P}} \right] \right.$$

$$+ \quad H_2 \left[\frac{\sqrt{(t-t_1)^2 - P^2}}{2} \right.$$

$$\left. \left. + \quad P \ln \left[\frac{\sqrt{t - t_1 + P} + \sqrt{t - t_1 - P}}{\sqrt{2P}} \right] \right] + \ldots \right\} \quad . \qquad \text{(VI.4)}$$

Since $t - P > t_1$, then $f(\phi)$ is continuous and has at least a bounded first derivative for $P > P_0 > 0$. It then remains to investigate the behavior of $f(\phi)$ about $P = 0$. Let $P = 0$ occur when $\phi = \phi_0$. To investigate $f(\phi)$ near $\phi = \phi_0$ it is necessary to have an expression for $\hat{a}_1' \cdot \hat{a}_P$ in this range. Assume that the contour is smooth so that this portion of the contour may be represented as an arc of a circle with radius of curvature $R(\phi)$ as shown in Figure VI.1. In this representation a positive sign is assigned to R if $\vec{R}$ is an outward normal and a negative sign is assigned to R if $\vec{R}$ is an inward normal, i.e., $R(\phi)$ is positive at ϕ if the contour is locally convex and negative if the contour is locally concave. Applying the law of cosines to Figure VI.1 gives

$$\hat{a}_1' \cdot \hat{a}_P = - \frac{P}{2R} \, . \qquad \text{(VI.5)}$$

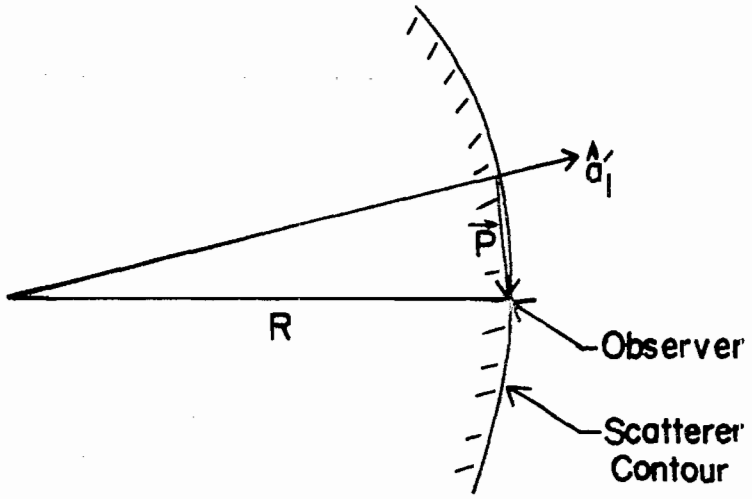

FIGURE VI .I REPRESENTATION OF CONTOUR ABOUT OBSERVER

Substitution of (VI.5) into (VI.4) yields

$$f(\phi) = -\frac{1}{2R}\left\{H_0 \frac{\sqrt{t - t_1 - P}}{\sqrt{t - t_1 + P}} + 2 H_1 P\left[-\frac{\sqrt{t - t_1 - P}}{\sqrt{t - t_1 + P}}\right.\right.$$

$$+ 2 \ln\left[\frac{\sqrt{t - t_1 - P} + \sqrt{t - t_1 + P}}{\sqrt{2P}}\right]]$$

$$+ 2H P\left[\frac{\sqrt{(t-t_1)^2 - P^2}}{2}\right.$$

$$\left.\left.+ P \ln\left[\frac{\sqrt{t - t_1 - P} + \sqrt{t - t_1 + P}}{\sqrt{2P}}\right]] + \ldots\right\} \qquad \text{(VI.6)}$$

where

$$0 < |\phi - \phi_0| < \varepsilon$$

$$0 < P \quad .$$

Since $t_1 < t - P$, then (VI.6) shows that $f(\phi)$ is continuous for all values of ϕ. Moreover, (VI.6) shows that the first derivative of $f(\phi)$ possesses only a logarithmic singularity at ϕ_0.

Thus, since $f(\phi)$ is continuous and bounded, then the Fourier series representation is not only valid, but also uniformly convergent (Carslaw, 1930). In addition, since

the first derivative of $f(\phi)$ possesses only a logarithmic singularity, then the absolute value of its m^{th} Fourier coefficient is less than $M/m^{2-\varepsilon}$ for all m greater than zero where ε is an arbitrarily small positive number and M is some positive number independent of m.

The treatment of (3.2) is the same as for (3.1). The conclusions are also the same. Thus, the Fourier series representation of the space integration argument in (3.2) is not only valid but also uniformly convergent. Furthermore, the m^{th} Fourier coefficient is less than $M/m^{2-\varepsilon}$ for all m greater than zero where ε is an arbitrarily small positive number and M is some positive number independent of m.

The consideration of (3.3) is somewhat simpler than either (3.1) or (3.2) since P is never zero in (3.3). The space integration argument in (3.3) is

$$g(\phi) = \hat{a}_1' \cdot \hat{a}_\rho \int_{t'=t_1}^{t-P} \frac{dt'}{\sqrt{t - t' - P}} \frac{\partial H(\phi,t')}{\partial t'} \qquad \text{(VI.7)}$$

where

$$H(\phi,t') \quad \text{replaces} \quad H(\vec{\rho}',t)$$

$$P = P(\phi) \quad .$$

Now expand the time derivative of H in a Taylor series about

$t' = t - P$, i.e.,

$$\frac{\partial H(\phi,t')}{\partial t'} = G_0(\phi) + G_1(\phi)(t-P-t') + \frac{1}{2} G_2(\phi)(t-P-t')^2 + \ldots .$$

Thus, (VI.7) can be written as

$$g(\phi) = \hat{a}_1' \cdot \hat{a}_\rho \int_{t'=t_1}^{t-P} dt' \left[\frac{G_0}{(t-P-t')^{1/2}} + G_1(t-P-t')^{1/2} + \ldots\right] .$$

Performing this integration gives

$$g(\phi) = 2\hat{a}_1' \cdot \hat{a}_\rho \left[G_0(t-t_1-P)^{1/2} + \frac{1}{3} G_1(t-t_1-P)^{3/2} + \ldots\right] . \qquad \text{(VI.8)}$$

Thus, $g(\phi)$ is continuous. Moreover, since the contour is smooth, then the first derivative of $g(\phi)$ exists and is at least bounded. Carslaw (1930) shows that under these conditions the Fourier series representation of $g(\phi)$ exists, is uniformly convergent, and that the absolute magnitude of the m^{th} Fourier coefficient is less than M/m^2 for all m greater than zero, where M is some positive constant independent of m.